Research Paper

THEMED ISSUE: Mantle to Surface Dynamics during the Transition from Subduction to Collision to Tectonic Escape: Results from the Continental Dynamics–Central Anatolian Tectonics (CD-CAT) Project

GEOSPHERE

GEOSPHERE, v. 17, no. 1

https://doi.org/10.1130/GES02266.1

13 figures; 3 tables; 1 supplemental file

CORRESPONDENCE: mcosca@usgs.gov

CITATION: Cosca, M.A., Reid, M., Delph, J.R., Gençalioğlu Kuşcu, G., Blichert-Toft, J., Premo, W., Whitney, D.L., Teyssier, C., and Rojay, B., 2021, Age and mantle sources of Quaternary basalts associated with "leaky" transform faults of the migrating Anatolia-Arabia-Africa triple junction: Geosphere, v. 17, no. 1, p. 69–94, https://doi.org/10.1130/GES02266.1.

Science Editor: Andrea Hampel
Associate Editor: Julie Roberge

Received 4 April 2020
Revision received 20 August 2020
Accepted 26 September 2020

Published online 4 December 2020

GOLD OPEN ACCESS

THE GEOLOGICAL SOCIETY OF AMERICA®

Age and mantle sources of Quaternary basalts associated with "leaky" transform faults of the migrating Anatolia-Arabia-Africa triple junction

Michael A. Cosca[1], Mary Reid[2], Jonathan R. Delph[3], Gonca Gençalioğlu Kuşcu[4], Janne Blichert-Toft[5], Wayne Premo[6], Donna L. Whitney[7], Christian Teyssier[7], and Bora Rojay[8]

[1]Geology, Geophysics, and Geochemistry Science Center, U.S. Geological Survey, Denver Federal Center, MS 963, Denver, Colorado 80225, USA
[2]School of Earth and Sustainability, Northern Arizona University, Flagstaff, Arizona 86011, USA
[3]Department of Earth, Atmospheric, and Planetary Sciences, Purdue University, West Lafayette, Indiana 47907, USA
[4]Department of Geological Engineering, Muğla Sıtkı Koçman University, Kötekli-Muğla, TR-48000, Turkey
[5]Laboratoire de Géologie de Lyon, Ecole Normale Supérieure de Lyon, CNRS UMR 5276, Université de Lyon, 46 Allée d'Italie, 69007 Lyon, France
[6]Geology and Environmental Change Science Center, U.S. Geological Survey, Denver Federal Center, MS 963, Denver, Colorado 80225, USA
[7]Earth and Environmental Sciences, University of Minnesota, Minneapolis, Minnesota 55455, USA
[8]Department of Geological Engineering, Middle East Technical University, Ankara 06800, Turkey

ABSTRACT

The Anatolia (Eurasia), Arabia, and Africa tectonic plates intersect in southeast Turkey, near the Gulf of İskenderun, forming a tectonically active and unstable triple junction (the A^3 triple junction). The plate boundaries are marked by broad zones of major, dominantly left-lateral transform faults including the East Anatolian fault zone (the Anatolia-Arabia boundary) and the Dead Sea fault zone (the Arabia-Africa boundary). Quaternary basalts occur locally within these "leaky" transform fault zones (similar to those observed within oceanic transform faults), providing evidence that mantle melting, basalt genesis, and eruption are linked to crustal deformation and faulting that extends into the upper mantle. We investigated samples of alkaline basalt (including basanite) from the Toprakkale and Karasu volcanic fields within a broad zone of transtension associated with these plate-boundary faults near the İskenderun and Amik Basins, respectively.

Toprakkale basalts and basanites have $^{40}Ar/^{39}Ar$ plateau ages ranging from 810 ± 60 ka to 46 ± 13 ka, and Karasu volcanic field basalts have $^{40}Ar/^{39}Ar$ plateau ages ranging from 2.63 ± 0.17 Ma to 52 ± 16 ka. Two basanite samples within the Toprakkale volcanic field have isotopic characteristics of a depleted mantle source, with $^{87}Sr/^{86}Sr$ of 0.703070 and 0.703136, $^{143}Nd/^{144}Nd$ of 0.512931 and 0.512893, $^{176}Hf/^{177}Hf$ of 0.283019 and 0.282995, $^{206}Pb/^{204}Pb$ of 19.087 and 19.155, and $^{208}Pb/^{204}Pb$ of 38.861 and 38.915. The $^{176}Hf/^{177}Hf$ ratios of Toprakkale basalts (0.282966–0.283019) are more radiogenic than Karasu basalts (0.282837–0.282965), with some overlap in $^{143}Nd/^{144}Nd$ ratios (0.512781–0.512866 vs. 0.512648–0.512806). Toprakkale $^{206}Pb/^{204}Pb$ ratios (19.025 ± 0.001) exhibit less variation than that observed for Karasu basalts (18.800–19.324), and $^{208}Pb/^{204}Pb$ values for Toprakkale basalts (38.978–39.103) are slightly lower than values for Karasu basalts (39.100–39.219). Melting depths estimated for the basalts from both volcanic fields generally cluster between 60 and 70 km, whereas the basanites record melting depths of ~90 km. Depth estimates for the basalts largely correspond to the base of a thin lithosphere (~60 km) observed by seismic imaging. We interpret the combined radiogenic isotope data (Sr, Nd, Hf, Pb) from all alkaline basalts to reflect partial melting at the base of the lithospheric mantle. In contrast, seismic imaging indicates a much thicker (>100 km) lithosphere beneath southern Anatolia, a substantial part of which is likely subducted African lithosphere. This thicker lithosphere is adjacent to the surface locations of the basanites. Thus, the greater melting depths inferred for the basanites may include partial melt contributions either from the lithospheric mantle of the attached and subducting African (Cyprean) slab, or from partial melting of detached blocks that foundered due to convective removal of the Anatolian lithosphere and that subsequently melted at ~90 km depth within the asthenosphere.

The Quaternary basalts studied here are restricted to a broad zone of transtension formed in response to the development of the A^3 triple junction, with an earliest erupted age of 2.63 Ma. This indicates that the triple junction was well established by this time. While the current position of the A^3 triple junction is near the Amik Basin, faults and topographic expressions indicate that inception of the triple junction began as early as 5 Ma in a position farther to the northeast of the erupted basalts. Therefore, the position of the A^3 triple junction appears to have migrated to the southwest since the beginning of the Pliocene as the Anatolia-Africa plate boundary has adjusted to extrusion (tectonic escape) of the Anatolia plate. Establishment of the triple junction over the past 5 m.y. was synchronous with rollback of the African slab beneath Anatolia and associated trench retreat, consistent with Pliocene uplift in Cyprus

Michael Cosca https://orcid.org/0000-0002-0600-7663

and with the current positions of plate boundaries. The A^3 triple junction is considered to be unstable and likely to continue migrating to the southwest for the foreseeable geologic future.

INTRODUCTION

Near the Gulf of İskenderun in the eastern Mediterranean Sea, the Africa, Anatolia, and Arabia tectonic plates form an unstable triple junction (referred to here as the A^3 triple junction) along left-lateral transform faults (Fig. 1; Dewey et al., 1986). This instability is associated with significant crustal deformation reflected by broad regions of high seismicity (Ergin et al., 2004), apparent crustal thinning (Abgarmi et al., 2017), and the development of transtensional basins (e.g., Cilicia-Adana-İskenderun and Samandağ-Amik-Karasu-Narlı) and transpressional ranges (e.g., Amanos Mountains) under conditions of complex strain partitioning (Fig. 2; Tatar et al., 2004; Aksu et al., 2005; Seyrek et al., 2007). Within this dynamic setting, small volumes of Quaternary mafic lava occur locally along transform fault segments and/or between rotating crustal blocks within fault zones (Fig. 2; e.g., Tatar et al., 2004; Kavak et al., 2009). Because these near-primary basalts are restricted spatially to transform faults of the developing A^3 triple junction, this magmatism provides a rare opportunity to study melt generation within an exposed and actively developing plate boundary. More generally, the unusual setting of basaltic magmatism along transform faults within continental crust is significant because it provides context for their petrogenesis. Although a rare occurrence within continental crust, such small magmatic centers are known to occur in association with transform faults and fracture zones within oceanic crust (e.g., Hékinian et al., 1995; Perfit et al., 1996), with the potential for large-scale fluid and mineral systems forming along transform faults associated with triple junctions (e.g., Fletcher et al., 2020). Moreover, understanding the regional tectonic implications of triple junctions and their migration

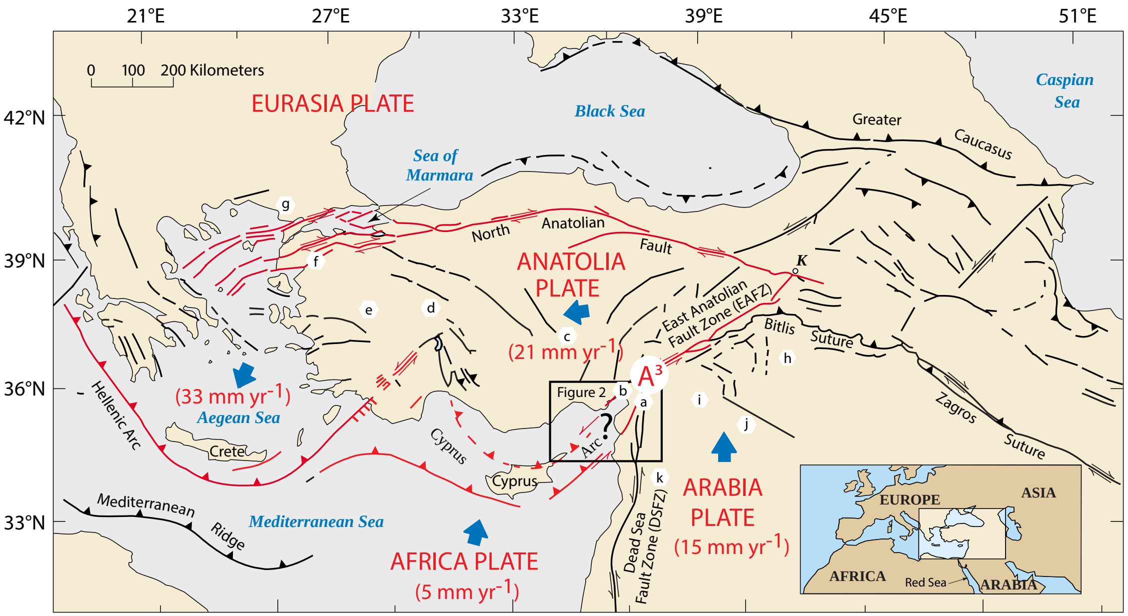

Figure 1. Tectonic map of the eastern Mediterranean region illustrating major tectonic elements, relative fault displacements, and relative plate motions. Faults in red are associated with the tectonic escape and subduction of the Anatolia plate. Faults in black are active and related to regional stress patterns associated with motions of the Africa, Arabia, and Anatolia plates relative to a stable Eurasia. Dominant relative motions of the tectonic plates illustrated by large blue arrows and their relative magnitudes (in mm yr^{-1}) are from geodesy and radar measurements (Reilinger et al., 2006; Mahmoud et al., 2013; Cavalié and Jónsson, 2014; Simão et al., 2016). The approximate area defined by the Africa-Anatolia-Arabia tectonic plate boundary is shown by the circle labeled A^3. Positions of volcanic fields are indicated by letters within white polygons as follows: a—Karasu; b—Toprakkale; c—Cappadocia (central Anatolia); d—Kirka-Afyon (central Anatolia); e—Kula; f—northwest Anatolia; g—Thracia, h—Karacadağ, Diyarbakir (SE Anatolia); i—northwest Syria; j—Harrat Ash Shalam, Syria; k—Dead Sea transform, Syria. K—Karliova. Box inset shows location of Figure 2. Figure is modified from Holzer (2000).

(e.g., Furlong and Schwartz, 2004), including the role of triple junction evolution in the development of escape tectonics, constitutes an important aspect of global tectonics that is not well understood.

Modern-day geophysical methods provide insight into physical heterogeneities within Earth's crust and mantle at depths where magmas are sourced, and this insight is particularly useful for characterizing the genesis of recently erupted near-primary melts (e.g., Plank and Forsyth, 2016; Reid et al., 2019). The integration of geochemical and geophysical data sets furthers our understanding of the chemical, thermal, and physical evolution of tectonically active regions. New data from the U.S. National Science Foundation (NSF) Continental Dynamics–Central Anatolian Tectonics (CD-CAT) seismic deployment (e.g., Abgarmi et al., 2017; Delph et al., 2017; Portner et al., 2018) vastly increased seismic coverage in south-central Anatolia, thus providing unprecedented imaging of physical contrasts in the crust and upper mantle. Geophysical images of the upper mantle beneath southern Anatolia near the A^3 triple junction highlight inferred regions of subducted Neotethyan oceanic lithosphere and the associated African continental margin (Biryol et al., 2011; Abgarmi et al., 2017; Delph et al., 2017; Portner et al., 2018). Lateral changes in Anatolian upper-mantle velocity structure appear to be related to the regional distribution of Quaternary magmatism, such that magmatism near the triple junction is generally restricted to areas underlain by thinner lithosphere (Delph et al., 2017). However, understanding the ways in which these lithospheric-scale contrasts in seismic properties may correlate with the geochemistry of Quaternary volcanic rocks requires a more careful analysis of magma source characteristics.

In this study, we present rock compositions, high-precision $^{40}Ar/^{39}Ar$ geochronology, and radiogenic isotope geochemistry (Sr, Nd, Hf, Pb) data of Quaternary basalts from two volcanic fields proximal to transform fault segments of the A^3 triple junction alongside a compilation of published results, and we compare the integrated data set with seismic images of the uppermost mantle. We demonstrate that the geochemical and geophysical data support magma generation at two distinct depth intervals, consistent with melting of both lithospheric and asthenospheric mantle sources. When placed within the tectonic context of the region, the ascent of these basaltic magmas is likely facilitated by "leaky" transform faults. These results have implications for the timing and position of the developing triple junction, evolution of plate-boundary faults, and tectonic escape of the Anatolia microplate.

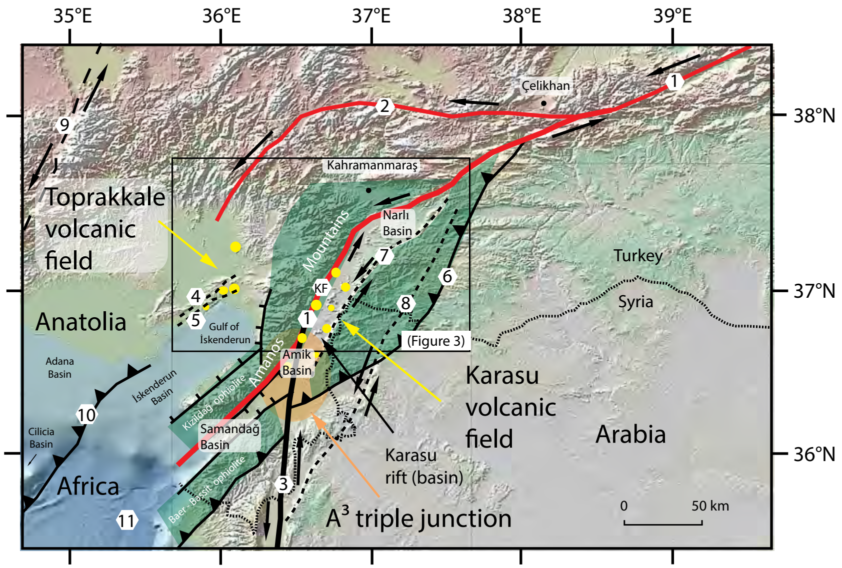

Figure 2. Regional digital elevation map including major geologic and tectonic elements of the study area. Samples for this investigation were collected from Quaternary volcanic deposits of the Toprakkale and Karasu volcanic fields, which are approximately located and highlighted in yellow. The East Anatolian fault zone (EAFZ) is shown in red. The shaded green area represents the exposed, imbricated Late Cretaceous ophiolite and overthrusted Miocene carbonate rocks of the former collisional margin between the Nubian (Arabia-Africa) and Eurasian (Anatolia) plates. The numbers are keyed to the following: (1) main southern strand of the East Anatolian fault zone; (2) northern strand of the East Anatolian fault zone; (3) Dead Sea fault zone (DSFZ); (4) Karataş fault; (5) Yumurtalık fault; (6) limit of Late Cretaceous to late Miocene collisional front (Bitlis suture); (7) Yesemek (East Hatay) fault; (8) Aaferin fault; (9) Central Anatolian (Ecemiş) fault; (10) Kyrenia-Misis fault zone; (11) area of fault transition to the Cyprean arc. Note the transition of the Dead Sea fault zone to the East Anatolian fault zone near the Amik Basin. The Karasu (Amanos) fault segment (KF) of the East Anatolian fault zone is indicated, where it runs along the base of the Amanos Mountains on the west side of the Karasu Basin.

■ TECTONIC SETTING

The tectonic forces controlling movements between the tectonic plates of Anatolia, Africa, and Arabia in the eastern Mediterranean have led to the development of a tectonically complex and unstable triple junction (e.g., Şengör et al., 1985; Perinçek and Çemen, 1990; Rojay et al., 2001; Reilinger et al., 2006). Modern geodesy and radar measurements near the triple junction show relative plate displacements up to 20 mm yr^{-1} (Reilinger et al., 2006; Mahmoud et al., 2013; Cavalié and Jónsson, 2014; Simão et al., 2016). The A^3 triple junction is currently centered near the Amik subbasin within the Karasu rift (Fig. 2; Dewey et al., 1986; Over et al., 2004; Yuce et al., 2014), although other triple junction locations have been proposed owing to the tectonic complexity and distributed deformation within the region (e.g., Karig and Kozlu, 1990; Tarı et al., 2014). The three plates are separated by two major transform fault systems: the left-lateral NE-SW–trending East Anatolian fault zone and the left-lateral N-S–trending Dead Sea fault zone (Fig. 2; Dewey and Şengör, 1979; Rojay et al., 2001; Westaway, 2004; Tatar et al., 2004; Duman and Emre, 2013). Here, both transtension and transpression are recorded in a network of smaller faults subparallel to the plate boundaries (e.g., Kavak et al., 2009). Focal mechanisms between fault zones reflect their complex interplay, showing normal, thrust, and mixed compressional and extensional oblique-slip motion over a large range of depths (Ergin et al., 2004). Within the field area, transtension across a wide region surrounding the A^3 triple junction has resulted in the development of major basins, including the Cilicia-Adana-İskenderun Basins and the Karasu Basin, with its Samandağ, Amik, and Narlı subbasins, located northwest and southeast of the East Anatolian fault zone, respectively (Fig. 2).

The Dead Sea fault zone and the East Anatolian fault zone are neotectonic structures that crosscut an earlier orogenic belt of Late Cretaceous ophiolites, including the Kızıldağ (Amanos) and Baer Bassit ophiolites (Fig. 2). These ophiolites represent the former collision zone (Bitlis suture) between the Nubia (Africa-Arabia) and Eurasia (Anatolia) plates and remnants of the intervening Neotethys oceanic basement. This ophiolite mélange was itself overthrusted during the late Miocene by Jurassic–Cretaceous platform carbonates, equivalent to those exposed in the Kyrenia mountain range in Cyprus, forming an imbricated stack of ophiolite and carbonate rocks (e.g., Şengör and Yılmaz, 1981). Near the Gulf of İskenderun, the transition from a largely compressional tectonic system to one dominated by transtension and transpression developed when rifting in the Red Sea began in the late Miocene, leading to formation of the translational Dead Sea–East Anatolian fault zone system, and finally to tectonic extrusion of the Anatolian plate along the East Anatolian fault zone (e.g., Şengör et al., 1985; Hempton, 1987).

The East Anatolian fault zone has been active since the Pliocene (e.g., McKenzie, 1976; Şengör et al., 1985; Muehlberger and Gordon, 1987), with present-day average left-lateral slip estimated by global positioning system (GPS) data of ~10 mm yr^{-1} (Reilinger et al., 2006). Near the town of Çelikhan, the East Anatolian fault zone splits into two main segments (a northern minor strand and a southern main strand) largely separated by the Amanos Mountains (Fig. 2; Duman and Emre, 2013). The Amanos Mountains, an ~2300-m-elevation range, represent an uplifted block of Precambrian-cored continental crust within a major zone of transpression, and, despite its position between the two major strands of the East Anatolian fault zone, it contains few mapped Quaternary faults. This apparent tectonic rigidity is consistent with its relatively recent and coherent uplift since 4 Ma (Seyrek at al., 2008), and the stark relief of the Amanos Mountains relative to the low-relief Arabian margin suggests a strong asymmetry in structural deformation and differential crustal uplift (e.g., Rojay et al., 2001; Reilinger et al., 2006).

The main southern strand of the East Anatolian fault zone extends ~580 km from the so-called Karlıova triple junction in the east, where it joins the North Anatolian fault, to the Amik Basin in the west (Rojay et al., 2001; Westaway, 2004; Kavak et al., 2009; Duman and Emre, 2013). The Amik Basin (Fig. 2) approximately coincides with the northern termination of the Dead Sea fault zone, which accommodates ~5 mm yr^{-1} of left-lateral motion between the Africa and Arabia plates (Reilinger et al., 2006; Mahmoud et al., 2013), and its continuation as the main southern strand of the East Anatolian fault zone (e.g., Arpat and Şaroğlu, 1972; Rojay et al., 2001; Westaway, 2004; Kavak et al., 2009; Duman and Emre, 2013). Where the East Anatolian fault zone transits the Karasu valley (also referred to as rift, trough, basin, or graben), it is characterized by a diffuse network of individual fault segments comprising several restraining and releasing bends (Duman and Emre, 2013). The Karasu valley is bordered on its western margin by the Amanos Mountains and the east-dipping Karasu (Amanos) fault zone, and on its eastern margin by the west-dipping Yesemek (East Hatay) fault zone (Fig. 2; Rojay et al., 2001; Seyrek et al., 2008; Duman and Emre, 2013). Farther to the southeast, the Aaferin fault represents a major fault splay of the Dead Sea fault zone that roughly parallels the Karasu valley before linking with the main strand of the East Anatolian fault zone near the town of Kahramanmaraş (Fig. 2).

The northern segment of the East Anatolian fault zone diverges from its main segment near the village of Çelikhan, continuing ~350 km toward the Gulf of İskenderun. Similar to the main southern strand of the East Anatolian fault zone, the northern strand consists of several individual fault segments connected by releasing and restraining bends and ultimately projecting offshore on strike toward the Kyrenia-Misis fault zone (Fig. 2; Duman and Emre, 2013). Both the northern and southern strands of the East Anatolian fault zone project offshore into the Mediterranean, likely connecting to major fault networks associated with the Cyprean trench (e.g., Duman and Emre, 2013), where strike-slip deformation linked to the interaction of the three plates gives way to compressional deformation related to the northward movement of the Africa plate (e.g., Imprescia et al., 2012). The northern strand of the East Anatolian fault zone becomes diffuse as it approaches the Gulf of İskenderun; deformation is distributed across smaller faults within a broad zone of transtension. Along the northern margin of the gulf, two subparallel fault segments, the Karataş and Yumurtalık faults (Fig. 2), both predominantly sinistral strike-slip faults with some reversed throw, can be considered as examples of small discontinuous faults that are part of a much broader network of transtensional structures. The Karataş and Yumurtalık faults were previously referred to as the Karataş-Osmaniye fault (e.g., McKenzie, 1976), and they have often been considered to be the boundary between Anatolian and African lithosphere (e.g., Parlak et al., 1997; Gürsoy et al., 2003; Westaway, 2003, 2004; Seyrek et al., 2008; Kavak et al., 2009).

QUATERNARY (LEAKY TRANSFORM) VOLCANISM ALONG THE EAST ANATOLIAN FAULT ZONE

There are two small Quaternary volcanic fields (here referred to as the Toprakkale and Karasu volcanic fields) locally occurring along and/or near both the northern and southern fault segments of the East Anatolian fault zone (Figs. 2 and 3); they consist of volcanic cones, lava flows, and ash-fall deposits (e.g., Parlak et al., 1997, 1998; Yurtmen et al., 2000; Rojay et al., 2001; Alıcı et al., 2001; Kavak et al., 2009). Quaternary volcanic rocks along the East Anatolian fault zone are neither voluminous nor widespread and are absent west of the İskenderun Basin and similarly absent northeast of Fevzipaşa along the main strand of the East Anatolian fault zone (Fig. 3).

Toprakkale Volcanic Field

The Toprakkale volcanic field refers to all of the Quaternary volcanic centers and lava flows of the Ceyhan-Osmaniye-Erzin-Toprakkale region, including the basaltic ash-fall deposits along the northern shore of the Gulf of İskenderun near İncirli (Fig. 3; e.g., Polat et al., 1997; Arger et al., 2000; Yurtmen et al., 2000; Bağcı et al., 2011; Italiano et al., 2017; Oyan, 2018). Volcanism in the Toprakkale volcanic field is spatially associated with the roughly parallel NE-SW–trending Karataş and Yumurtalık faults and a small stepover near the Delihalil volcano represented by the Toprakkale fault (Duman and Emre, 2013).

Published $^{40}Ar/^{39}Ar$ and K-Ar ages between 2.3 and 0.1 Ma for basalts in the Toprakkale volcanic field (Arger et al., 2000; Oyan, 2018) are consistent with paleomagnetic studies of volcanic rocks along the northern strand of the East Anatolian fault zone that have both normal and reversed polarities (Gürsoy et al., 2003). The Toprakkale volcanic rocks are mafic, with high combined alkalis ($Na_2O + K_2O$), and they plot as basanites and mostly alkaline basalts (Fig. 4). Relative to primitive mid-ocean-ridge basalts (MORB), they are enriched in light rare earth elements (LREEs), large ion lithophile elements (LILEs), and high field strength elements (HFSEs; e.g., Polat et al., 1997; Arger et al., 2000; Yurtmen et al., 2000; Bağcı et al., 2011). Values of $^{87}Sr/^{86}Sr$ and $^{143}Nd/^{144}Nd$ are consistent with derivation from an ocean-island basalt (OIB)–like asthenospheric mantle source together with some component of partial melting of lithospheric mantle. Trace-element differences between the basanites and alkaline basalts have been argued to indicate differential degrees of lithospheric mantle partial melting (1.5%–4.6% vs. 9.2%; Bağcı et al., 2011; Oyan, 2018).

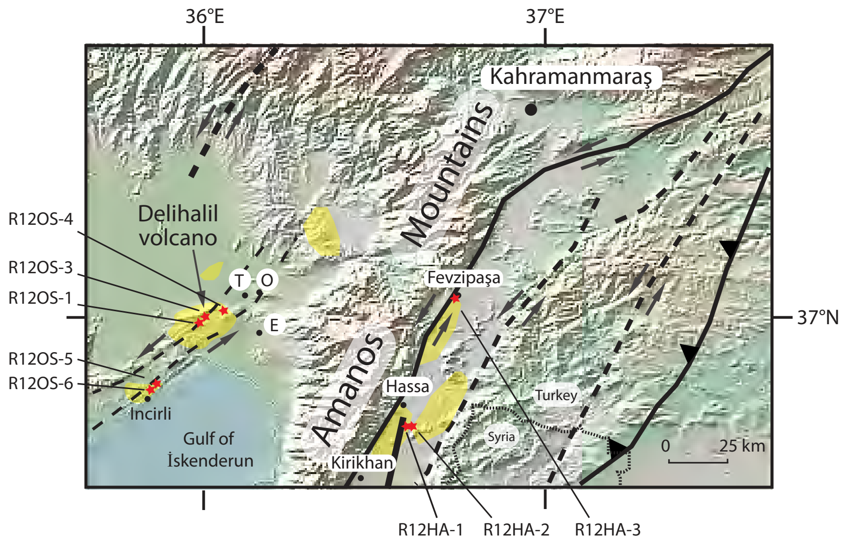

Figure 3. Inset from Figure 2 showing sample locations and the overall distribution of major faults and Quaternary volcanic rocks between the main and northern strands of the East Anatolian fault zone. Samples from the Karasu volcanic field occur within the Amik subbasin of the Karasu rift (basin, trough, or graben), where the Dead Sea fault zone merges(?) with the East Anatolian fault zone. The transtensional nature of the field area is expressed by basin development including the Karasu, Amik, İskenderun, and Narlı basins, and transpression expressed by uplift of the Amanos Mountains. The Toprakkale volcanic field includes all Quaternary volcanic rocks of the Ceyhan-Osmaniye (O)-Erzin (E)-Toprakkale (T) and immediately surrounding areas (see location on Fig. 11). Samples R12OS-1 and R12OS-3 are located near the summit and flank, respectively, of Delihalil volcano. Samples from the Karasu volcanic field (R12HA-1 through R12HA-3) are associated with different segments of the Karasu fault segment of the East Anatolian fault zone.

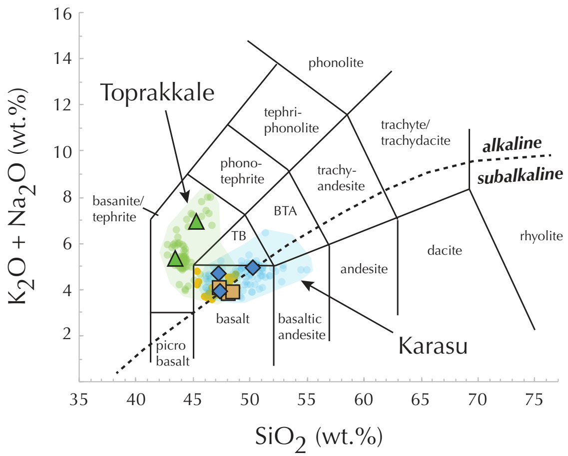

Figure 4. Compositions of samples from the Toprakkale and Karasu volcanic fields on a total alkali vs. silica (TAS) diagram (after Le Maitre et al., 1989), with the alkaline-subalkaline fields also indicated (Irvine and Baragar, 1971). Data from this study are colored and outlined in black (green triangles—basanite from Delihalil volcano; orange squares—alkali basalt from Toprakkale; blue diamonds—basalt from Karasu volcanic field). Colored circles represent data from other studies, with green and blue shaded fields encompassing the range of rock compositions from the Toprakkale and Karasu volcanic fields, respectively. TB—trachybasalt; BTA—basaltic trachyandesite.

Karasu Volcanic Field

The Karasu volcanic field includes all localized Quaternary lava flows and vents in the Amik Basin, a subbasin within the Karasu rift that is exposed over a distance of ~60 km between Kırıkhan and Fevzipaşa (Figs. 2 and 3; Rojay et al., 2001). Northeast of Fevzipaşa, a tectonic saddle separates the Amik and Narli subbasins, which contain either Quaternary (Amik) or Miocene (Narlı) volcanic rocks (Rojay et al., 2001). Borehole data within the Karasu valley are consistent with sedimentation and volcanism occurring throughout much of the Quaternary, as the Karasu valley continues to act as a zone of active infilling, with sag structures (subbasins) consistent with active transpression and intermittent basaltic volcanism (Rojay et al., 2001).

When plotted on a conventional total alkali versus SiO_2 rock discrimination plot (Fig. 4), the volcanic rocks from the Karasu volcanic field straddle the boundary between the alkaline and subalkaline fields (Irvine and Baragar, 1971), which represents the low-pressure thermal divide defined by olivine-clinopyroxene-plagioclase stability. Fractional crystallization of any of these phases would drive the residual magma away from the divide, indicating that the Karasu basalts show evidence for both feldspathoid-normative and quartz-normative compositions. In notable contrast with the Toprakkale volcanic field, no basanites have been described from the Karasu volcanic field, but both alkali olivine basalts and quartz- or olivine-tholeiites have been described (Çapan et al., 1987; Alıcı et al., 2001). Any petrogenetic signature is poorly resolved in the geochemical and isotopic data, with, for example, $^{87}Sr/^{86}Sr$ and $^{143}Nd/^{144}Nd$ values showing considerable overlap. The wide range in $^{87}Sr/^{86}Sr$ (0.703353–0.705490) and trace-element compositions could indicate crustal contamination in many of the samples from the Karasu valley (Alıcı et al., 2001).

SAMPLES

Eight samples of fresh volcanic rock were collected from the volcanic fields, five from the Toprakkale volcanic field and three from the Karasu volcanic field, in July 2012 (Fig. 3). All of the samples were either directly or proximally associated with fault segments of the East Anatolian fault zone. Within the Toprakkale volcanic field, samples of dark basaltic rock were collected from outcrops including near the summit of the Quaternary Delihalil volcano (R12OS-1; Fig. 5A), along the flank of Delihalil (R12OS-3; Fig. 5B), and outside the town of Toprakkale (R12OS-4; Fig. 5C). Additional samples were collected from layered volcanic flow and ash deposits that occur along the northern margin of the Gulf of İskenderun, in the vicinity of the Yumurtalık fault (R12OS-5, R12OS-6; Fig. 5D). Within the Karasu volcanic field, two samples were collected near the village of Hassa, along the Karasu (Amanos) fault segment of the southern strand of the East Anatolian fault zone (Fig. 3). Sample R12HA-1 (Fig. 5E) was collected from a fresh lava flow exposed near a flowing creek bed, and sample R12HA-02 (Fig. 5F) was collected from stratigraphically overlying fresh lava. Sample R12Ha-03 was collected near the village of Fevzipaşa. Samples R12HA-1 and R12HA-2 were collected in an area where several small volcanic centers (Büyük, Güvenç, Hassa, Bosalan) occur, possibly within local dilational zones ("spenochasms"; Tatar et al., 2004) formed in response to differential stress along the East Anatolian fault zone. These sample sites are within the much larger regional K-Ar geochronology study by Rojay et al. (2001) and were collected to try to gain better precision on the ages from this area. Specific sampling procedures corresponding to different analytical methods are described below.

METHODS

Rock Chemistry

Surficial contamination was removed from rock samples by extensive rinsing in water, followed by a sequence of 5–10 min of ultrasonication that progressed from dilute (~2%) hydrogen peroxide to dilute (~0.01 *N*) hydrochloric acid, with intermediate and final steps in distilled water. Major- and trace-element concentrations (Table 1) were determined on rock powders by quantitative X-ray fluorescence spectrometry, inductively coupled plasma–mass spectrometry, and inductively coupled plasma–atomic emission mass spectrometry. Samples for this investigation were analyzed by SGS Minerals in Lakefield, Ontario, Canada.

$^{40}Ar/^{39}Ar$ Analyses

The $^{40}Ar/^{39}Ar$ analyses were performed at the U.S. Geological Survey (USGS) in Denver, Colorado. Fresh rock fragments ~3 mm^3 in size were prepared by crushing, washing in deionized water, and handpicking. Together with the neutron fluence monitor Fish Canyon sanidine, samples were loaded into precise positions within 18 mm Al disks, stacked, wrapped in Al foil, and encapsulated under vacuum in a quartz tube. The quartz tube was sealed into an Al canister and rotated at 1 rpm during neutron irradiation for 11 MWh in the central thimble position of the USGS TRIGA reactor (Dalrymple et al., 1981). Following irradiation, the samples and fluence monitors were loaded with tweezers into a stainless-steel sample holder and then placed into a laser chamber with an externally pumped ZnSe window, which was attached to a custom-built ultrahigh-vacuum extraction line. The volume of the mostly stainless-steel vacuum extraction line, including a cryogenic trap operated at −130 °C and two SAES™ GP50 getters (one at room temperature and one operated at 2 A [amperes]), is estimated at ~450 cm^3. A combination of turbo molecular pumps and ion pumps maintained steady pressures within the extraction line of <1.33×10^{-7} Pa. Samples were incrementally heated in steps of 90 s by controlled power output of a 50 W CO_2 laser equipped with a beam-homogenizing lens, resulting in uniform energy over the entire sample surface. The reported incremental heating data represent results from individual mineral grains. During laser heating, any sample gas released was exposed to the cryogenic trap and was further purified for an additional 120 s by exposure to both the cryogenic trap and the SAES getters. The sample gas was expanded into a Thermo Scientific ARGUSVI™ mass spectrometer, and argon isotopes were analyzed simultaneously using four Faraday detectors (^{40}Ar, ^{39}Ar, ^{38}Ar, ^{37}Ar)

Figure 5. Photographs of selected sample locations. (A) Sample locality R12OS-1, near the summit of Delihalil volcano, a Quaternary volcano erupting basanite lavas. (B) Sample locality R12OS-3, from the flank of Delihalil volcano. (C) Sample locality R12OS-4, outside the town of Toprakkale. (D) View to the northeast, near sample localities R12OS-5 and R12OS-6, along the northern margin of the Gulf of İskenderun (Mediterranean Sea in background). Note the multiple layers of air-fall deposits. (E) View to the southeast from sample locality R12HA-1, within Karasu valley. (F) View to the southeast from sample locality R12HA-2, showing fresh lava flows stratigraphically above those of sample R12HA-1. Pine trees in background for scale.

TABLE 1. WHOLE-ROCK MAJOR AND TRACE ELEMENT DATA

Sample:	R12 OS 01	R12 OS 03	R12 OS 04	R12 OS 05	R12 OS 06	R12 HA 01	R12 HA 02	R12 HA 03
Latitude (°N):	37.015	37.023	37.029	36.905	36.901	36.732	36.732	37.063
Longitude (°E):	36.067	36.078	36.128	35.955	35.945	36.529	36.543	36.621
Rock type:	Basanite	Basanite	Basalt	Basalt	Basalt	Basalt	Basalt	Basalt
SiO_2	45.3	43.5	47.4	48.5	48.2	47.4	47.2	50.2
TiO_2	2.82	3.04	2.02	1.8	1.85	2.4	2.44	2.16
Al_2O_3	15.9	14.4	15.4	15.3	15.1	16.1	15.4	16.5
Fe_2O_3	11.8	13.4	12.7	12.9	12.9	12.8	13.1	11.6
Cr_2O_3	0.01	0.05	0.04	0.05	0.05	0.03	0.04	0.03
MnO	0.17	0.18	0.16	0.17	0.17	0.18	0.16	0.16
MgO	7.86	9.34	7.92	8.74	8.62	6.99	8.05	5.59
CaO	8.28	9.92	10.2	9.73	9.71	10.5	9.62	8.33
Na_2O	4.56	3.83	3.25	3.26	3.19	3.07	3.51	3.55
K_2O	2.41	1.53	0.81	0.6	0.61	0.86	1.19	1.39
P_2O_5	0.85	1.04	0.36	0.36	0.37	0.4	0.44	0.4
LOI	1.12	0.522	0.482	<0.01	<0.01	0.171	<0.01	0.354
Sum	99.96	100.23	100.26	101.41	100.77	100.73	101.15	99.91
Ag	<1	<1	<1	<1	<1	<1	<1	<1
As	<30	<30	<30	<30	<30	<30	<30	<30
Ba	275	308	183	184	208	194	287	331
Be	<5	<5	<5	<5	<5	<5	<5	<5
Bi	<0.1	<0.1	<0.1	<0.1	<0.1	<0.1	<0.1	<0.1
Cd	<0.2	<0.2	<0.2	<0.2	<0.2	<0.2	<0.2	<0.2
Ce	78.6	81.6	40.7	48.8	51.1	37.2	45.8	55.8
Co	39.4	44.1	46.3	48.1	48	43.6	47.2	39.4
Cr	140	210	280	310	310	160	230	100
Cs	0.2	0.1	0.4	<0.1	<0.1	<0.1	0.3	0.1
Cu	45	58	50	29	41	54	58	16
Dy	5.23	4.89	4.05	3.84	3.85	4.29	4.5	5.63
Er	2.65	2.16	1.93	1.98	2.03	2.11	2.32	2.92
Eu	2.38	2.56	1.64	1.61	1.62	1.87	1.89	2.04
Ga	19	18	19	19	19	20	21	23
Gd	6.92	7.08	4.83	4.74	4.69	5.14	5.55	6.36
Ge	<1	<1	1	1	1	1	1	1
Hf	7	4	3	3	3	3	4	5
Ho	1	0.86	0.76	0.75	0.76	0.81	0.87	1.08
In	<0.2	<0.2	<0.2	<0.2	<0.2	<0.2	<0.2	<0.2
La	41.5	41.6	21.1	26.8	28.6	18	22.6	28.2
Li	<10	<10	<10	<10	<10	<10	<10	10
Lu	0.33	0.22	0.23	0.23	0.23	0.23	0.28	0.38
Mo	4	3	<2	<2	<2	<2	<2	2
Nb	49	45	16	16	16	17	27	26
Nd	38.2	39.9	20.5	22.6	23.8	21.5	24.8	30.6
Ni	111	150	126	137	144	88	122	33
Pb	<5	<5	<5	<5	<5	<5	<5	7
Pr	9.78	10.2	5.05	5.82	6.08	5.01	6.02	7.32
Rb	24.2	15.2	8.1	7.5	6.4	11.4	20	22.7
Sb	0.2	<0.1	<0.1	0.1	0.1	0.1	<0.1	0.3
Sc	20	20	23	22	23	25	24	25
Sm	7	7.5	4.5	4.6	4.4	4.6	5.2	6.1
Sn	2	2	1	1	<1	1	2	2
Sr	919	1060	587	556	589	591	649	587
Ta	3.5	2.8	1	1	1.1	1.2	1.8	1.7
Tb	0.96	0.93	0.69	0.68	0.69	0.77	0.8	0.94
Th	5	3.3	2.2	3.7	3.9	2.1	2.2	4.4
Tl	<0.5	<0.5	<0.5	<0.5	<0.5	<0.5	<0.5	<0.5
Tm	0.36	0.27	0.27	0.28	0.26	0.28	0.3	0.4
U	1.6	1.12	0.63	0.88	0.64	0.67	0.73	1.07
V	178	187	197	191	200	229	215	217
W	<1	<1	<1	<1	<1	<1	<1	<1
Y	25	21.9	18.9	18.8	18.8	20.3	22	27.7
Yb	2.2	1.7	1.6	1.6	1.6	1.7	1.9	2.5
Zn	92	91	111	106	109	103	97	102
Zr	284	180	113	110	109	118	150	190

Note: Major elements are in weight percent, and trace elements are in parts per million. LOI—loss on ignition.

and one ion counter (^{36}Ar). Following data acquisition of 10 min, time zero intercepts were fit to the data (using parabolic and/or linear best fits) and corrected for backgrounds, detector intercalibrations, and nucleogenic interferences. The mass spectrometer computer program written by A. Deino of the Berkeley Geochronology Center was used for data acquisition, age calculations, and plotting. All $^{40}Ar/^{39}Ar$ ages reported in Table 2 are referenced to an age of 28.201 ± 0.046 Ma for the Fish Canyon sanidine (Kuiper et al., 2008), the decay constants of Min et al. (2000), and an atmospheric $^{40}Ar/^{36}Ar$ ratio of 298.56 ± 0.31 (Lee et al., 2006). Laser fusion of >10 individual Fish Canyon Tuff sanidine crystals at each closely monitored position within the irradiation package resulted in neutron flux ratios reproducible to ~0.25% (2σ). Isotopic production ratios were determined from irradiated CaF_2 and KCl salts, and the following values were measured for this study: $(^{36}Ar/^{37}Ar)_{Ca} = (2.4 \pm 0.05) \times 10^{-4}$; $(^{39}Ar/^{37}Ar)_{Ca} = (6.59 \pm 0.10) \times 10^{-4}$; and $(^{38}Ar/^{39}Ar)_K = (1.29 \pm 0.03) \times 10^{-2}$. Cadmium shielding during irradiation prevented any measurable $(^{40}Ar/^{39}Ar)_K$. The $^{40}Ar/^{39}Ar$ plateau ages (and uncertainties) are considered to be the best estimate of the cooling age of the minerals and were calculated from samples if three or more consecutive heating steps released >50% of the total ^{39}Ar and also had statistically (2σ) indistinguishable $^{40}Ar/^{39}Ar$ ages.

Sr, Nd, Hf, and Pb Isotope Analyses

The analytical techniques used for Pb-Sr-Nd isotopic systematics on whole-rock powders at the USGS were similar to those reported by Tatsumoto and Unruh (1976) and more recently by Premo and Loucks (2000) and Premo and Taylor (2010). The whole-rock powders were dissolved in 7 mL perfluoroalkoxy Teflon™ vials with ultrapure concentrated HF + HNO_3 while heating to ~150 °C on a hot plate for at least 5 d. Lead was extracted from the dissolved effluent using AG1-X8 anion-exchange resin in Teflon columns and a very dilute HBr medium. The Pb laboratory contamination (blank) varied between 60 and 300 pg during the analytical session. Strontium and rare earth elements (REEs) were separated from the rest of the sample using a 30-mL-volume cation-exchange column (Birck and Allégre, 1978), while Sm was separated from Nd using the α-isobutyric method of Lugmair et al. (1975). Sr and Nd blanks were less than 300 pg each.

Pb, Sr, and Nd isotopic measurements were conducted using a Triton™ (Thermo-Fisher Scientific) nine-collector mass spectrometer, which was operated with a 10 kV acceleration voltage and 10^{11} Ω resistors for the Faraday cups. Pb residues were redissolved in H_3PO_4 and loaded onto single Re filaments. The measured Pb isotopic ratios were corrected using the algorithms and programming of Ludwig (1980, 1985) for laboratory blanks with measured compositions of $^{206}Pb/^{204}Pb = 19.34 \pm 0.53$, $^{207}Pb/^{204}Pb = 15.53 \pm 0.08$, and $^{208}Pb/^{204}Pb = 38.11 \pm 0.20$, and instrumental mass fractionation (0.08% ± 0.03% per a.m.u.) as determined from multiple runs of the NIST Pb standards SRM-981 and SRM-982.

Between 500 and 1000 ng aliquots of Sr and Nd were loaded separately on outgassed Re filaments with a Ta_2O_5 activator. Within-run 1 standard error (SE) values for conventionally fractionation-corrected isotope ratios using accepted $^{88}Sr/^{86}Sr$ = 8.375209 typically were ~0.0004% for $^{87}Sr/^{86}Sr$ and ~0.002% for $^{84}Sr/^{86}Sr$ in unspiked samples. Unspiked NIST $SrCO_3$ standard SRM-987 was run after each five unknowns, and its average value was used to determine a normalization factor (*F*) for measured $^{87}Sr/^{86}Sr$ values as $F = (^{87}Sr/^{86}Sr_{Measured})/0.710248$. The long-term weighted average for the NIST-corrected $^{87}Sr/^{86}Sr$ value in the USGS carbonate standard EN-1 (giant clam shell) was 0.709176 ± 0.000002 ($n = 31$, mean square of weighted deviates [MSWD] = 0.82, probability of fit = 0.74). Measured $^{143}Nd/^{144}Nd$ data were normalized to $^{146}Nd/^{144}Nd$ = 0.7219 and monitored for instrumental bias using the JNd-1 Nd standard (Tanaka et al., 2000). A mean $^{143}Nd/^{144}Nd$ value of 0.512087 ± 0.00006 (2SE%) was obtained during the same runs, and the average of two JNdi-1 analyses was 0.512085 ± 0.0006 (2SE%).

Hf and duplicate Pb isotope analyses were performed at the Ecole Normale Supérieure in Lyon (ENSL), France, on the same whole-rock powders as those used for USGS chemical and isotopic analyses. In this case, an ~600 mg aliquot of whole-rock powder was leached in high-purity 6 M HCl in stages alternating between heating to 125 °C and ultrasonication. The total duration of leaching was 50 min. The leachate was decanted, and the residue was washed repeatedly in ultrapure water before digestion in double-distilled concentrated HNO_3 and HF in proportions of 1:3. After evaporation, Hf was leached from the digested residue using high-purity concentrated HF and separated first from the remaining sample matrix and then from Ti using a two-stage chromatographic procedure (Blichert-Toft et al., 1997). The Ca-Mg fluoride precipitate remaining after the HF-leaching step was dissolved in double-distilled 6 M HCl, evaporated to dryness, and then converted to bromides. Pb was separated from this solution on a 500 μL AG1-X8 anion-exchange column using dilute HBr to elute the sample matrix and 6 M HCl to collect the Pb.

Isotopic analyses were performed at ENSL on a Nu Plasma 500 HR multiple-collector–inductively coupled plasma–mass spectrometer. Groups of two to four Hf isotope analyses were bracketed by analyses of the JMC-475 Hf standard. Results were normalized for instrumental mass fractionation using an exponential law relative to $^{179}Hf/^{177}Hf$ = 0.7325. The JMC-475 Hf standard run in alternation in the session with the unknowns yielded $^{176}Hf/^{177}Hf$ = 0.282158 ± 0.000004 (2 standard deviation [sd]; $n = 11$). Pb was analyzed using Tl doping (5 ppb) and sample-standard bracketing (White et al., 2000), wherein the NIST 981 Pb standard was run systematically after every second sample. Analyses were normalized to the values of Eisele et al. (2003). External 2σ reproducibility of $^{206}Pb/^{204}Pb$, $^{207}Pb/^{204}Pb$, and $^{208}Pb/^{204}Pb$ was ±100–200 ppm (or 0.01%–0.02%), while that of $^{207}Pb/^{206}Pb$ and $^{208}Pb/^{206}Pb$ was ±50 ppm (or 0.005%). Internal run errors on all Pb isotope ratios were better than the external reproducibility. Hf and Pb blanks were <20 pg. The Sr, Nd, Hf, and Pb isotope data are listed in Table 3.

RESULTS

Petrography and Rock Geochemistry

Petrographic inspection of the samples revealed fresh basalts with phenocrysts of olivine and

TABLE 2. ANALYTICAL RESULTS OF CO_2-LASER INCREMENTAL HEATING $^{40}Ar/^{39}Ar$ EXPERIMENT

Run_ID	Sample	Material	CO_2 laser power (W)	^{40}Ar (fA)	^{40}Ar (fA) σ	^{39}Ar (fA)	^{39}Ar (fA) σ	^{38}Ar (fA)	^{38}Ar (fA) σ	^{37}Ar (fA)	^{37}Ar (fA) σ	^{36}Ar (fA)	^{36}Ar (fA) σ	Ca/K	%^{40}Ar rad	Age (Ma)	Age (Ma)	^{39}Ar moles	Irradiation	J	J σ	Isochron $^{36}Ar/^{40}Ar$	Percent initial $^{36}Ar/^{40}Ar$ error	Isochron $^{39}Ar/^{40}Ar$	Percent initial $^{39}Ar/^{40}Ar$ error	Percent initial $^{39}Ar/^{36}Ar$ error	Correlation coefficient $^{40}Ar/^{39}Ar$	Correlation coefficient $^{36}Ar/^{39}Ar$
865-02A	R12 OS01	Whole rock	0.1	−0.1990	0.3983	0.0064	0.2282	−0.0089	0.1472	0.0395	0.1358	−0.0003	0.0015	20.99481	58.33556	−1.994806	72.89487	1.94E-19	DT-15a	0.0000593	2.73E-06	0.00140	589.99580	−0.03173	−3620.00800	−3656.90400	0.14277	0.01876
865-02B	R12 OS01	Whole rock	0.3	−0.5635	0.3983	0.2092	0.2293	−0.0015	0.1455	0.1006	0.1361	−0.0001	0.0015	1.624895	93.59872	−0.2735001	0.4346668	6.38E-18	DT-15a	0.0000593	2.73E-06	0.00021	1270.86500	−0.37116	−130.45660	−1273.64100	0.99475	0.03014
865-02C	R12 OS01	Whole rock	0.5	−0.4188	0.3992	−0.0834	0.2313	−0.0214	0.1472	0.0109	0.1370	0.0006	0.0015	−0.4435368	140.0848	0.7628916	2.260844	−2.54E-18	DT-15a	0.0000593	2.73E-06	−0.00134	−291.63750	0.19909	293.41070	−391.14530	0.66601	0.10616
865-02D	R12 OS01	Whole rock	0.7	6.2740	0.4052	0.1492	0.2282	−0.0942	0.1463	0.0778	0.1367	0.0222	0.0016	1.76375	−5.575563	−0.2543508	0.5992777	4.55E-18	DT-15a	0.0000593	2.73E-06	0.00354	9.68535	0.02377	153.15230	153.18530	0.03511	0.02812
865-02E	R12 OS01	Whole rock	0.9	66.9007	0.3989	3.1154	0.2285	0.1656	0.1472	1.1011	0.1374	0.2210	0.0023	1.195619	1.596568	0.0371884	0.0281646	9.50E-17	DT-15a	0.0000593	2.73E-06	0.00330	1.21823	0.04656	7.36034	7.41257	0.12496	0.03966
865-02F	R12 OS01	Whole rock	1.1	56.8115	0.4026	4.5999	0.2287	0.1828	0.1460	1.4236	0.1374	0.1865	0.0024	1.047153	2.308473	0.0309245	0.0194735	1.40E-16	DT-15a	0.0000593	2.73E-06	0.00327	1.47525	0.08095	5.02452	5.13971	0.22078	0.06776
865-02G	R12 OS01	Whole rock	1.3	25.5533	0.3943	4.3011	0.2287	0.0655	0.1472	1.2142	0.1356	0.0793	0.0020	0.9554494	7.975068	0.0513889	0.0182073	1.31E-16	DT-15a	0.0000593	2.73E-06	0.00308	2.96389	0.16830	5.53888	5.89061	0.36677	0.14503
865-02H	R12 OS01	Whole rock	1.5	15.9954	0.3941	3.1890	0.2382	0.0384	0.1482	0.9701	0.1367	0.0520	0.0019	1.029836	3.625197	0.019722	0.0231411	9.72E-17	DT-15a	0.0000593	2.73E-06	0.00323	4.35154	0.19934	7.86866	8.28867	0.35664	0.17733
865-02I	R12 OS01	Whole rock	1.7	12.7708	0.3939	2.7501	0.2277	0.0100	0.1478	0.9564	0.1364	0.0408	0.0017	1.17764	5.579742	0.0281051	0.0256919	8.38E-17	DT-15a	0.0000593	2.73E-06	0.00316	5.27115	0.21530	8.83757	9.31968	0.37196	0.20418
865-02J	R12 OS01	Whole rock	1.9	11.5117	0.3935	2.0762	0.2274	0.0142	0.1485	0.7251	0.1377	0.0373	0.0017	1.182981	4.099094	0.0246533	0.0337677	6.33E-17	DT-15a	0.0000593	2.73E-06	0.00321	5.74768	0.18032	11.47894	11.89229	0.31239	0.17706
865-02K	R12 OS01	Whole rock	2.5	36.2308	0.3947	2.5178	0.2269	−0.0198	0.1488	1.4024	0.1358	0.1135	0.0021	1.887067	6.956182	0.1086014	0.0338917	7.68E-17	DT-15a	0.0000593	2.73E-06	0.00312	2.19198	0.06946	9.08431	9.21695	0.17906	0.05961
865-02L	R12 OS01	Whole rock	3.0	33.6497	0.3994	2.1678	0.2274	−0.0290	0.1466	1.1017	0.1356	0.1079	0.0021	1.722307	4.68274	0.0788589	0.0386806	6.61E-17	DT-15a	0.0000593	2.73E-06	0.00319	2.32360	0.06440	10.56405	10.68537	0.16072	0.05739
865-02M	R12 OS01	Whole rock	4.0	527.8910	0.4254	16.7281	0.2502	0.4728	0.1478	11.7661	0.1364	1.7455	0.0065	2.384175	1.559082	0.0533883	0.0129882	5.10E-16	DT-15a	0.0000593	2.73E-06	0.00330	0.38426	0.03167	1.49924	1.54348	0.23800	0.01127
865-02N	R12 OS01	Whole rock	5.0	197.7330	0.4080	8.6706	0.2277	0.2398	0.1460	7.7884	0.1367	0.6527	0.0036	3.045531	1.930875	0.0477925	0.0145795	2.64E-16	DT-15a	0.0000593	2.73E-06	0.00328	0.59690	0.04381	2.63661	2.68751	0.19555	0.02706
865-02O	R12 OS01	Whole rock	6.0	66.3060	0.3998	3.3720	0.2290	0.1238	0.1466	3.5221	0.1353	0.2185	0.0027	3.542323	2.270049	0.0484556	0.0295538	1.03E-16	DT-15a	0.0000593	2.73E-06	0.00327	1.40173	0.05081	6.82604	6.91601	0.16517	0.03800
Plateau age = 0.046 ± 0.013 Ma, steps A–O, MSWD = 0.6, 100% of ^{39}Ar. Integrated age = 0.04 ± 0.2 Ma.																												
882-02A	R12 OS03	Whole rock	0.1	−0.1766	0.3935	−0.1841	0.2290	−0.1907	0.1458	0.0788	0.1370	−0.0013	0.0015	−1.471781	−127.8145	−0.1312344	0.3842189	−5.61E-18	DT-15c	0.0000585	2.91E-06	0.00763	249.37440	1.04314	255.13900	167.35210	0.30072	0.78014
882-02B	R12 OS03	Whole rock	0.3	−0.1670	0.3985	−0.1885	0.2307	0.0553	0.1460	−0.0238	0.1364	−0.0004	0.0015	0.4349875	25.36001	0.0240664	0.344612	−5.75E-18	DT-15c	0.0000585	2.91E-06	0.00250	435.53870	1.12857	268.21940	384.35140	0.79295	0.48749
882-02C	R12 OS03	Whole rock	0.5	−0.5906	0.3977	0.0310	0.2293	−0.0061	0.1472	0.0099	0.1350	−0.0010	0.0015	1.104068	47.02257	−0.9600012	7.404042	9.45E-19	DT-15c	0.0000585	2.91E-06	0.00177	159.34140	−0.05247	−743.03890	−753.96020	0.17359	0.03830
882-02D	R12 OS03	Whole rock	0.7	1.6306	0.3992	0.1250	0.2406	0.1043	0.1469	0.0444	0.1361	0.0065	0.0015	1.222999	−18.37057	−0.2567734	0.72039	3.81E-18	DT-15c	0.0000585	2.91E-06	0.00396	34.26463	0.07663	194.12610	194.06000	0.08645	0.09009
882-02E	R12 OS03	Whole rock	0.9	105.5190	0.4052	3.4394	0.2456	0.2053	0.1472	1.1365	0.1364	0.3513	0.0033	1.137094	0.7295749	0.0239766	0.0334662	1.05E-16	DT-15c	0.0000585	2.91E-06	0.00333	1.02341	0.03259	7.15521	7.20753	0.12200	0.02014
882-02F	R12 OS03	Whole rock	1.1	133.5860	0.4052	4.6887	0.2277	0.1648	0.1482	2.1145	0.1358	0.4361	0.0035	1.552266	2.738291	0.083582	0.0257184	1.43E-16	DT-15c	0.0000585	2.91E-06	0.00326	0.85236	0.03509	4.86783	4.92319	0.15120	0.02218
882-02G	R12 OS03	Whole rock	1.3	97.5470	0.4052	3.5623	0.2285	−0.0675	0.1458	1.7662	0.1361	0.3189	0.0026	1.706925	2.609439	0.0765559	0.02706	1.09E-16	DT-15c	0.0000585	2.91E-06	0.00326	0.92628	0.03651	6.43041	6.47010	0.11437	0.02897
882-02H	R12 OS03	Whole rock	1.5	81.0361	0.4019	2.3027	0.2272	0.1086	0.1463	1.2947	0.1356	0.2699	0.0027	1.936204	0.7785817	0.0293587	0.0418571	7.02E-17	DT-15c	0.0000585	2.91E-06	0.00332	1.11432	0.02840	9.88445	9.92223	0.09006	0.02233
882-02I	R12 OS03	Whole rock	1.7	58.4496	0.3949	1.7006	0.2267	0.2541	0.1469	0.9442	0.1350	0.1895	0.0024	1.91237	3.429692	0.1262988	0.0543298	5.18E-17	DT-15c	0.0000585	2.91E-06	0.00323	1.44106	0.02908	13.35514	13.39853	0.08391	0.02372
882-02J	R12 OS03	Whole rock	1.9	40.9107	0.3946	1.0119	0.2287	0.0030	0.1478	0.8543	0.1377	0.1343	0.0023	2.908663	2.235736	0.096886	0.0869057	3.08E-17	DT-15c	0.0000585	2.91E-06	0.00327	1.97409	0.02471	22.64778	22.69254	0.06623	0.02081
882-02K	R12 OS03	Whole rock	2.5	90.8228	0.4019	2.8557	0.2310	0.1398	0.1452	3.5366	0.1374	0.3035	0.0029	4.267627	0.7309502	0.0249283	0.0356171	8.71E-17	DT-15c	0.0000585	2.91E-06	0.00332	1.04895	0.03140	8.11379	8.15727	0.10571	0.02301
882-02L	R12 OS03	Whole rock	3.0	209.7410	0.4080	5.8725	0.2282	0.1145	0.1460	10.5188	0.1356	0.6919	0.0043	6.173904	2.146035	0.0822423	0.0246646	1.79E-16	DT-15c	0.0000585	2.91E-06	0.00328	0.65075	0.02795	3.89875	3.94307	0.15028	0.01492
882-02M	R12 OS03	Whole rock	4.0	207.9860	0.4111	5.9189	0.2414	0.2402	0.1466	12.9865	0.1370	0.7017	0.0038	7.564285	0.0650099	0.0024524	0.022149	1.80E-16	DT-15c	0.0000585	2.91E-06	0.00335	0.58728	0.02839	4.09350	4.12592	0.12621	0.01625
882-02N	R12 OS03	Whole rock	5.0	51.1968	0.3946	1.4274	0.2285	−0.2209	0.1482	3.8559	0.1361	0.1693	0.0024	9.315146	2.228134	0.0858401	0.0630536	4.35E-17	DT-15c	0.0000585	2.91E-06	0.00327	1.62499	0.02780	16.07387	16.11886	0.07813	0.02274
882-02O	R12 OS03	Whole rock	6.0	88.5523	0.4026	2.3478	0.2390	0.0595	0.1458	7.5930	0.1370	0.2933	0.0028	11.15513	2.187189	0.0886661	0.0432335	7.16E-17	DT-15c	0.0000585	2.91E-06	0.00328	1.06151	0.02642	10.22829	10.26303	0.08445	0.01904
Plateau age = 0.05 ± 0.02 Ma, steps A–O, MSWD = 1.0, 100% of ^{39}Ar. Integrated age = 0.06 ± 0.03 Ma.																												
866-02A	R12 OS04	Whole rock	0.1	−0.2946	0.3985	0.1267	0.2293	0.0669	0.1455	−0.0189	0.1370	−0.0017	0.0015	−0.5066588	−70.03711	0.1765784	0.6053953	3.86E-18	DT-15a	0.0000593	2.73E-06	0.00570	162.34530	−0.43012	−225.95050	−202.02490	0.24564	0.49888
866-02B	R12 OS04	Whole rock	0.3	−0.4315	0.3985	−0.3751	0.2414	0.1357	0.1455	0.1999	0.1350	−0.0014	0.0015	−1.808358	−4.101151	−0.0051118	0.1740613	−1.14E-17	DT-15a	0.0000593	2.73E-06	0.00349	136.55670	0.87007	112.54220	119.37950	0.62059	0.55505
866-02C	R12 OS04	Whole rock	0.5	−0.6462	0.3983	−0.1068	0.2293	0.0249	0.1469	0.1007	0.1361	−0.0007	0.0015	−3.200282	65.17983	0.4271061	1.101338	−3.26E-18	DT-15a	0.0000593	2.73E-06	0.00117	210.54270	0.16548	223.13910	294.12330	0.65443	0.08088
866-02D	R12 OS04	Whole rock	0.7	0.6176	0.3936	0.9875	0.2456	0.0229	0.1463	0.4446	0.1356	0.0079	0.0016	1.52875	−273.3736	−0.185483	0.083154	3.01E-17	DT-15a	0.0000593	2.73E-06	0.01251	67.19597	1.59844	68.41560	32.76143	0.20622	0.88341
866-02E	R12 OS04	Whole rock	0.9	26.3600	0.3992	2.1260	0.2502	0.2378	0.1472	2.4544	0.1370	0.0750	0.0021	3.921166	16.20966	0.2181896	0.0454644	6.48E-17	DT-15a	0.0000593	2.73E-06	0.00281	3.17464	0.08056	11.88202	12.11066	0.20249	0.06079
866-02F	R12 OS04	Whole rock	1.1	42.7790	0.3957	2.7894	0.2285	0.1027	0.1469	5.2919	0.1364	0.0749	0.0020	6.445504	49.29623	0.8213333	0.07292	8.50E-17	DT-15a	0.0000593	2.73E-06	0.00170	2.89401	0.06508	8.26013	8.65385	0.30024	0.03579
866-02G	R12 OS04	Whole rock	1.3	34.4750	0.3935	2.6468	0.2279	−0.0808	0.1469	4.2252	0.1367	0.0497	0.0019	5.424875	58.50023	0.8275052	0.076614	8.07E-17	DT-15a	0.0000593	2.73E-06	0.00139	4.02880	0.07665	8.70250	9.45264	0.39199	0.03715
866-02H	R12 OS04	Whole rock	1.5	29.1529	0.3977	2.9845	0.2414	−0.0143	0.1455	3.0736	0.1361	0.0367	0.0018	3.500699	63.77857	0.676168	0.0598524	9.10E-17	DT-15a	0.0000593	2.73E-06	0.00121	5.23101	0.10227	8.21186	9.54285	0.51084	0.04333
866-02I	R12 OS04	Whole rock	1.7	23.5637	0.3951	2.1264	0.2310	0.0691	0.1466	2.3108	0.1356	0.0289	0.0017	3.694786	64.65821	0.77768	0.0906409	6.48E-17	DT-15a	0.0000593	2.73E-06	0.00118	6.25070	0.09015	11.00672	12.43308	0.46655	0.04086
866-02J	R12 OS04	Whole rock	1.9	24.6632	0.3951	1.9935	0.2274	−0.0204	0.1469	2.0992	0.1358	0.0357	0.0016	3.581169	57.88866	0.7773099	0.0951822	6.08E-17	DT-15a	0.0000593	2.73E-06	0.00141	5.00133	0.08075	11.53365	12.36501	0.36297	0.04448
866-02K	R12 OS04	Whole rock	2.5	35.0803	0.3943	2.4561	0.2293	0.1668	0.1463	2.2040	0.1350	0.0620	0.0019	3.052636	48.00169	0.7440035	0.0760077	7.49E-17	DT-15a	0.0000593	2.73E-06	0.00174	3.33790	0.06995	9.41229	9.85900	0.30016	0.04021
866-02L	R12 OS04	Whole rock	3.0	17.8728	0.3933	1.1112	0.2414	−0.1334	0.1482	1.0632	0.1367	0.0356	0.0017	3.255754	41.27701	0.7205034	0.1686744	3.39E-17	DT-15a	0.0000593	2.73E-06	0.00197	5.29124	0.06212	21.85841	22.27275	0.19646	0.04187
866-02M	R12 OS04	Whole rock	4.0	41.6482	0.4016	2.2147	0.2406	0.1617	0.1452	2.3049	0.1361	0.0939	0.0020	3.542149	33.35292	0.6807369	0.0819754	6.75E-17	DT-15a	0.0000593	2.73E-06	0.00223	2.35420	0.05312	10.91830	11.08542	0.17673	0.03618
866-02N	R12 OS04	Whole rock	5.0	34.8882	0.3935	1.0721	0.2332	−0.1648	0.1458	2.0525	0.1361	0.0902	0.0019	6.517772	23.57856	0.8336213	0.1949683	3.27E-17	DT-15a	0.0000593	2.73E-06	0.00256	2.43421	0.03067	21.83405	21.91113	0.08725	0.02393
866-02O	R12 OS04	Whole rock	6.0	19.2220	0.3941	0.5807	0.2236	−0.0715	0.1460	1.0127	0.1353	0.0531	0.0019	5.938656	18.14481	0.652436	0.2832723	1.77E-17	DT-15a	0.0000593	2.73E-06	0.00274	4.17858	0.03016	38.63094	38.74754	0.08187	0.02605
Plateau age = 0.75 ± 0.06 Ma, steps F–O, MSWD = 0.5, 87.9% of ^{39}Ar. Integrated age = 0.68 ± 0.08 Ma.																												
869-02A	R12 OS05	Whole rock	0.1	−0.2083	0.3996	−0.0689	0.2298	−0.0799	0.1469	0.1687	0.1356	−0.0007	0.0015	−8.351647	−9.571015	−0.0316088	0.9594585	−2.10E-18	DT-15b	0.0000599	1.02E-06	0.00367	274.96580	0.33199	383.81590	386.39860	0.36523	0.34869
869-02B	R12 OS05	Whole rock	0.3	−0.0303	0.3937	0.1361	0.2456	0.0768	0.1485	0.1190	0.1370	−0.0006	0.0015	2.984234	−540.4586	0.1320194	0.5388276	4.15E-18	DT-15b	0.0000599	1.02E-06	0.02145	1320.10500	−4.48831	−1311.90800	−294.73110	0.13935	0.97494
869-02C	R12 OS05	Whole rock	0.5	−0.1549	0.3992	0.2166	0.2293	0.0508	0.1469	0.1384	0.1367	0.0007	0.0015	2.181793	213.9376	−0.1678625	0.3537798	6.60E-18	DT-15b	0.0000599	1.02E-06	−0.00382	−363.70530	−1.39742	−278.61460	277.66220	0.65232	0.65528
869-02D	R12 OS05	Whole rock	0.7	0.6190	0.3979	0.2290	0.2290	0.0572	0.1452	0.1430	0.1358	0.0007	0.0015	2.133006	68.745	0.2038362	0.3549853	6.98E-18	DT-15b	0.0000599	1.02E-06	0.00105	245.16360	0.36975	118.94370	256.86850	0.88877	0.14172
869-02E	R12 OS05	Whole rock	0.9	23.0189	0.3957	2.4857	0.2502	0.3422	0.1482	4.0281	0.1358	0.0602	0.0019	5.535125	24.17407	0.245844	0.0395207	7.58E-17	DT-15b	0.0000599	1.02E-06	0.00254	3.70685	0.10780	10.23096	10.60638	0.27431	0.07792
869-02F	R12 OS05	Whole rock	1.1	40.8275	0.4026	4.0461	0.2414	−0.1009	0.1466	7.4636	0.1358	0.0469	0.0018	6.302101	67.98202	0.7534058	0.0485558	1.23E-16	DT-15b	0.0000599	1.02E-06	0.00107	4.19999	0.09891	6.05947	7.23922	0.54815	0.03821
869-02G	R12 OS05	Whole rock	1.3	42.2212	0.4021	4.1013	0.2301	0.1044	0.1458	3.5467	0.1377	0.0399	0.0018	2.955068	72.86263	0.8228698	0.049544	1.25E-16	DT-15b	0.0000599	1.02E-06	0.00091	4.75171	0.09706	5.69706	7.29486	0.62517	0.03351
869-02H	R12 OS05	Whole rock	1.5	33.3455	0.3936	3.0064	0.2394	0.0495	0.1482	2.5732	0.1356	0.0354	0.0017	2.925451	69.28285	0.842996	0.0710758	9.16E-17	DT-15b	0.0000599	1.02E-06	0.00103	5.02280	0.09009	8.05733	9.34628	0.50770	0.03442
869-02I	R12 OS05	Whole rock	1.7	22.1001	0.4007	1.9432	0.2274	0.0642	0.1478	1.7849	0.1374	0.0272	0.0017	3.140265	64.32684	0.8026274	0.1009449	5.92E-17	DT-15b	0.0000599	1.02E-06	0.00119	6.75794	0.08785	11.85508	13.40222	0.46792	0.04103
869-02J	R12 OS05	Whole rock	1.9	26.2850	0.3952	1.4617	0.2296	−0.0557	0.1475	2.0462	0.1367	0.0462	0.0018	4.786944	48.49703	0.9572833	0.1585924	4.46E-17	DT-15b	0.0000599	1.02E-06	0.00173	4.21903	0.05553	15.80230	16.21657	0.22712	0.03391
869-02K	R12 OS05	Whole rock	2.5	38.8438	0.3941	1.0773	0.2290	−0.0616	0.1466	2.7869	0.1358	0.0982	0.0020	8.848017	25.43058	1.007848	0.2268625	3.28E-17	DT-15b	0.0000599	1.02E-06	0.00250	2.29561	0.02766	21.34433	21.41920	0.08623	0.02101
869-02L	R12 OS05	Whole rock	3.0	34.4600	0.3937	0.6072	0.2262	0.1995	0.1460	2.2921	0.1348	0.1006	0.0021	12.91457	13.71775	0.8569099	0.346989	1.85E-17	DT-15b	0.0000599	1.02E-06	0.00289	2.37199	0.01755	37.43442	37.47447	0.04861	0.01470
869-02M	R12 OS05	Whole rock	4.0	44.1550	0.3996	0.4985	0.2293	0.0781	0.1463	4.4776	0.1370	0.1377	0.0024	30.73525	8.186352	0.8029462	0.4148899	1.52E-17	DT-15b	0.0000599	1.02E-06	0.00308	1.97764	0.01118	46.48094	46.50524	0.03362	0.00891
869-02N	R12 OS05	Whole rock	5.0	19.6527	0.3940	0.2981	0.2307	−0.0726	0.1452	2.7736	0.1358	0.0609	0.0019	31.84155	9.319985	0.6806063	0.5891369	9.09E-18	DT-15b	0.0000599	1.02E-06	0.00304	3.69606	0.01501	78.25239	78.28796	0.03332	0.01390
869-02O	R12 OS05	Whole rock	6.0	29.8533	0.3923	0.3946	0.2243	0.0130	0.1463	4.7840	0.1374	0.0939	0.0019	41.50508	8.12366	0.6831044	0.4398811	1.20E-17	DT-15b	0.0000599	1.02E-06	0.00308	2.47553	0.01304	57.66066	57.68363	0.03083	0.01210
Plateau age = 0.81 ± 0.06 Ma, steps F–O, MSWD = 0.4, 85.3% of ^{39}Ar. Integrated age = 0.74 ± 0.07 Ma.																												

(*continued*)

TABLE 2. ANALYTICAL RESULTS OF CO_2-LASER INCREMENTAL HEATING $^{40}Ar/^{39}Ar$ EXPERIMENT (*continued*)

Run_ID	Sample	Material	CO_2 laser power (W)	^{40}Ar (fA)	^{40}Ar (fA) σ	^{39}Ar (fA)	^{39}Ar (fA) σ	^{38}Ar (fA)	^{38}Ar (fA) σ	^{37}Ar (fA)	^{37}Ar (fA) σ	^{36}Ar (fA)	^{36}Ar (fA) σ	Ca/K	%^{40}Ar rad	Age (Ma)	Age (Ma)	^{39}Ar moles	Irradiation	*J*	*J* σ	Isochron $^{36}Ar/^{40}Ar$	Percent initial $^{36}Ar/^{40}Ar$ error	Isochron $^{39}Ar/^{40}Ar$	Percent initial $^{39}Ar/^{40}Ar$ error	Percent initial $^{39}Ar/^{36}Ar$ error	Correlation coefficient $^{40}Ar/^{39}Ar$	Correlation coefficient $^{36}Ar/^{39}Ar$
870-02A	R12 OS06	Whole rock	0.1	−0.3483	0.3994	0.1853	0.2293	−0.1589	0.1466	−0.0496	0.1367	−0.0017	0.0015	−0.9160066	−41.00867	0.0844772	0.376302	5.65E-18	DT-15b	0.0000599	1.02E-06	0.00472	148.40180	−0.53223	−168.67550	−155.50770	0.38462	0.52523
870-02B	R12 OS06	Whole rock	0.3	−0.7100	0.3987	−0.4520	0.2456	0.0317	0.1452	−0.0562	0.1370	−0.0013	0.0015	0.4255732	45.01975	0.0775239	0.1525123	−1.38E-17	DT-15b	0.0000599	1.02E-06	0.00184	129.18530	0.63670	78.15335	128.40230	0.81591	0.31239
870-02C	R12 OS06	Whole rock	0.5	−0.7450	0.3996	−0.4490	0.2456	−0.1370	0.1455	0.0025	0.1361	−0.0006	0.0015	−0.0187938	77.42605	0.140805	0.1675276	−1.37E-17	DT-15b	0.0000599	1.02E-06	0.00076	278.83470	0.60287	76.61114	279.03450	0.96228	0.13467
870-02D	R12 OS06	Whole rock	0.7	0.1622	0.3983	0.0331	0.2282	0.0558	0.1478	−0.0244	0.1358	0.0009	0.0015	−2.53116	−68.4014	−0.3673487	3.223095	1.01E-18	DT-15b	0.0000599	1.02E-06	0.00564	296.09600	0.20418	731.63060	708.73890	0.13040	0.27838
870-02E	R12 OS06	Whole rock	0.9	24.4374	0.3947	2.0992	0.2456	0.2586	0.1478	4.2758	0.1356	0.0543	0.0019	6.983187	35.88648	0.4589706	0.0645156	6.40E-17	DT-15b	0.0000599	1.02E-06	0.00215	3.88171	0.08572	11.84016	12.24862	0.26202	0.05677
870-02F	R12 OS06	Whole rock	1.1	35.2019	0.3943	3.8978	0.2414	−0.0448	0.1475	6.2062	0.1377	0.0337	0.0017	5.460002	73.61395	0.7299737	0.0488328	1.19E-16	DT-15b	0.0000599	1.02E-06	0.00088	5.65869	0.11055	6.30473	8.32181	0.65330	0.03517
870-02G	R12 OS06	Whole rock	1.3	39.2775	0.3944	4.2021	0.2298	0.0371	0.1450	3.7802	0.1380	0.0311	0.0017	3.085635	77.58152	0.7955752	0.0465839	1.28E-16	DT-15b	0.0000599	1.02E-06	0.00075	5.71148	0.10689	5.56690	7.84772	0.70524	0.03172
870-02H	R12 OS06	Whole rock	1.5	26.1331	0.3933	2.8373	0.2285	0.1280	0.1469	2.0943	0.1364	0.0194	0.0016	2.532437	78.81235	0.7962509	0.0686183	8.65E-17	DT-15b	0.0000599	1.02E-06	0.00071	9.00469	0.10850	8.19835	11.98954	0.73001	0.03068
870-02I	R12 OS06	Whole rock	1.7	14.8068	0.3941	1.4151	0.2298	0.0460	0.1482	1.7618	0.1364	0.0117	0.0016	4.272206	77.92251	0.8948339	0.1531641	4.31E-17	DT-15b	0.0000599	1.02E-06	0.00074	14.72951	0.09545	16.48233	21.78055	0.65414	0.02919
870-02J	R12 OS06	Whole rock	1.9	9.8128	0.3985	0.6980	0.2367	0.1069	0.1463	1.4624	0.1374	0.0101	0.0016	7.191058	71.17022	1.099097	0.3864072	2.13E-17	DT-15b	0.0000599	1.02E-06	0.00097	17.62606	0.07098	34.23939	38.07719	0.43830	0.02733
870-02K	R12 OS06	Whole rock	2.5	25.3349	0.3947	1.2685	0.2414	0.0919	0.1472	3.3824	0.1356	0.0538	0.0019	9.15453	38.23758	0.8395714	0.1707078	3.87E-17	DT-15b	0.0000599	1.02E-06	0.00207	3.86230	0.04992	19.15244	19.41294	0.16657	0.03282
870-02L	R12 OS06	Whole rock	3.0	23.8623	0.3943	0.4946	0.2296	0.1568	0.1472	4.5754	0.1358	0.0663	0.0019	31.76357	19.41293	1.037365	0.5097544	1.51E-17	DT-15b	0.0000599	1.02E-06	0.00270	3.31969	0.02051	46.93918	46.99804	0.05313	0.01752
870-02M	R12 OS06	Whole rock	4.0	22.7759	0.3944	0.3637	0.2269	0.0556	0.1472	6.0147	0.1370	0.0679	0.0019	56.80058	14.37369	1.005605	0.6742758	1.11E-17	DT-15b	0.0000599	1.02E-06	0.00287	3.41346	0.01567	63.62970	63.67379	0.03981	0.01381
870-02N	R12 OS06	Whole rock	5.0	8.4471	0.3996	0.1931	0.2282	−0.0805	0.1472	3.2315	0.1364	0.0226	0.0017	57.48512	24.96543	1.220142	1.515669	5.89E-18	DT-15b	0.0000599	1.02E-06	0.00251	9.21585	0.02243	120.57570	120.74130	0.05622	0.02014
870-02O	R12 OS06	Whole rock	6.0	35.4605	0.3939	0.2117	0.2260	−0.0721	0.1472	9.1886	0.1367	0.1058	0.0021	149.1444	14.20555	2.743839	3.108219	6.45E-18	DT-15b	0.0000599	1.02E-06	0.00287	2.38050	0.00567	112.38110	112.39510	0.01657	0.00461
Plateau age = 0.78 ± 0.06 Ma, steps F–O, MSWD = 0.4, 91.7% of ^{39}Ar. Integrated age = 0.83 ± 0.12 Ma.																												
875-02A	R12 HA01	Whole rock	0.1	−0.1587	0.3987	0.2218	0.2301	0.0003	0.1466	0.0762	0.1374	−0.0010	0.0015	1.220092	−103.6103	0.0812806	0.3104334	6.76E-18	DT-15b	0.0000599	1.02E-06	0.00682	287.89260	−1.39759	−271.84100	−174.72980	0.39275	0.80662
875-02B	R12 HA01	Whole rock	0.3	−0.5097	0.3931	−0.1296	0.2293	−0.1664	0.1463	0.0170	0.1361	0.0003	0.0015	−0.4667423	115.4822	0.4975299	1.013855	−3.95E-18	DT-15b	0.0000599	1.02E-06	−0.00052	−573.63330	0.25446	192.90660	−595.31800	0.94620	0.05374
875-02C	R12 HA01	Whole rock	0.5	−0.6066	0.3977	−0.4878	0.2456	0.0939	0.1488	−0.0302	0.1353	−0.0008	0.0015	0.2201904	60.95666	0.0830982	0.1409042	−1.49E-17	DT-15b	0.0000599	1.02E-06	0.00131	199.99310	0.80426	82.67579	195.52950	0.91286	0.26000
875-02D	R12 HA01	Whole rock	0.7	0.2114	0.3981	0.0344	0.2307	0.1452	0.1475	0.1240	0.1374	0.0010	0.0016	12.81718	−26.67485	−0.1806152	2.314155	1.05E-18	DT-15b	0.0000599	1.02E-06	0.00424	256.91800	0.16194	699.94670	696.39470	0.17069	0.19723
875-02E	R12 HA01	Whole rock	0.9	48.1310	0.4111	0.8346	0.2264	0.2853	0.1469	0.9499	0.1377	0.1163	0.0022	4.044133	28.15078	1.78111	0.4944466	2.54E-17	DT-15b	0.0000599	1.02E-06	0.00241	2.10181	0.01732	27.18222	27.23640	0.06442	0.01277
875-02F	R12 HA01	Whole rock	1.1	54.1874	0.4012	1.1316	0.2382	0.0075	0.1469	1.9992	0.1380	0.0668	0.0019	6.278969	63.70293	3.347966	0.708959	3.45E-17	DT-15b	0.0000599	1.02E-06	0.00122	3.00894	0.02084	21.11074	21.29804	0.13272	0.00863
875-02G	R12 HA01	Whole rock	1.3	55.3989	0.4026	1.1175	0.2277	−0.0557	0.1460	1.6127	0.1380	0.0750	0.0019	5.13032	59.98194	3.262388	0.6687989	3.41E-17	DT-15b	0.0000599	1.02E-06	0.00134	2.68972	0.02014	20.42249	20.57290	0.12119	0.00962
875-02H	R12 HA01	Whole rock	1.5	52.6430	0.3996	1.0584	0.2398	0.1153	0.1463	1.3670	0.1364	0.0943	0.0021	4.592281	46.84745	2.556279	0.5845921	3.23E-17	DT-15b	0.0000599	1.02E-06	0.00178	2.33408	0.02008	22.70204	22.79621	0.09156	0.01087
875-02I	R12 HA01	Whole rock	1.7	45.7695	0.4012	0.5009	0.2279	0.0353	0.1478	1.0106	0.1358	0.0793	0.0021	7.175449	48.56841	4.869953	2.224264	1.53E-17	DT-15b	0.0000599	1.02E-06	0.00172	2.76199	0.01092	45.62226	45.68869	0.05436	0.00610
875-02J	R12 HA01	Whole rock	1.9	36.6241	0.3935	0.7180	0.2258	0.1129	0.1460	1.1815	0.1345	0.0678	0.0019	5.85401	45.13608	2.527057	0.8026897	2.19E-17	DT-15b	0.0000599	1.02E-06	0.00184	3.05043	0.01957	31.52388	31.63434	0.08447	0.01200
875-02K	R12 HA01	Whole rock	2.5	322.5240	0.4111	3.5757	0.2414	0.2689	0.1463	5.6441	0.1374	0.7620	0.0042	5.616303	29.68836	2.938603	0.2026106	1.09E-16	DT-15b	0.0000599	1.02E-06	0.00236	0.56223	0.01107	6.76486	6.78576	0.07860	0.00427
875-02L	R12 HA01	Whole rock	3.0	536.1970	0.4215	4.7303	0.2293	0.2795	0.1458	8.4057	0.1350	1.4300	0.0057	6.324187	20.57851	2.560652	0.1308451	1.44E-16	DT-15b	0.0000599	1.02E-06	0.00266	0.40950	0.00881	4.85804	4.87398	0.08092	0.00311
875-02M	R12 HA01	Whole rock	4.0	584.6410	0.4338	5.0924	0.2277	0.2089	0.1463	14.4876	0.1367	1.5618	0.0064	10.12728	20.56883	2.595543	0.1237496	1.55E-16	DT-15b	0.0000599	1.02E-06	0.00266	0.41668	0.00868	4.48673	4.50480	0.08956	0.00295
875-02N	R12 HA01	Whole rock	5.0	269.5950	0.4144	2.4561	0.2414	0.2303	0.1488	10.6967	0.1370	0.7205	0.0041	15.50713	20.72683	2.5053	0.2541053	7.49E-17	DT-15b	0.0000599	1.02E-06	0.00266	0.59587	0.00906	9.88110	9.89663	0.05620	0.00401
875-02O	R12 HA01	Whole rock	6.0	372.2770	0.4215	2.8757	0.2277	0.0704	0.1472	17.5108	0.1370	1.0206	0.0048	21.68639	18.7669	2.680745	0.2213133	8.77E-17	DT-15b	0.0000599	1.02E-06	0.00272	0.49121	0.00767	7.97612	7.98961	0.05821	0.00327
Plateau age = 2.63 ± 0.14 Ma, steps D–O, MSWD = 0.9, 101.7% of ^{39}Ar. Integrated age = 2.8 ± 0.2 Ma.																												
884-02A	R12 HA02	Whole rock	0.1	−0.2793	0.3996	0.1555	0.2320	0.0441	0.1478	0.1331	0.1353	−0.0009	0.0015	3.084749	−1.902024	0.0036624	0.4158974	4.74E-18	DT-15c	0.0000585	2.91E-06	0.00341	213.71910	−0.55621	−206.81430	−217.98810	0.54111	0.46308
884-02B	R12 HA02	Whole rock	0.3	−0.1877	0.3971	0.0177	0.2287	0.0426	0.1463	0.2167	0.1361	−0.0017	0.0015	44.17557	−187.2427	2.158904	28.56404	5.39E-19	DT-15c	0.0000585	2.91E-06	0.00962	227.07240	−0.09283	−1329.87600	−1315.53400	0.02274	0.14825
884-02C	R12 HA02	Whole rock	0.5	−0.0231	0.3936	0.3854	0.2272	0.2428	0.1463	0.0327	0.1374	−0.0021	0.0015	0.3059837	−2631.678	0.168925	0.1950863	1.17E-17	DT-15c	0.0000585	2.91E-06	0.09150	1705.37400	-16.68447	−1704.85000	−93.48384	0.03301	0.99850
884-02D	R12 HA02	Whole rock	0.7	0.4351	0.3998	−0.1847	0.2290	0.1402	0.1452	−0.0293	0.1361	0.0015	0.0015	0.57129	−2.833982	0.0071505	0.3515114	−5.63E-18	DT-15c	0.0000585	2.91E-06	0.00344	137.11800	−0.42448	−154.35140	−160.44500	0.47085	0.39895
884-02E	R12 HA02	Whole rock	0.9	36.0552	0.3947	4.0931	0.2502	0.2252	0.1485	4.0198	0.1367	0.1255	0.0024	3.542474	−2.409953	−0.0227585	0.0213661	1.25E-16	DT-15c	0.0000585	2.91E-06	0.00343	2.21700	0.11341	6.21778	6.41687	0.26123	0.08695
884-02F	R12 HA02	Whole rock	1.1	41.2442	0.3947	5.8970	0.2287	0.0882	0.1472	5.4029	0.1377	0.1319	0.0022	3.305571	6.221343	0.0466433	0.0138352	1.80E-16	DT-15c	0.0000585	2.91E-06	0.00314	1.91806	0.14285	3.99926	4.22370	0.34103	0.11942
884-02G	R12 HA02	Whole rock	1.3	41.8315	0.4026	5.0788	0.2296	0.0677	0.1469	2.9420	0.1361	0.1326	0.0022	2.090433	6.3217	0.055792	0.0162036	1.55E-16	DT-15c	0.0000585	2.91E-06	0.00314	1.90222	0.12135	4.62447	4.81143	0.29413	0.10531
884-02H	R12 HA02	Whole rock	1.5	40.8670	0.4579	4.6183	0.2307	0.0787	0.1458	2.1323	0.1364	0.1323	0.0022	1.666508	4.06168	0.0385061	0.0184126	1.41E-16	DT-15c	0.0000585	2.91E-06	0.00321	1.98613	0.11297	5.12280	5.26069	0.25736	0.12341
884-02I	R12 HA02	Whole rock	1.7	33.0439	0.3943	4.0171	0.2277	0.4059	0.1466	2.3299	0.1367	0.1041	0.0021	2.093991	6.867176	0.0605278	0.0198616	1.22E-16	DT-15c	0.0000585	2.91E-06	0.00312	2.33694	0.12151	5.79580	6.01685	0.28713	0.10512
884-02J	R12 HA02	Whole rock	1.9	25.8905	0.4026	2.6865	0.2287	0.0553	0.1482	1.9266	0.1361	0.0810	0.0020	2.589681	7.635062	0.0788546	0.0294434	8.19E-17	DT-15c	0.0000585	2.91E-06	0.00309	2.93489	0.10370	8.66206	8.87714	0.23778	0.09512
884-02K	R12 HA02	Whole rock	2.5	74.8168	0.4026	4.3258	0.2293	0.1141	0.1472	4.9690	0.1364	0.2460	0.0027	4.149148	2.694391	0.0499684	0.0223333	1.32E-16	DT-15c	0.0000585	2.91E-06	0.00326	1.22209	0.05775	5.33498	5.41991	0.18176	0.04442
884-02L	R12 HA02	Whole rock	3.0	45.7107	0.3935	1.7247	0.2282	−0.0603	0.1463	3.2285	0.1370	0.1513	0.0022	6.763171	2.108024	0.059961	0.0476811	5.26E-17	DT-15c	0.0000585	2.91E-06	0.00328	1.67875	0.03765	13.28927	13.33930	0.09276	0.03321
884-02M	R12 HA02	Whole rock	4.0	36.3744	0.4007	0.5032	0.2258	−0.0080	0.1463	3.4715	0.1361	0.1199	0.0023	24.9311	2.826391	0.2206076	0.1978149	1.53E-17	DT-15c	0.0000585	2.91E-06	0.00325	2.23571	0.01372	45.25781	45.28601	0.03738	0.01199
884-02N	R12 HA02	Whole rock	5.0	32.9729	0.3931	0.7517	0.2255	−0.0753	0.1458	3.5161	0.1356	0.1107	0.0021	16.90843	1.153568	0.0544937	0.1063286	2.29E-17	DT-15c	0.0000585	2.91E-06	0.00331	2.24213	0.02267	30.20036	30.23631	0.05319	0.02099
884-02O	R12 HA02	Whole rock	6.0	44.7776	0.3961	0.8773	0.2262	−0.0224	0.1472	5.9034	0.1387	0.1355	0.0022	24.32765	11.41715	0.6289894	0.1892557	2.67E-17	DT-15c	0.0000585	2.91E-06	0.00297	1.89749	0.01944	26.01176	26.05069	0.05701	0.01585
884-02P	R12 HA02	Whole rock	7.0	41.8508	0.3994	0.9284	0.2253	−0.1642	0.1463	7.0506	0.1356	0.1370	0.0022	27.46332	4.471162	0.217816	0.10306	2.83E-17	DT-15c	0.0000585	2.91E-06	0.00320	1.87100	0.02198	24.51458	24.54864	0.05639	0.01985
Plateau age = 0.052 ± 0.017 Ma, steps F–N, MSWD = 0.3, 82.5% of ^{39}Ar. Integrated age = 0.07 ± 0.03 Ma.																												
887-02A	R12 HA03	Whole rock	0.1	−0.5039	0.3931	−0.1698	0.2285	−0.0770	0.1488	−0.0102	0.1370	−0.0011	0.0015	0.2333938	34.5698	0.1098635	0.405164	−5.18E-18	DT-15c	0.0000585	2.91E-06	0.00219	157.42090	0.33700	155.54340	191.83160	0.61907	0.24850
887-02B	R12 HA03	Whole rock	0.3	−0.3650	0.3943	0.2017	0.2456	0.1565	0.1482	−0.0680	0.1374	−0.0023	0.0015	−1.303923	−87.99503	0.1704425	0.3781406	6.15E-18	DT-15c	0.0000585	2.91E-06	0.00630	126.10870	−0.55291	−162.76500	−138.05840	0.24321	0.56851
887-02C	R12 HA03	Whole rock	0.5	−0.4786	0.3992	0.1902	0.2301	0.0000	0.1469	−0.0140	0.1348	−0.0003	0.0015	−0.2846733	78.96422	−0.2128032	0.4250293	5.80E-18	DT-15c	0.0000585	2.91E-06	0.00070	453.33780	−0.39744	−146.97310	−461.76100	0.94857	0.10440
887-02D	R12 HA03	Whole rock	0.7	−0.6598	0.3994	−0.0013	0.2296	0.1584	0.1478	0.2092	0.1370	−0.0025	0.0015	−627.0653	−19.65094	−8.900016	1310.441	−3.94E-20	DT-15c	0.0000585	2.91E-06	0.00401	83.41140	0.00237	14,681.06000	14,681.03000	0.00269	0.00299
887-02E	R12 HA03	Whole rock	0.9	33.9484	0.3941	0.5699	0.2239	0.0071	0.1455	0.4960	0.1356	0.1155	0.0021	3.369706	−1.340934	−0.0856354	0.1421552	1.74E-17	DT-15c	0.0000585	2.91E-06	0.00339	2.14222	0.01677	39.35625	39.38007	0.03842	0.01599
887-02F	R12 HA03	Whole rock	1.1	37.8065	0.3949	1.6116	0.2410	0.0676	0.1463	2.4058	0.1358	0.1206	0.0023	5.780676	5.65824	0.1423981	0.0569404	4.91E-17	DT-15c	0.0000585	2.91E-06	0.00316	2.19296	0.04256	15.01851	15.10550	0.11224	0.03313
887-02G	R12 HA03	Whole rock	1.3	34.7580	0.3937	5.1828	0.2272	0.0516	0.1466	5.3656	0.1364	0.0790	0.0019	4.009806	34.36365	0.2470763	0.0180337	1.58E-16	DT-15c	0.0000585	2.91E-06	0.00220	2.76098	0.14895	4.53288	5.05973	0.45380	0.10253
887-02H	R12 HA03	Whole rock	1.5	27.2288	0.3944	6.5583	0.2394	0.0825	0.1463	5.4486	0.1364	0.0467	0.0018	3.218624	51.69476	0.2300461	0.013725	2.00E-16	DT-15c	0.0000585	2.91E-06	0.00162	4.30886	0.24066	3.93081	5.46043	0.69986	0.12390
887-02I	R12 HA03	Whole rock	1.7	26.9394	0.3947	7.1887	0.2287	0.1846	0.1455	4.9784	0.1364	0.0387	0.0017	2.683611	59.73714	0.2399034	0.0122689	2.19E-16	DT-15c	0.0000585	2.91E-06	0.00135	4.91267	0.26667	3.50563	5.66790	0.78958	0.12467
887-02J	R12 HA03	Whole rock	1.9	25.2613	0.3949	7.0719	0.2290	0.0810	0.1466	4.1127	0.1361	0.0367	0.0017	2.25407	58.95336	0.2256406	0.0122587	2.16E-16	DT-15c	0.0000585	2.91E-06	0.00137	5.21053	0.27981	3.59802	5.93322	0.79909	0.13035
887-02K	R12 HA03	Whole rock	2.5	49.9146	0.3944	10.6898	0.2307	0.3519	0.1475	4.4183	0.1361	0.0914	0.0020	1.602376	46.60756	0.2331369	0.0087556	3.26E-16	DT-15c	0.0000585	2.91E-06	0.00179	2.37187	0.21410	2.29964	3.10869	0.67824	0.11449
887-02L	R12 HA03	Whole rock	3.0	53.8593	0.4014	6.6038	0.2282	0.2368	0.1463	2.6273	0.1356	0.1359	0.0022	1.542727	25.34451	0.2214307	0.0144887	2.01E-16	DT-15c	0.0000585	2.91E-06	0.00250	1.76506	0.12258	3.53672	3.80941	0.38071	0.08898
887-02M	R12 HA03	Whole rock	4.0	73.3447	0.4019	4.9591	0.2279	0.2468	0.1478	6.7378	0.1367	0.2115	0.0025	5.2698	15.20009	0.2411241	0.0214189	1.51E-16	DT-15c	0.0000585	2.91E-06	0.00284	1.31758	0.06751	4.63689	4.75764	0.22904	0.04914
887-02N	R12 HA03	Whole rock	5.0	29.2023	0.3983	1.6642	0.2269	−0.0306	0.1482	3.2867	0.1374	0.0825	0.0019	7.662025	17.24398	0.3248089	0.0632935	5.07E-17	DT-15c	0.0000585	2.91E-06	0.00277	2.74142	0.05685	13.73910	13.87619	0.14865	0.04940
887-02O	R12 HA03	Whole rock	6.0	14.8935	0.3931	0.6571	0.2247	−0.1672	0.1463	1.9845	0.1374	0.0444	0.0017	11.71952	12.92507	0.3149017	0.151142	2.00E-17	DT-15c	0.0000585	2.91E-06	0.00292	4.75057	0.04396	34.43263	34.55725	0.09504	0.04258
887-02P	R12 HA03	Whole rock	7.0	16.1232	0.3932	0.4348	0.2247	−0.0810	0.1460	3.1103	0.1367	0.0486	0.0018	27.76188	12.65723	0.5071739	0.3116414	1.33E-17	DT-15c	0.0000585	2.91E-06	0.00293	4.50754	0.02672	52.21673	52.29679	0.06096	0.02527
Plateau age = 0.23 ± 0.01 Ma, steps F–P, MSWD = 0.8, 98.5% of ^{39}Ar. Integrated age = 0.23 ± 0.08 Ma.																												

(*continued*)

TABLE 2. ANALYTICAL RESULTS OF CO_2-LASER INCREMENTAL HEATING $^{40}Ar/^{39}Ar$ EXPERIMENT (*continued*)

Run_ID	Sample	Material	CO_2 laser power (W)	^{40}Ar (fA)	^{40}Ar (fA) σ	^{39}Ar (fA)	^{39}Ar (fA) σ	^{38}Ar (fA)	^{38}Ar (fA) σ	^{37}Ar (fA)	^{37}Ar (fA) σ	^{36}Ar (fA)	^{36}Ar (fA) σ	Ca/K	%^{40}Ar rad	Age (Ma)	Age (Ma)	^{39}Ar moles	Irradiation	*J*	*J* σ	Isochron $^{36}Ar/^{40}Ar$	Percent initial $^{36}Ar/^{40}Ar$ error	Isochron $^{39}Ar/^{40}Ar$	Percent initial $^{39}Ar/^{40}Ar$ error	Percent initial $^{39}Ar/^{36}Ar$ error	Correlation coefficient $^{40}Ar/^{39}Ar$	Correlation coefficient $^{36}Ar/^{39}Ar$
Monitors for sample data																												
868-11	FCT-A	Sanidine	4.0	1576.3140	0.6742	5.8688	0.2293	0.0086	0.1482	−0.0381	0.1370	0.0106	0.0017	−0.0178978	99.79959	28.83768	1.117895	1.79E-16	DT-15a	0.0000593	2.73E-06	0.00001	16.23132	0.00372	3.90699	16.69453	0.97223	0.00003
868-12	FCT-A	Sanidine	4.0	7025.8150	1.3572	0.4618	0.2269	−0.0551	0.1478	0.2431	0.1361	0.0836	0.0024	1.451758	99.64501	1173.459	425.9179	1.41E-17	DT-15a	0.0000593	2.73E-06	0.00001	2.83814	0.00007	49.16704	49.24873	0.05763	0.00000
868-13	FCT-A	Sanidine	4.0	2304.9580	0.6420	8.5405	0.2299	0.2491	0.1458	0.1467	0.1374	0.0080	0.0017	0.0520501	99.89666	29.00335	0.7744993	2.60E-16	DT-15a	0.0000593	2.73E-06	0.00000	21.52900	0.00371	2.69150	21.69631	0.99228	0.00001
868-14	FCT-A	Sanidine	4.0	1558.5670	0.5308	6.0620	0.2298	0.1433	0.1475	0.0678	0.1367	0.0074	0.0017	0.0338919	99.85866	27.62962	1.039848	1.85E-16	DT-15a	0.0000593	2.73E-06	0.00000	22.44586	0.00389	3.79187	22.76348	0.98603	0.00001
868-15	FCT-A	Sanidine	4.0	2604.0340	0.7072	10.1073	0.2304	0.1755	0.1460	0.1742	0.1364	0.0104	0.0017	0.0522492	99.8818	27.69305	0.6266965	3.08E-16	DT-15a	0.0000593	2.73E-06	0.00000	16.71692	0.00388	2.28009	16.87144	0.99083	0.00002
868-16	FCT-A	Sanidine	4.0	1893.2260	0.5880	7.4272	0.2502	0.0747	0.1469	0.0829	0.1358	0.0075	0.0017	0.0339837	99.88177	27.40108	0.9163599	2.26E-16	DT-15a	0.0000593	2.73E-06	0.00000	22.52950	0.00392	3.36924	22.77966	0.98900	0.00001
868-17	FCT-A	Sanidine	4.0	662.6170	0.4295	2.5814	0.2287	−0.0473	0.1488	0.0478	0.1377	0.0033	0.0016	0.0563348	99.85363	27.58355	2.425928	7.87E-17	DT-15a	0.0000593	2.73E-06	0.00000	48.66704	0.00390	8.86098	49.46615	0.98383	0.00001
868-18	FCT-A	Sanidine	4.0	887.6470	0.4478	3.0431	0.2406	−0.0116	0.1472	−0.0178	0.1361	0.0039	0.0017	−0.017839	99.86734	31.3168	2.454874	9.28E-17	DT-15a	0.0000593	2.73E-06	0.00000	42.54075	0.00343	7.90589	43.26830	0.98317	0.00001
868-19	FCT-A	Sanidine	4.0	596.4680	0.4254	2.3677	0.2285	0.1039	0.1475	−0.0256	0.1353	0.0048	0.0017	−0.0330517	99.75862	27.04822	2.590798	7.22E-17	DT-15a	0.0000593	2.73E-06	0.00001	34.34235	0.00397	9.64903	35.67107	0.96272	0.00002
868-20	FCT-A	Sanidine	4.0	282.8150	0.4080	1.1402	0.2290	0.1225	0.1452	0.1108	0.1364	0.0014	0.0016	0.2970538	99.85302	26.663	5.31714	3.48E-17	DT-15a	0.0000593	2.73E-06	0.00000	112.24640	0.00403	20.08693	114.02720	0.98436	0.00001
868-21	FCT-A	Sanidine	4.0	557.4870	0.4254	2.0243	0.2287	−0.0550	0.1469	0.1447	0.1361	0.0066	0.0016	0.2185366	99.6469	29.51904	3.309085	6.17E-17	DT-15a	0.0000593	2.73E-06	0.00001	23.97951	0.00363	11.30032	26.50747	0.90459	0.00002
881-10	FCT-B	Sanidine	4.0	4228.1610	1.0177	16.5244	0.2457	0.1723	0.1482	0.2197	0.1345	0.0263	0.0019	0.0403301	99.81459	27.78634	0.4100287	5.04E-16	DT-15b	0.0000599	1.02E-06	0.00001	7.29317	0.00391	1.48682	7.44298	0.97985	0.00005
881-11	FCT-B	Sanidine	4.0	3353.8950	0.8188	12.8207	0.2316	0.2654	0.1469	0.2130	0.1353	0.0100	0.0017	0.0504085	99.91195	28.43086	0.5098003	3.91E-16	DT-15b	0.0000599	1.02E-06	0.00000	17.19061	0.00382	1.80702	17.28512	0.99452	0.00002
881-12	FCT-B	Sanidine	4.0	1764.4200	0.5308	6.7293	0.2307	0.0832	0.1478	0.2724	0.1358	0.0216	0.0018	0.1228569	99.63619	28.41837	0.9669898	2.05E-16	DT-15b	0.0000599	1.02E-06	0.00001	8.59476	0.00381	3.42903	9.25317	0.92880	0.00003
881-13	FCT-B	Sanidine	4.0	4332.0290	1.0640	16.9342	0.2398	0.2277	0.1472	0.2433	0.1364	0.0276	0.0019	0.0437668	99.81026	27.77883	0.3904601	5.16E-16	DT-15b	0.0000599	1.02E-06	0.00001	6.95632	0.00391	1.41623	7.09882	0.97990	0.00006
881-14	FCT-B	Sanidine	4.0	2194.7450	0.6263	8.4620	0.2310	0.1924	0.1466	0.2126	0.1370	0.0075	0.0017	0.0765426	99.8994	28.18662	0.7637557	2.58E-16	DT-15b	0.0000599	1.02E-06	0.00000	22.91481	0.00386	2.73046	23.07661	0.99298	0.00001
881-15	FCT-B	Sanidine	4.0	2599.0250	0.6420	9.6620	0.2343	0.2291	0.1469	0.2366	0.1364	0.0230	0.0018	0.0746347	99.73737	29.17773	0.7018925	2.95E-16	DT-15b	0.0000599	1.02E-06	0.00001	8.08283	0.00372	2.42471	8.43840	0.95783	0.00003
881-16	FCT-B	Sanidine	4.0	796.7530	0.4478	2.9662	0.2290	−0.0256	0.1475	0.0431	0.1356	0.0038	0.0016	0.0444911	99.85827	29.17108	2.234442	9.04E-17	DT-15b	0.0000599	1.02E-06	0.00000	42.43032	0.00372	7.72075	43.12619	0.98384	0.00001
881-17	FCT-B	Sanidine	4.0	2854.5100	0.7926	10.9422	0.2293	0.2378	0.1466	0.0113	0.1367	0.0253	0.0019	0.0031674	99.73543	28.30221	0.5885654	3.34E-16	DT-15b	0.0000599	1.02E-06	0.00001	7.57045	0.00383	2.09560	7.85487	0.96376	0.00005
881-18	FCT-B	Sanidine	4.0	2405.4890	0.6185	9.0414	0.2279	0.1831	0.1466	0.0889	0.1350	0.0163	0.0017	0.0300743	99.79837	28.87825	0.7223809	2.76E-16	DT-15b	0.0000599	1.02E-06	0.00001	10.60988	0.00376	2.52116	10.90502	0.97291	0.00002
894-10	FCT-C	Sanidine	4.0	1834.8300	0.5515	6.9164	0.2290	0.1031	0.1466	0.0880	0.1367	0.0063	0.0017	0.0386248	99.89826	28.16157	0.9253794	2.11E-16	DT-15c	0.0000585	2.91E-06	0.00000	26.92419	0.00377	3.31120	27.12669	0.99252	0.00001
894-11	FCT-C	Sanidine	4.0	2902.2600	0.8013	10.9256	0.2301	0.0813	0.1463	0.3176	0.1370	0.0146	0.0018	0.0882996	99.85122	28.18609	0.589265	3.33E-16	DT-15c	0.0000585	2.91E-06	0.00000	12.33442	0.00377	2.10668	12.51278	0.98573	0.00003
894-12	FCT-C	Sanidine	4.0	949.3380	0.4632	3.5163	0.2290	0.0218	0.1472	0.1964	0.1361	0.0030	0.0016	0.1697308	99.90796	28.66037	1.852226	1.07E-16	DT-15c	0.0000585	2.91E-06	0.00000	54.01979	0.00370	6.51321	54.41032	0.99281	0.00001
894-13	FCT-C	Sanidine	4.0	562.6810	0.4254	1.9838	0.2282	−0.1118	0.1460	0.0993	0.1356	0.0078	0.0016	0.1526266	99.58927	30.00323	3.423518	6.05E-17	DT-15c	0.0000585	2.91E-06	0.00001	21.25836	0.00353	11.50394	24.17020	0.87948	0.00002
894-14	FCT-C	Sanidine	4.0	346.2900	0.4111	1.3532	0.2398	0.0747	0.1475	0.0490	0.1374	0.0017	0.0015	0.1103476	99.85163	27.161	4.777716	4.12E-17	DT-15c	0.0000585	2.91E-06	0.00000	88.61417	0.00391	17.72070	90.36657	0.98058	0.00001
894-15	FCT-C	Sanidine	4.0	488.4230	0.4254	1.9969	0.2296	−0.0367	0.1466	−0.0040	0.1367	0.0015	0.0016	−0.0061704	99.90841	25.98273	2.966094	6.09E-17	DT-15c	0.0000585	2.91E-06	0.00000	107.10860	0.00409	11.49643	107.72260	0.99429	0.00001

Note: MSWD—mean square of weighted deviates. fA—femto amps. All data corrected for mass discrimination, detector intercalibration, blanks, radioactive decay, and interfering nucleogenic isotope reactions. Neutron flux (*J*) normalized to Fish Canyon sanidine with an age of 28.201 ± 0.046 Ma (Kuiper et al., 2008), decay constants of Min et al. (2000), and an atmospheric $^{40}Ar/^{36}Ar$ ratio of 298.56 ± 0.31 (Lee et al., 2006). Plateau and integrated ages are reported at the 2σ level of uncertainty.

TABLE 3. ANALYTICAL RESULTS FOR Sr, Nd, Pb, AND Hf ISOTOPE MEASUREMENTS

Sample name		Sample weight (mg)	$^{206}Pb/^{204}Pb$†	Error 2SE%	$^{207}Pb/^{204}Pb$†	Error 2SE%	$^{208}Pb/^{204}Pb$†	Error 2SE%	$^{87}Sr/^{86}Sr$§	Error 2SE%	$^{143}Nd/^{144}Nd$#	Error 2SE%	ε_{Nd}	$^{176}Hf/^{177}Hf$**	Error ±2σ	ε_{Hf}	$\Delta\varepsilon_{Hf}$	Mean Δ7/4	Mean Δ8/4
R12HA01	USGS	177	19.327	0.060	15.664	0.090	39.201	0.120	0.703769	0.0008	0.512772	0.0005	2.6					8	23
	ENSL*		19.3209		15.6746		39.2368							0.282965	5	6.8	0.2		
R12HA02	USGS	291	19.172	0.060	15.651	0.090	39.108	0.120	0.703586	0.0007	0.512806	0.0005	3.3					9	32
	ENSL*		19.1347		15.6534		39.0933							0.282932	6	5.7	−1.9		
R12HA03	USGS	272	18.813	0.060	15.707	0.090	39.120	0.120	0.704423	0.0008	0.512648	0.0004	0.2					17	75
	ENSL*		18.7869		15.6971		39.0875							0.282837	4	2.3	−1.2		
R120S01	USGS	227	19.099	0.060	15.619	0.090	38.876	0.120	0.703070	0.0009	0.512931	0.0004	5.7					5	16
	ENSL*		19.0752		15.6098		38.8461							0.283019	4	8.7	−2.1		
R120S03	USGS	224	19.158	0.060	15.609	0.090	38.907	0.120	0.703136	0.0008	0.512893	0.0003	5.0					4	13
	ENSL*		19.1511		15.6129		38.9220							0.282995	10	7.9	−1.9		
R120S04	USGS	247	19.029	0.060	15.645	0.090	38.959	0.120	0.703604	0.0008	0.512866	0.0008	4.5					10	35
	ENSL*		19.0224		15.6565		38.9972							0.283019	6	8.7	−0.4		
R120S05	USGS	238	19.021	0.060	15.663	0.090	39.045	0.120	0.703978	0.0007	0.512780	0.0005	2.8					12	45
	ENSL*		19.0276		15.6838		39.1137							0.282979	4	7.3	0.4		
R120S06	USGS	199	19.035	0.060	15.684	0.090	39.114	0.120	0.703994	0.0013	0.512781	0.0008	2.8					13	47
	ENSL*		19.0176		15.6780		39.0921							0.282966	4	6.9	0		
EN-1 carbonate std									0.709174	0.0009									
SRM-987 std									0.710257	0.0008									
									0.710247	0.0008									
									0.710252	0.0009									
JNd std											0.512088	0.0006							

Note: SE—standard error; std—standard.
*Powder leached in hot 6 *N* HCl for 50 min prior to dissolution.
†U.S. Geological Survey (USGS) results were corrected for blank (total Pb ~60 pg) and mass fractionation (0.12% per a.m.u.); Ecole Normale Supérieure in Lyon (ENSL) results were corrected for mass fractionation.
§Corrected for blank (total Sr ~30 pg) and mass fractionation ($^{88}Sr/^{86}Sr$ = 8.3752). The mean value of $^{87}Sr/^{86}Sr$ for three analyses of Sr standard SRM-987 was 0.710252 ±10.
#Corrected for blank (total Nd ~60 pg) and mass fractionation ($^{146}Nd/^{144}Nd$ = 0.7219). The $^{143}Nd/^{144}Nd$ value for one analysis of JNd standard was 0.512087 ± 3.
**The $^{176}Hf/^{177}Hf$ value for 11 analyses of JMC475 was 0.282158 ±4 (2 s.d.).

clinopyroxene in a matrix of plagioclase and iron-titanium oxides, and some samples preserved fresh glass and vesicles (Fig. 6). Major- and trace-element compositions of samples determined from this study from both the Toprakkale and Karasu volcanic fields support previous analyses (e.g., Polat et al., 1997; Yurtmen et al., 2000; Alıcı et al., 2001; Nikogosian et al., 2018; Oyan, 2018), in that many samples were alkaline (Fig. 4). CIPW normative mineralogy calculations indicated that the basanites are nepheline-normative. There is a clear divergence from mostly subalkaline rocks in the Karasu volcanic field to mostly alkaline rocks in the Toprakkale volcanic field, and basanite is only reported from the Toprakkale volcanic field (this and previous studies). Relative to primitive mantle, all samples from this and other studies have compositions that are enriched in LILEs and LREEs (Fig. 7), and that share more similarities to OIB. Plots of REE relative to chondrites normalized to trivalent cations, rather than normalized abundances, result in smooth curves for which their slope and curvature provide a new means of basalt discrimination (O'Neill, 2016). A plot of REE data following this approach from both the Toprakkale and Karasu volcanic fields (Fig. 8) shows that the Toprakkale and Karasu samples are largely distinct from MORB and plot in regions consistent with garnet-bearing OIB (O'Neill, 2016). Moreover, the data for these two volcanic fields plot as largely separate fields from each other, with limited overlap, consistent with the separate fields defined by their alkaline versus subalkaline compositions (Fig. 4).

^{40}Ar/^{39}Ar Geochronology

The ^{40}Ar/^{39}Ar geochronological data from this study constrain alkalic basalt volcanism in the Toprakkale and Karasu volcanic fields to between 2.63 ± 0.17 Ma and 46 ± 13 ka (Fig. 9). The Delihalil volcano is the most prominent edifice in the Toprakkale volcanic field, with ^{40}Ar/^{39}Ar plateau ages (2σ errors throughout) of 46 ± 13 ka (R12-OS1) and 50 ± 20 ka (R12-OS3) determined from basanites collected near and below the summit, respectively. The young Delihalil volcanic edifice erupted onto alkaline basalt lavas dated at 750 ± 90 ka (R12-OS4), with similar ages of 810 ± 60 ka (R12-OS5) and 780 ± 60 ka (R12-OS6) determined from samples collected along the northern margin of the Gulf of İskenderun; all three of these samples have identical geochemical and petrographic characteristics, despite being collected 30 km apart.

In the Karasu volcanic field, the basalt flow (R12HA-01) exposed near the village of Hassa produced a ^{40}Ar/^{39}Ar plateau age of 2.63 ± 0.17 Ma, and stratigraphically overlying basalt (R12HA-02) produced the youngest basalt dated from the Karasu volcanic field with a ^{40}Ar/^{39}Ar plateau age of 52 ± 16 ka. The lava flow toward the northern end of the Karasu volcanic field near the village of Fevzipaşa recorded a ^{40}Ar/^{39}Ar plateau age of 230 ± 30 ka (R12HA-03).

Sr, Nd, Hf, and Pb Isotope Geochemistry

The two basanites analyzed from the Toprakkale volcanic field have the following isotopic ratios: ^{87}Sr/^{86}Sr of 0.703070 and 0.703136; ^{143}Nd/^{144}Nd of 0.512931 and 0.512893 (ε_{Nd} = +5.8 to +5.0); ^{176}Hf/^{177}Hf of 0.283019 and 0.282995 (ε_{Hf} = +8.7 to +7.9); ^{206}Pb/^{204}Pb of 19.087 and 19.155; and ^{208}Pb/^{204}Pb of 38.861 and 38.915, where the Pb isotope values are averages of those obtained at the USGS and ENSL. The ^{143}Nd/^{144}Nd and ^{87}Sr/^{86}Sr values for Toprakkale basanites (Parlak et al., 2000; Bağcı et al., 2011; this study) are among the highest and lowest values, respectively, when compared to Miocene mafic Anatolian lavas (cf. compilations by McNab et al., 2018; Uslular and Gençalioğlu-Kuşcu, 2019a; Fig. 10 herein). They also overlap with those of the most depleted mantle-like basalts in northern and central Arabia (Bertrand et al., 2003; Ma et al., 2011), albeit displaced to slightly lower ^{87}Sr/^{86}Sr. Plots of ^{176}Hf/^{177}Hf and ^{143}Nd/^{144}Nd lie within the distribution of oceanic mantle compositions defined by MORB and OIB (deviation from the mantle array, $\Delta\varepsilon_{Hf}$, of –2; Fig. 10), and they resemble those of late Miocene basalts of western Anatolia (Aldanmaz et al., 2015). Pb isotope compositions lie close to, but above, the Northern Hemisphere reference line (NHRL; Hart, 1984) in ^{207}Pb/^{204}Pb-^{206}Pb/^{204}Pb and ^{208}Pb/^{204}Pb -^{206}Pb/^{204}Pb space (Δ7/4 deviations of ~5 and Δ8/4 of ~15; Fig. 10), similar to those of Miocene basalts from the northern and central Arabia plate as well as to those of late Miocene and Quaternary basalts in western Anatolia.

Quaternary alkaline Toprakkale basalts have somewhat higher ^{176}Hf/^{177}Hf ratios (0.282966–0.283019; ε_{Hf} = +6.9 to +8.7) than alkaline Karasu basalts (0.282837–0.282965; ε_{Hf} = +2.3 to +6.8) and somewhat higher ^{143}Nd/^{144}Nd ratios (0.512781–0.512866 and ε_{Nd} = +2.8 to +4.5, versus 0.512648–0.512806 and ε_{Nd} = +0.2 to +3.3). Plots of ^{176}Hf/^{177}Hf and ^{143}Nd/^{144}Nd values lie within the oceanic mantle array ($\Delta\varepsilon_{Hf}$ of ~–2.1 to +0.4; Fig. 10), in this respect resembling late Miocene basalts of western Anatolia (Aldanmaz et al., 2015), in contrast to contemporaneous near-primary basalts in central Anatolia, which have similar Nd isotope ratios that are displaced to ε_{Hf} values ~6 units higher (Reid et al., 2017). The ^{206}Pb/^{204}Pb values for alkaline Toprakkale basalts are relatively invariant (19.025 ± 0.001), whereas those for Karasu basalts vary from 18.800 to 19.324; ^{208}Pb/^{204}Pb ratios overlap but are displaced to lower values in Toprakkale basalts (38.978–39.103) relative to Karasu basalts (39.101–39.219). More generally, Pb isotope ratios extend to values well above the NHRL in ^{207}Pb/^{204}Pb-^{206}Pb/^{204}Pb and ^{208}Pb/^{204}Pb -^{206}Pb/^{204}Pb space (Δ7/4 up to 17 and Δ8/4 up to 75; Fig. 10). Although there is some overlap in radiogenic isotope ratios, the combined data highlight differences between the two Quaternary volcanic fields, with the Toprakkale basanites displaying the most restricted and depleted mantle-like compositions.

DISCUSSION

Magma Sources and Melt Equilibration Depths: Toprakkale Basanites

The Hf and Pb isotope compositions obtained for Toprakkale basanites, considered together with Sr and Nd isotope data, provide important new constraints on their mantle source(s). New and published Sr isotope data for Toprakkale basanites exhibit minor variability (average ^{87}Sr/^{86}Sr = 0.70315 ± 0.00007 [1 sd]; *n* = 14) despite approximately twofold variations in La/Nb, La/Yb, and Ba/Nb. Helium isotope values averaging R/R$_a$ = 7.6 ± 0.3 obtained for five Toprakkale basanites

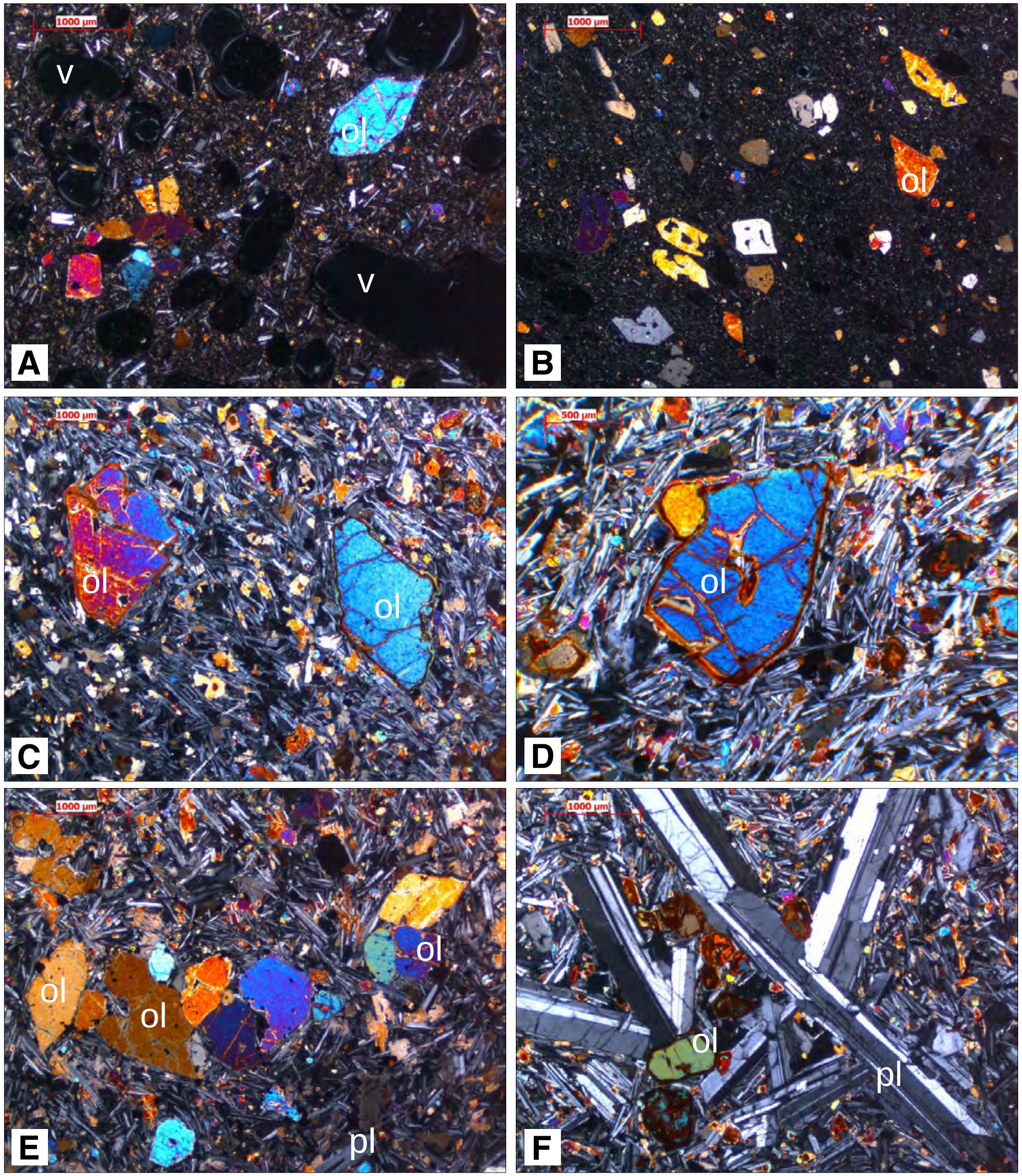

Figure 6. Photomicrographs of selected samples from the Toprakkale and Karasu volcanic fields: (A–B) basanites from Delihalil volcano (R12-OS3 and R12-OS1), (C–D) alkali basalts along the Yumurtalık fault (Botaş) (R12-OS5 and R12-OS6), and (E–F) alkali basalts from near Hassa and İslahiye (R12-HA2 and R12-HA3). Note the glassy, vesicular (v) groundmass and euhedral-subhedral skeletal olivine (ol) phenocrysts in the basanites in A and B vs. the large euhedral olivine (ol) and plagioclase (pl) phenocrysts in the intergranular groundmass of the alkali basalts.

are indistinguishable from those of MORB mantle (Italiano et al., 2017). More generally, the isotopic features of the Toprakkale basanites, and specifically the Hf and Pb isotopic data reported here, lie within mantle arrays defined by the isotopic characteristics of oceanic basalts, and close to those with a common mantle component (“C”; Hanan and Graham, 1996). As noted previously by several authors (Polat et al., 1997; Alıcı et al., 2001; Yurtmen et al., 2002; Oyan, 2018; Nikogosian et al., 2018), the incompatible element characteristics of the basanites resemble those of OIB (Fig. 10). Thus, both isotopic and incompatible element characteristics of the Toprakkale basanites indicate that they are OIB-type, asthenosphere-derived melts largely unmodified by crustal contributions.

Depths of peridotite-derived melt equilibration can be estimated using olivine-orthopyroxene-melt barometry (Lee et al., 2009; Plank and Forsyth, 2016). Relevant conditions for melt equilibration are assumed to be: (1) primary melts in equilibrium with an Fo_{89} source (a fairly conservative estimate judging by Arabian mantle xenoliths; Stern and Johnson, 2010); (2) minimum water contents given by H_2O (ppm) = 200•Ce (ppm), a relation typical for oceanic basalts (Reid et al., 2017); and (3) $Fe^{2+}/\Sigma Fe$ = 0.18 and 0.16 for the basanites and basalts, respectively, extrapolated based on estimated water contents (Kelley and Cottrell, 2009). Barometer uncertainty is ±8 km (Plank and Forsyth, 2016). Basanites were filtered for Mg# >55 and CaO/Al_2O_3 >0.6, since those with lower values are more likely to have experienced clinopyroxene fractionation (Italiano et al., 2017).

Basanites could have been derived by partial melting of garnet pyroxenite (Keshav and Gudfinnsson, 2004), hornblende peridotite (Pilet et al., 2008), or, in this study area specifically, phlogopite-bearing garnet peridotite (Oyan, 2018). The latter source was identified for Toprakkale basalts based on the apparent buffering of alkalis and alkaline earth elements relative to LREEs during melting. Pressure estimates for basanite melt equilibration with peridotite derived from new and published chemical analyses average 2.7 ± 0.2 GPa (n = 31; data in Supplemental Table S1[1]), corresponding to a mean depth estimate of 91 ± 3 km, assuming an average crustal thickness of 30 km as indicated by seismic data (Abgarmi et al., 2017). Inferred water contents are 1.0–1.6 wt% but could be higher if the source is more hydrous than typical suboceanic mantle. Increasing water contents by a factor of two, for example, reduces the depth estimate by only 2 km. Allowing for an uncertainty in $Fe^{2+}/\Sigma Fe$ of ±0.05 (likely a maximum) would increase the depth uncertainty by ±4 km. The ~90 km depth estimate for melt equilibration is consistent with REE and HFSE evidence for Toprakkale basanite generation in the garnet stability field (Fig. 8; Oyan, 2018; Nikogosian et al., 2018). The corresponding equilibration pressures are within 0.3 GPa of values reported previously (Çoban, 2007; Reid et al., 2017; Nikogosian et al., 2018), albeit for a larger number of samples and with differing assumptions about primary melt compositions. These pressure

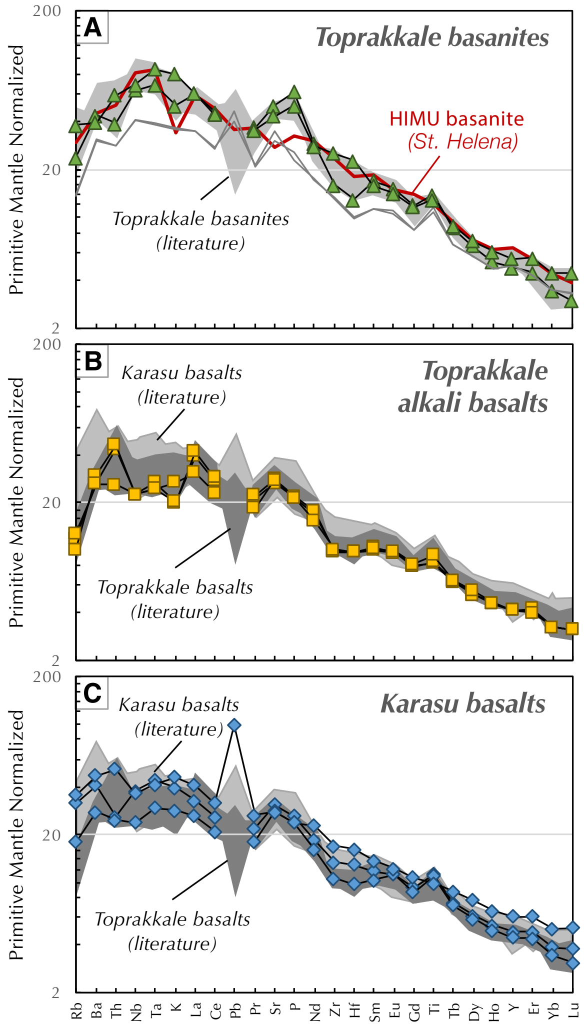

Figure 7. Primitive mantle–normalized (McDonough and Sun, 1995) incompatible trace-element diagrams for (A) Toprakkale basanites, (B) Toprakkale basalts, and (C) Karasu basalts. Fields show literature data, with some anomalous literature results excluded (Zr in three basalts where Zr/Hf <16 and Nb in two basalts where Nb/Ta ~11). HIMU—high μ = high $^{238}U/^{204}Pb$. Data sources are Oyan (2018), Nikogosian et al. (2018), and summary by Uslular and Gençalioğlu-Kuşcu (2019a).

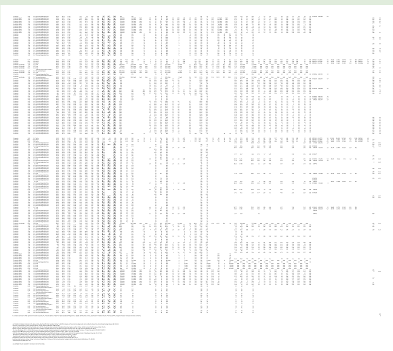

[1]Supplemental Material. Table of published geochemical and isotopic data and pressure estimates for volcanic rocks of the Toprakkale and Karasu volcanic fields. Please visit https://doi.org/10.1130/GEOS.S.13011689 to access the supplemental material, and contact editing@geosociety.org with any questions.

estimates are considerably lower than the value of 3.7 GPa estimated by Oyan (2018) using the barometer formulation of Lee et al. (2009). Much of this difference is probably attributable to different barometer formulations.

Magma Sources and Melt Equilibration Depths: Toprakkale and Karasu Basalts

The isotopic and enriched trace-element compositions of basalts from the Toprakkale and Karasu volcanic fields have been variously ascribed to subduction-modified sources (Yurtmen et al., 2000; Italiano et al., 2017), mantle signatures overprinted by crustal contributions (Alıcı et al., 2001; Oyan, 2018), and mantle source heterogeneity (Nikogosian et al., 2018). The elevated $^{207}Pb/^{204}Pb$ and $^{208}Pb/^{204}Pb$ values of the basalts could, by analogy with Miocene central Anatolian basalts, reflect metasomatism of the lithosphere by a subduction-related component. However, the basalts are largely characterized by positive HFSE anomalies (e.g., $La/Nb_N = 0.6–0.9$; Fig. 7), in contrast to the pronounced negative anomalies in relatively primitive subduction-influenced Miocene basalts from central Anatolia (La/Nb_N mostly >2; Reid et al., 2017; Uslular and Gençalioğlu-Kuşcu, 2019b). The oceanic mantle array–like Hf-Nd isotopic characteristics of Toprakkale and Karasu basalts also contrast with Hf isotope signatures that are displaced from the oceanic mantle array in central Anatolian basalts (Reid et al., 2017). Instead, incompatible element patterns for the A³ triple junction basalts are broadly similar to, albeit at lower abundances than, the basanites, as permitted if the basalts were generated by a greater degree of melting (Bağcı et al., 2011; Oyan, 2018).

The variations in new Hf, Δ7/4, and Δ8/4 isotope data along with new and previously determined Sr and Nd isotope ratios additionally require either source heterogeneity and/or contributions from more than one source. Paired isotope ratios from both volcanic fields define broadly linear arrays that trend from the basanites to the most evolved basalt (Fig. 10), despite occurring in two spatially distinct areas. The more radiogenic isotopic compositions of the alkaline Toprakkale basalts relative to the basanites could be the result of 2%–5% crustal assimilation (Oyan, 2018), with olivine-normative basalts displaced even farther in Nd and Hf isotope space. The somewhat different isotopic trends defined for the two volcanic fields would require different crustal end members if they resulted from crustal assimilation.

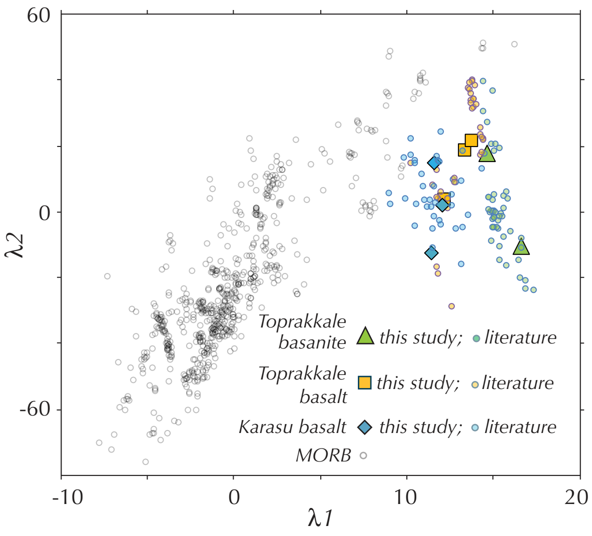

Figure 8. Plot of rare earth elements (REEs) relative to chondrites following the method of O'Neill (2016), in which the petrogenetic vectors λ1 and λ2 relate to the slope and curvature of chondrite-normalized REE plots. Data on this diagram from the Toprakkale and Karasu volcanic fields (this study and cited literature) plot as distinct fields relative to ocean-floor basalts (mid-ocean-ridge basalt [MORB]) from O'Neill (2016). The position on this diagram to the right of MORB, where most of the Toprakkale and Karasu samples plot, is consistent with contributions from melts generated from an oceanic-island basalt–like garnet-bearing mantle source (O'Neill, 2016).

In detail, interelement ratios for the basalts (compiled data) and olivine-hosted melt inclusions (Nikogosian et al., 2018) in the Toprakkale volcanic field are more MORB-like than the basanites, an observation that is not easily reconciled with crustal assimilation. This has led to the hypothesis that at least some of the trace-element heterogeneity exhibited by the basalts is derived from a more MORB-like mantle source than that of the basanites (Nikogosian et al., 2018), although the more radiogenic Sr, Nd, and Hf isotope signatures of the basalts do not support this interpretation.

Pressure estimates obtained for the Toprakkale and Karasu basalts, assuming melt equilibration with peridotite, average 1.9 ± 0.1 GPa (n = 26) and 1.8 ± 0.3 GPa (n = 15), respectively (data filtered as described above). These pressures correspond to average depth estimates of 64 ± 4 km and 63 ± 8 km, or ~30 km shallower than those estimated for the basanites. Such pressures are similar to those of 1.8–2.3 GPa and 2.05–2.17 GPa obtained in previous investigations (Reid et al., 2017; McNab et al., 2018; Nikogosian et al., 2018) and imply depths in the spinel peridotite stability field, contributions from which have been identified by other authors (Italiano et al., 2017; Oyan, 2018). Melting in the presence of garnet is also apparent from REE and HFSE systematics (Bağcı et al., 2011; Nikogosian et al., 2018) and was likely inherited as melt upwelled from depth; the "garnet-signatures" would not be erased by equilibration or mixing with more shallowly derived melts. Inferred water contents are from 0.6 to 1.4 wt%.

Reconciling Melt Equilibration Depths with Geophysical Images of Mantle Structure

Data from this and previous studies are consistent with a model in which both the Toprakkale and Karasu volcanic fields were derived by partial melting of an oceanic basalt–like asthenospheric mantle source (basanites) with possible contributions from lithospheric mantle ± crustal source (basalts). However, observed geochemical and isotopic variations

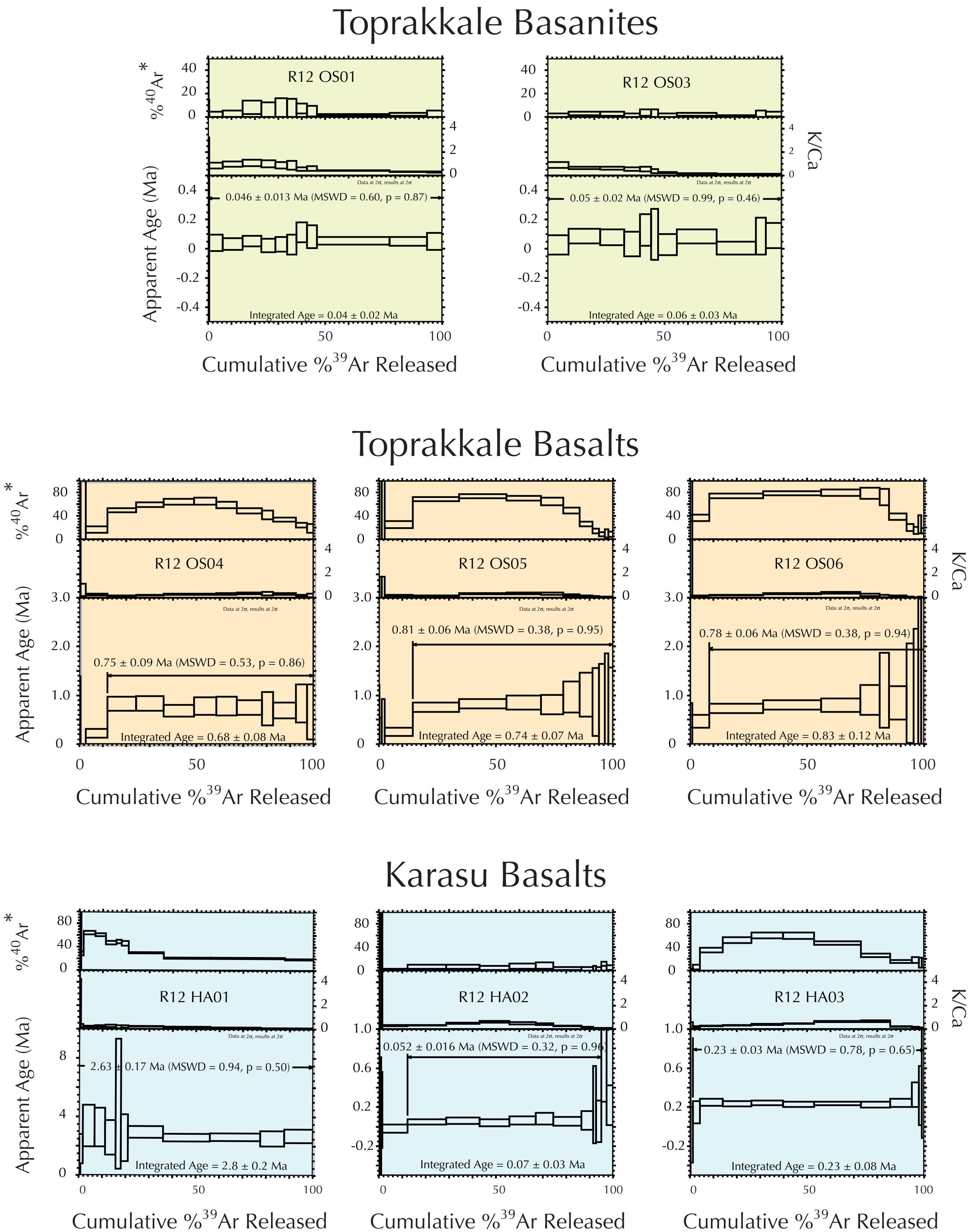

Figure 9. $^{40}Ar/^{39}Ar$ **age spectrum plots of samples from this study. Basanite samples from Delihalil volcano are shaded green, and other alkaline basalts from Toprakkale volcanic field are shaded orange. Basalt samples from the Karasu volcanic field are shaded blue. Uncertainties on all** $^{40}Ar/^{39}Ar$ **ages are given at the 2σ level of confidence. MSWD—mean square of weighted deviates.**

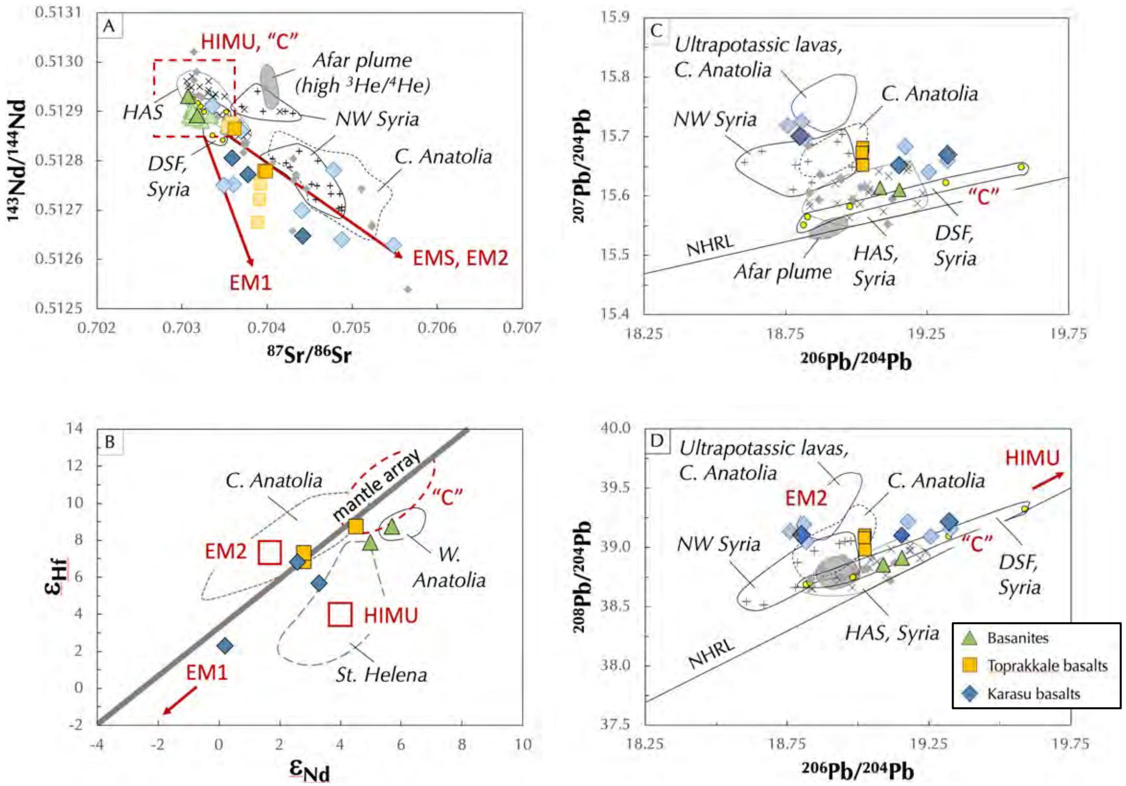

Figure 10. Plots of (A) $^{143}Nd/^{144}Nd$ vs. $^{87}Sr/^{86}Sr$, (B) ε_{Hf} vs. ε_{Nd}, (C) $^{207}Pb/^{204}Pb$ vs. $^{206}Pb/^{204}Pb$, and (D) $^{208}Pb/^{204}Pb$ vs. $^{206}Pb/^{204}Pb$ for samples from the Toprakkale and Karasu volcanic fields. Darker large symbols with black margins are from this study (see legend and Fig. 4); lighter large symbols with colored margins are from Arger et al. (2000), Parlak et al. (2000), Alıcı et al. (2001), Bağcı et al. (2011), and Oyan (2018). Also shown are comparative data of mainly Miocene rocks for central Anatolia (Şen et al., 2004; Reid et al., 2017; Uslular and Gençalioğlu-Kuşcu, 2019b) and locations on the northern Arabia plate: Karacadağ (small diamonds—Pearce et al., 1990; Şen et al., 2004; Lustrino et al., 2010; Keskin et al., 2012; Ekici et al., 2014); Dead Sea fault (DSF), Syria (small circles—Ma et al., 2011); northwestern Syria (crosses—Krienitz et al., 2006), Harrat Ash Shalam (HAS), Syria (x's—Shaw et al., 2003), and Afar plume (Pik et al., 1999). General locations of mantle end-member HIMU (high-μ = high $^{238}U/^{204}Pb$), common mantle (C), and the enriched mantle end-members EM1 and EM2, along with eastern Mediterranean sediments (EMS; Klaver et al., 2015) and the location of the mantle array (Vervoort et al., 1999), are shown for reference. NHRL—Northern Hemisphere reference line.

between the volcanic fields may also be impacted by the regional tectonic complexities of an evolving triple junction, perhaps explaining why alkaline basalts occur in both volcanic fields while basanites have only been identified in the Toprakkale volcanic field. Moreover, the melting depths inferred for the Toprakkale basanites are not only the deepest from either volcanic field, but they are also restricted to an area of transtension between the major strands of the East Anatolian fault zone. The basanites are the most depleted mantle-like rocks in terms of Sr, Nd, and Hf isotopic data, with low overall variability compared to the less mafic rocks from both the Karasu and Toprakkale volcanic fields. The compositions of the basanites support relatively deep melting (mostly 80–105 km, averaging ~90 km), in contrast to shallower melting inferred for the Toprakkale alkaline basalts (mostly 60–70 km; Polat et al., 1997; Yurtmen et al., 2000; Bağcı et al., 2011; Oyan, 2018).

Significant variations in crustal and upper-mantle seismic structure are found near the A³ triple junction. Using P-wave receiver functions, Abgarmi et al. (2017) imaged a significant decrease in crustal thickness at the transition from the central Taurus Mountains (>40 km) to the Adana Basin (~30 km). This thinning is likely due to the extensional component of the dominantly transtensional A³ triple junction. By combining Rayleigh wave dispersion measurements with the receiver function measurements of Abgarmi et al. (2017) and jointly inverting to solve for the three-dimensional shear-wave velocity structure of central Anatolia, Delph et al. (2017) observed a widespread and vertically extensive fast shear-wave velocity anomaly beneath the central Taurus Mountains and western Adana Basin, which they interpreted as the underthrusted Cyprean slab. These fast velocities abruptly terminate near the central Adana Basin, transitioning to very slow upper-mantle shear velocities beneath the Iskenderun Basin and areas farther east (<4.2 km/s at >60 km; Fig. 11). These observations are consistent with thin crust (~30 km) and thin lithospheric mantle (~30 km) underlain by a hot and shallow melt-bearing asthenosphere beneath the A³ triple junction and extending beneath the Arabia plate.

Excluding the basanites, melt equilibration depths for Quaternary basaltic magmatism in the Toprakkale and Karasu volcanic fields agree with the seismically imaged lithosphere-asthenosphere boundary as defined by a sharp transition at ~60 km to very slow upper-mantle shear velocities (Fig. 11). A general (mostly within 5 km) co-occurrence between melt equilibration and lithosphere-asthenosphere boundary depth from seismic imaging has also been observed elsewhere in Turkey (Reid et al., 2017) and in the western United States (Reid et al., 2012; Plank and Forsyth, 2016). The correlation can be explained by partial melts being able to segregate from upwelling mantle as the relatively rigid lithospheric lid is approached. Chemical and isotopic heterogeneity exhibited by these basalts would therefore reflect hybridization of asthenosphere-derived melts with lithosphere that is being thermally and chemically eroded, except where arising from crustal contamination.

The relatively thin lithosphere (~50–60 km) below the İskenderun Basin extends farther to the east beneath the Arabian foreland (Angus et al., 2006; Delph et al., 2017) and is much thinner than the Arabian Shield farther to the south, which has a lithospheric thickness of >100 km (Hansen et al., 2007). The comparatively thin Arabian foreland lithosphere may represent its original thickness as a continental passive margin prior to collision. Another possibility is that thinning of the Arabian lithospheric mantle is occurring through an asthenospheric mantle erosion process, which could be linked to crustal tectonics and magmatism along the East Anatolian fault zone. For example, northward mantle flow beneath the Arabia plate (Becker and Faccenna, 2011) coupled with the abrupt decrease in lithospheric thickness from >100 km to ~60 km could lead to shear-induced, edge-driven convective erosion of the lithospheric mantle (e.g., Kaislaniemi and van Hunen, 2014). The convective removal of lithospheric mantle due to significant lithosphere-asthenosphere boundary topography has also been invoked in Australia as well as near the edges of other subduction zones (Davies and Rawlinson, 2014; Levander et al., 2014). Such edge-driven convection may provide a mechanism for adiabatic decompression melting of mantle that has entrained blocks of detached lithosphere, explaining the occurrence of localized small-volume basalts along the high-angle plate-boundary faults (East Anatolian fault zone) and also their geochemical and isotopic variations.

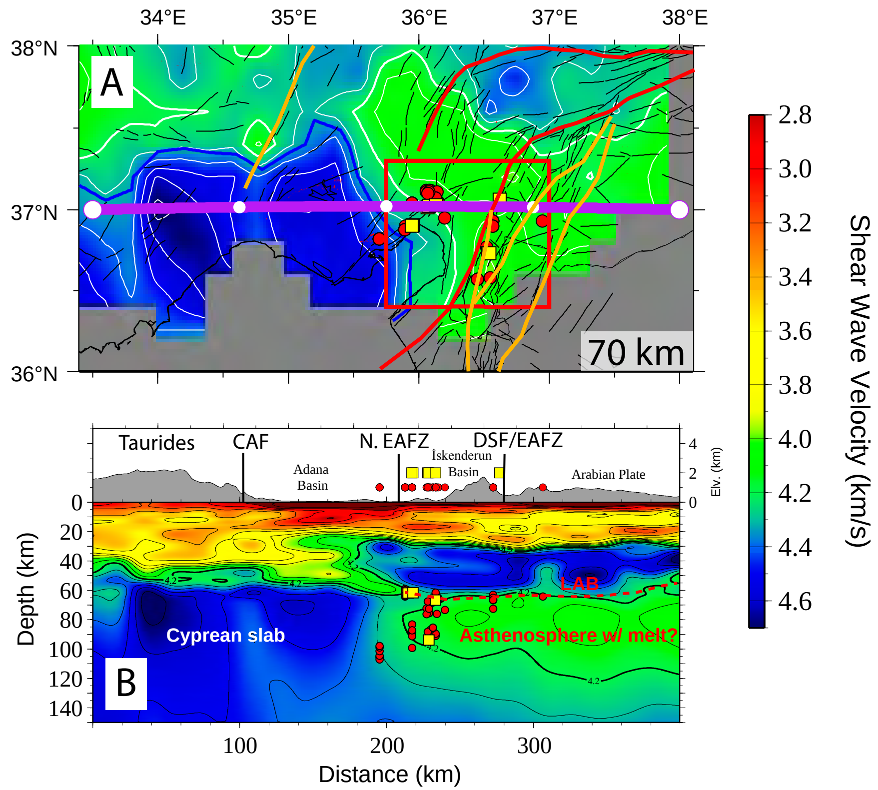

Figure 11. (A) Distribution of major fault patterns near the Cyprus-Arabia-Anatolia triple junction overlain on upper-mantle shear-wave velocity (70 km below surface). Faults in red correspond to the main and northern strands of the East Anatolian fault zone. Faults in orange include the Dead Sea fault zone, the Central Anatolian fault, the Yesemek fault, and the Aaferin fault (see Fig. 2 for locations). Velocities reach <4.2 km/s in the upper mantle, indicating the presence of melt under much of the region. Blue contour demarcates the edge of Cyprean slab from Delph et al. (2017). Volcanism only appears to reach the surface east of the Cyprean slab where faulting occurs near the triple junction. Yellow squares are samples from this study; red circles are samples from other studies cited in text. Purple line is cross-section location for part B with white circles demarcating 100 km intervals along line. (B) Cross section through the Arabia-Africa-Anatolia (A^3) triple junction (modified from Delph et al., 2017). Estimates of melting equilibration depths for primary melts are shown, if obtained, for samples analyzed in this study (yellow squares) and for compiled literature data (red circles). Dashed red line shows the approximate location of the lithosphere-asthenosphere boundary (LAB). CAF—Central Anatolian fault; N. EAFZ—northern strand of the East Anatolian fault zone; DSF/EAFZ—Dead Sea fault/East Anatolian fault zone.

Similarly, the Quaternary to recent mafic magmatism in the Karacadağ volcanic field in the Arabian foreland farther east (e.g., Lustrino et al., 2010; Ekici et al., 2014; Ekici and Macpherson, 2019) may also have resulted from such a process, supporting regional-scale mantle lithospheric erosion of the Arabian foreland, extending into the A^3 triple junction. Indeed, magmatism at the Karacadağ volcanic field extends back to ca. 17 Ma (Ekici and Macpherson, 2019), showing a minor southeastward migration through time along a major regional fault (Keskin et al., 2012), consistent with the convective removal of the lithospheric mantle.

The considerably deeper melt equilibration depths obtained here and in previous investigations of the Toprakkale basanites (~90 km; Reid et al., 2017; Oyan, 2018; Nikogosian et al., 2018) appear to require a different process of melt generation. The basanites could be melts of an oceanic basalt–like sublithospheric mantle source, as supported by the Pb and Hf isotope data reported here and recognized previously; they appear to define one end member for the basalts (Fig. 10). Basanite melts could simply have separated from mantle upwelling along an adiabat at depths greater than the lithosphere-asthenosphere boundary, as observed in the western Grand Canyon region of the western United States and proposed for the Sivas region of central Anatolia (Plank and Forsyth, 2016; Reid et al., 2019).

A signature feature of the basanites is their noticeable depletions of alkalis and Pb relative to similarly incompatible elements, a signature that is also observed in other Toprakkale basanites attributed to HIMU-OIB mantle sources (where HIMU stands for high $\mu = {}^{238}U/{}^{204}Pb$; Fig. 7; Bağcı et al., 2011; Oyan, 2018; Nikogosian et al., 2018). More subtle deviations from HIMU are also present in some samples of this study with elevated Sr and P, and sometimes lower Zr and Hf relative to nominally similar incompatible elements. Basanites from oceanic islands that exhibit similar geochemical characteristics (e.g., St. Helena, Cook-Austral islands) are inferred to have been derived from upwelling mantle plumes. The lack of high (>20) ${}^{206}Pb/{}^{204}Pb$ (or HIMU) in the Toprakkale basanites would reflect insufficient time for radiogenic ${}^{206}Pb$ ingrowth after recycling of oceanic crust into the plume source. Alternative origins have been proposed for HIMU signatures in the Toprakkale volcanic field and other localities in the Anatolia-Arabia region via melting of hydrous metasomatic veins impregnated within, or at the base of, the lithosphere or by reactive porous flow of melts migrating through the lithosphere (Bağcı et al., 2011; Aldanmaz et al., 2006; Oyan, 2018).

In this study, the seismologically imaged depth of the lithosphere-asthenosphere boundary directly below the Toprakkale volcanic field is similar to melt equilibration depths for the basalts (~60 km). We therefore considered three alternatives to explain why melt extraction of the basanites may have taken place at greater depths than the lithosphere-asthenosphere boundary: (1) Geochemical signatures of the nearby Cyprean slab lithospheric mantle (Fig. 11) were incorporated near the source; (2) the basanite melts were generated by heating and partial melting of suspended blocks within the asthenospheric mantle that delaminated/dripped from the base of the lithospheric mantle; or (3) the pressure estimates for basanite melt equilibration are invalid. Regarding the last hypothesis, melt equilibration depths could be in error if the source lithology lacked orthopyroxene and/or olivine (e.g., if it were a pyroxenite) or if there were considerable pyroxene fractionation after melt extraction. Previous investigations (e.g., Oyan, 2018) and our data filtering suggest that neither scenario applies here.

Basanites are only observed in the Toprakkale volcanic field, which is separated from the Karasu volcanic by the East Anatolian fault zone and the Amanos mountains (Fig. 2). Assuming that the melt generation depths of ~90 km are reliable, the Toprakkale basanites originated from ~30 km below the underlying seismically imaged lithosphere-asthenosphere boundary (Fig. 11). Irregular plate geometries at depth could induce small-scale convection cells, perhaps leading to localized heating and partial melting of the neighboring Cyprean slab lithospheric mantle. Because the Cyprean slab at depth occurs below the western Adana Basin (Delph et al., 2017), just west of the A^3 triple junction, melt generation and migration near the adjacent Cyprean slab edge may follow permeable lithospheric-scale pathways associated with this plate boundary as has been proposed for oceanic transform faults (Hékinian et al., 1995). Although there is no a priori reason that such a source would impart HIMU-like trace-element signatures on the basanites, we cannot discount a hypothesis wherein the basanites are partial melts derived from the Cyprean slab lithospheric mantle at depths of ~90 km. Another mechanism for explaining the deeper melting depths of the basanites is that they represent melts sourced from lithospheric blocks within the asthenosphere, for example, remnants of the Bitlis slab or blocks detached via convective removal from the base of the Anatolian lithosphere. This latter hypothesis is consistent with the abrupt contrast in seismically imaged lithospheric thicknesses and the spatial distribution of Quaternary basalts farther east within the Arabian foreland (e.g., Chorowicz et al., 2005; Stern and Johnson, 2019), and it may be the process that is largely responsible for the shallow lithosphere-asthenosphere boundary beneath eastern Anatolia. In either case, the basanites appear to include some contribution of partial melting of lithospheric mantle at ~90 km depth that was either "attached" to the Cyprean slab, or in the form of "detached" blocks foundered within the asthenospheric mantle.

Plate-Boundary Volcanism and Tectonic Escape of Anatolia

The combined K-Ar and ${}^{40}Ar/{}^{39}Ar$ ages indicate that the initial stages of volcanism began in the Toprakkale and Karasu volcanic fields with first appearances of alkaline volcanism at 2.25 ± 1.56 Ma (2 sd; Arger et al., 2000) and 2.63 ± 0.17 Ma (this study), respectively. Basaltic volcanism in the Karasu valley began nearly 1 m.y. earlier than previously known (1.57 ± 0.08 Ma) from the study by Rojay et al. (2001). The new ${}^{40}Ar/{}^{39}Ar$ data from this study support a semicontinuous 2.5 m.y. history of volcanism within the Karasu valley, consistent with borehole data showing intercalated basalt and fluvial-lacustrine sedimentation with significantly more sedimentation occurring along the western margin of the valley (Rojay et al., 2001). The 46 ± 13 ka basanite lava erupted from the Delihalil volcano, and the 50 ± 20 ka alkaline basalt lava flow in the Karasu valley also demonstrate that volcanism remains intermittently active in both the Toprakkale and Karasu volcanic fields. The initial period of volcanism in both volcanic fields was limited, as only one sample from each area records evidence of volcanism prior to 2 Ma, providing the earliest evidence of magmas erupted along developing fault boundaries (Fig. 12). However, between 2 and 1 Ma, more widespread basaltic volcanism was localized along the Karasu fault zone and along the Yumurtalık fault zone in the Karasu and Toprakkale volcanic fields, respectively. Over the last 1 m.y., volcanism appears to have intensified and produced most of the exposed volume of volcanic rocks within both volcanic fields. These post–1 Ma volcanic rocks are focused within larger eruption centers such as the Delihalil volcano in the Toprakkale volcanic field and a number of smaller volcanic cones within the Karasu volcanic field along clearly defined fault segments. Although poorly constrained, there is some indication that volcanism within the Karasu volcanic field may have migrated toward the Arabian plate over the last 200 k.y. (Fig. 12).

Important questions in understanding the tectonic evolution of the A³ triple junction are: (1) When did the modern fault systems bounding the triple junction become active, and (2) can the Quaternary lavas associated with the fault system provide chronological constraints on fault dynamics? Given that Quaternary volcanism is clearly localized along fault segments and releasing and restraining bends of the East Anatolian fault zone (Tatar et al., 2004; Kavak et al., 2009), it seems likely that volcanism postdated initiation of major strike-slip activity related to Anatolian tectonic escape, and, based on our new results, associated magmatism did not occur until 2.63 ± 0.17 Ma. While this provides a lower limit on the tectonic escape of the Anatolia microplate along the western terminus of the East Anatolian fault zone, others have suggested initiation of the East Anatolian fault zone by ca. 4 Ma and possibly as early as 7 Ma near the Gulf of İskenderun (e.g., Westaway, 2003, 2004; Seyrek et al., 2008). A reasonable upper limit to the inception of the East Anatolian fault zone is probably a few million years greater than the $^{40}Ar/^{39}Ar$ basalt ages, judging from estimates of the time required for initial melt generation and transfer through the crust (Cesare et al., 2009; Ferrari, 2004; Karakas et al., 2017). These estimates agree with independent geologic evidence supporting the transition from regional transpression to transtension and from "proto-escape" to active escape of the Anatolia plate along the East Anatolian fault zone around 5 Ma (e.g., Yılmaz et al., 2006).

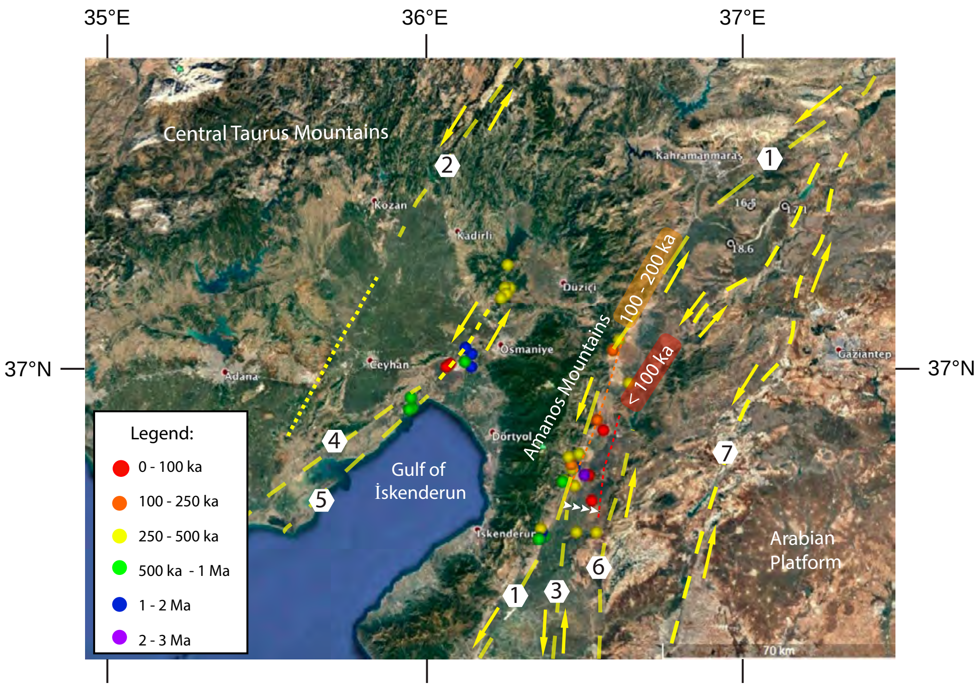

Figure 12. Temporal and spatial locations of K-Ar and $^{40}Ar/^{39}Ar$ data (this study and all published data cited in the text; Supplemental Table S1 [see text footnote 1]) from the Toprakkale and Karasu volcanic fields (and Miocene dates from the Narlı basin) plotted on a Google Earth satellite image. The positions of major faults associated with the Arabia-Africa-Anatolia (A³) triple junction are plotted in yellow, and specific fault names keyed to numbers are as follows: (1) main southern strand of East Anatolian fault zone; (2) northern strand of East Anatolian fault zone (EAFZ); (3) Dead Sea fault zone; (4) Karataş fault: (5) Yumurtalık fault; (6) Yesemek (East Hatay) fault; (7) Aaferin fault. Data from the Toprakkale volcanic field indicate punctuated volcanism in close proximity to faults. Data from the Karasu volcanic field are similarly associated with faulting. Data from the Karasu volcanic field exhibit a possible record of eastward migration of active volcanism (indicated by white arrows) over the last 200 k.y.

Plate Reorganization and Triple Junction Initiation and Migration

Prior to the late Miocene, a subduction/collision plate boundary existed between Nubia (Africa-Arabia) and Eurasia (Anatolia), and this is expressed geologically in the field by imbricated Kızıldağ and Baer Bassit ophiolite sequences (Bitlis suture). This plate boundary was disrupted in the early–mid-Miocene by an apparent tear in the downgoing slab (Nubia), and eventual breakoff of the Bitlis slab segment (Portner et al., 2018; Reid et al., 2019). Today, this boundary is represented by subduction of discrete segments of the Africa plate beneath Anatolia, as trench retreat is active along the Hellenic and Cyprus trenches, respectively. Based on seismic tomography in the eastern Mediterranean (e.g., Biryol et al., 2011; Portner et al., 2018), the following three distinct subduction/collision domains are observed: (1) Along the Hellenic arc, an intact slab extends continuously into the lower mantle below the Aegean; (2) in central Anatolia, subduction occurs near the Cyprus trench, and the slab appears to be mostly intact, although severely distorted with several apparent minor tears; and (3) northward of the Bitlis suture, which represents the oldest stage of the ongoing subduction/breakoff process, no slab is readily identifiable, and only relatively small, fast anomalies interpreted as detached or broken fragments of the Bitlis slab are visible in the upper mantle.

While tearing and breakoff of parts of the subducting Nubia slab were occurring at the former Bitlis subduction/collision zone, Arabia was beginning to separate and rotate away from Africa, and the northward propagation of the Red Sea rift ultimately led to the propagation of the Dead Sea fault zone into our study area by the late Miocene, just prior to the Pliocene formation of the East Anatolian fault zone (e.g., Reilinger et al., 2006; Bosworth and Stockli, 2016). Extrusion of the Anatolia plate since 5 Ma, currently moving at 21 mm yr^{-1} (relative to a stable Eurasia) and partly driven by the 15 mm yr^{-1} advance of Arabia and its collision with Eurasia along the Bitlis and Zagros sutures (e.g., Reilinger et al., 2006), results in a dynamic tectonic coupling along the more slowly (5 mm yr^{-1}) advancing African plate. The inception and continuing development of the A^3 triple junction plate boundaries are intimately tied to the evolving Dead Sea–East Anatolian fault zone system and the ways in which these faults respond to deformation related to tectonic escape of the Anatolia plate. The oblique nature of the relative plate motions in the fault-fault-trench triple junction system is inherently unstable (Dewey et al., 1986) and will continue to cause the A^3 triple junction to migrate until a more stable configuration is reached.

Although transfer of left-lateral deformation from the Dead Sea fault zone to the East Anatolian fault zone is fairly well accepted, and the East Anatolian fault zone represents a major component of the A^3 triple junction, a less-well-known feature is the offshore linkage of the northern East Anatolian fault zone to the Kyrenia-Misis fault and the way in which the main strand of the East Anatolian fault zone links to the Cyprus trench (e.g., Duman and Emre, 2013). The exposed broad zone of distributed deformation, transtension, and basin development between the two main strands of the East Anatolian fault zone clearly continues offshore, represented by the Adana-Cilicia and İskenderun basins. Indeed, continuing rollback of the subducting Cyprean slab and associated trench retreat may explain some of the plate kinematics, including the location, possible migration, and occurrence of mafic magmatism associated with the A^3 triple junction.

We suggest that initiation of the triple junction at a position near the village of Kahramanmaraş began around 5 Ma, and it subsequently migrated to the southwest to its current position near the Amik Basin (Fig. 13). This interpretation is consistent with an overall southwesterly shift in the locus of deformation along the East Anatolian fault zone toward areas containing young and shallow basins. This interpretation also implies that plate segmentation within the lithosphere may not correspond to exposed crustal sequences representing former plate positions. For example, the trend of pronounced seismicity west of Kahramanmaraş (e.g., Duman and Emre, 2013) could represent either a zone of previous weakness or one of incipient faulting. Coincident with the A^3 triple junction migration, there was linked migration of the Africa-Anatolia plate margin and a jump of the Cyprean trench to its current southerly position (Fig. 13). Geologic evidence for such a model

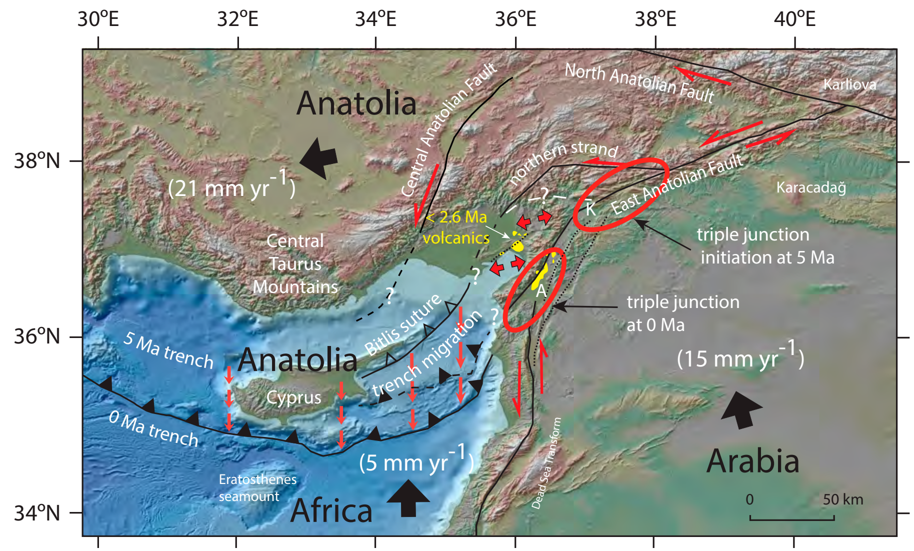

Figure 13. Digital elevation map with major tectonic features of the East Anatolian fault zone system labeled and illustrating the approximate position of the Anatolia-Arabia-Africa (A^3) triple junction at 5 Ma near Kahramanmaraş (K) and at 0 Ma near the Amik Basin (A). Some faults are dotted for clarity, and others are dashed where inferred. The triple junction migration was synchronous with a southward repositioning of the Africa-Anatolia plate boundary to the south of Cyprus by 5 Ma. Note the restriction of Quaternary (<2.6 Ma) basalts (yellow) to a region of transtension between the triple junction positions (block arrows), and the two strands of the East Anatolian fault zone. Active extrusion of the Anatolia microplate at 5 Ma transformed the triple junction from a boundary along a convergent zone (Bitlis suture) to one migrating along a transform plate boundary influenced by the extruding plate. The plate-boundary reorganization was coincident with a southward jump in the position of the active trench (red arrows) to one defining the current Anatolia-Africa plate boundary. This trench jump is consistent with Pliocene uplift occurring within Cyprus (e.g., McCallum and Robertson, 1995; Kinnaird et al., 2011). The current position of the A^3 triple junction is consistent with deformation transitioning from the northern strand to the main southern strand of the East Anatolian fault zone. Geologic conditions favor continued migration of the A^3 triple junction in conjunction with rollback of the African plate along the Dead Sea transform fault, with future uplift of the Eratosthenes seamount as trench migration progresses.

within the Adana Basin includes the abrupt termination of late Miocene compressional (Bitlis suture) sedimentation features and the establishment of Pliocene and younger high-angle translational faults and extensional/transtensional basins (e.g., Burton-Ferguson et al., 2005). Such a model is also consistent with a period of major Pliocene surface uplift within Cyprus (e.g., McCallum and Robertson, 1995; Kinnaird et al., 2011; Schildgen et al., 2012). This younger than 5 Ma southward trench migration could have been related to slab detachment through ongoing horizontal tearing and segmentation within the Cyprean slab (e.g., Portner et al., 2018). Cyprean slab detachment is thought to be a major factor driving the post–8 Ma surface uplift of the central Taurus Mountains (e.g., Schildgen et al., 2014; Meijers et al., 2018; 2020). The same or similar tectonic forces responsible for the partial uplift of Cyprus will ultimately lead to future uplift of the Eratosthenes Seamount.

Plate-boundary reorganization from 5 Ma to present would have modified the regional deformation and the state of stress and promoted the tapping of sublithospheric melt along lithospheric-scale shear zones associated with extension/transtension (Fig. 13). Cyprean slab rollback and the southwesterly migration of the A^3 triple junction are not only consistent with establishment of the southern strand of the East Anatolian fault zone as a primary plate boundary, but they are also consistent with the spatial distribution of mafic volcanism. The spatially restricted occurrence of Quaternary basalts between the current and former positions of the A^3 triple junction suggests that the migration of the triple junction, in this case associated with trench migration (or jump), triggered deeply sourced volcanism. Tectonic conditions favor continued migration of the A^3 triple junction along the Dead Sea transform fault as rollback of the Cyprean slab proceeds and the Anatolia-Africa-Arabia plate boundaries continue to evolve.

SUMMARY

From 5 Ma to the present day, the intersecting Africa-Anatolia-Arabia plate boundaries have adjusted to the tectonic escape of the Anatolia plate and rollback of the Cyprean slab. This process led to the initiation and subsequent migration of the A^3 triple junction and development of major transform faults, broad zones of transtension, and localized volcanism. Quaternary basalts and basanites within the Toprakkale and Karasu volcanic fields are a consequence of these plate adjustments within this dynamic setting. Radiogenic isotope data (Sr, Nd, Hf, Pb) indicate that the basanites were derived from the most-depleted mantle source, but all samples indicate derivation from a garnet-bearing OIB-like source. The seismically imaged depth (~60 km) of the lithosphere-asthenosphere boundary directly beneath the northwestern margin of the Arabia plate is consistent with the inferred depth of melting of all basalts. Basanites from the Toprakkale volcanic field, however, indicate a deeper (~90 km) melting source, interpreted to have originated from either partial melting of the adjacent Cyprean slab lithospheric mantle, or melting of detached fragments of Arabian lithospheric mantle that foundered within the asthenosphere. A mafic lava with a $^{40}Ar/^{39}Ar$ plateau age of 2.63 ± 0.17 Ma from the Karasu volcanic field represents the earliest stage of volcanism associated with the developing A^3 triple junction. This time period is also consistent with more regional data from the northwestern margin of the Arabia plate supporting an increase in magmatic activity from 2 Ma. Episodic eruption of lavas in the last 2.6 m.y. along discrete segments of the East Anatolian fault zone clearly demonstrates that volcanism is being localized along and/or between transform faults related to the A^3 triple junction. The Dead Sea fault zone and East Anatolian fault zone plate boundaries are high-angle shear zones that likely penetrate into the lithospheric mantle, providing the "leaky" conduits along which melts infiltrate to reach the surface, analogous to the restricted volcanism along transform faults occurring in oceanic crust. The spatially restricted distribution of basalts proximal to the A^3 triple junction indicates the potential for a causal relationship, because they occur within a zone of transtension near the triple junction and are not more widespread along the length of the East Anatolian fault zone. Tectonic conditions favor continued migration of the A^3 triple junction as this motion is directly tied to the ongoing tectonic escape of Anatolia and rollback of the Cyprean slab.

ACKNOWLEDGMENTS

This study was partially funded with collaborative support of the National Science Foundation (NSF) as part of the Continental Dynamics program (NSF EAR-1109762 and 1109826). We thank Nuretdin Kaymakçı for fruitful scientific discussions and introducing some of us to the field area. We also thank Gilles Brocard for maps and scientific discussions. Critical reviews and suggestions for improving the manuscript by Samuele Agostini, Richard Arculus, and David Moecher are gratefully acknowledged. Any use of trade, product, or firm names is for descriptive purposes only and does not imply endorsement by the U.S. government.

REFERENCES CITED

Abgarmi, B., Delph, J.R., Ozacar, A.A., Beck, S.L., Zandt, G., Sandvol, E., Turkelli, N., and Biryol, C.B., 2017, Structure of the crust and African slab beneath the central Anatolian plateau from receiver functions: New insights on isostatic compensation and slab dynamics: Geosphere, v. 13, no. 6, p. 1774–1787, https://doi.org/10.1130/GES01509.1.

Aksu, A.E., Calon, T.J., Hall, J., and Yaşar, D., 2005, Origin and evolution of the Neogene İskenderun Basin, northeastern Mediterranean Sea: Marine Geology, v. 221, no. 1–4, p. 161–187, https://doi.org/10.1016/j.margeo.2005.03.010.

Aldanmaz, E., Köprübaşı, N., Gürer, Ö.F., Kaymakçı, N., and Gourgaud, A., 2006, Geochemical constraints on the Cenozoic, OIB-type alkaline volcanic rocks of NW Turkey: Implications for mantle sources and melting processes: Lithos, v. 86, p. 50–76, https://doi.org/10.1016/j.lithos.2005.04.003.

Aldanmaz, E., Pickard, M., Meisel, T., Altunkaynak, Ş., Sayıt, K., Şen, P., Hannan, B., and Furman, T., 2015, Source components and magmatic processes in the genesis of Miocene to Quaternary lavas in western Turkey: Constraints from HSE distribution and Hf-Pb-Os isotopes: Contributions to Mineralogy and Petrology, v. 170, https://doi.org/10.1007/s00410-015-1176-x.

Alıcı, P., Temel, A., Gourgaud, A., Vidal, P., and Gündogdu, M.N., 2001, Quaternary tholeiitic to alkaline volcanism in the Karasu Valley, Dead Sea rift zone, southeast Turkey: Sr-Nd-Pb-O isotopic and trace-element approaches to crust-mantle interaction: International Geology Review, v. 43, no. 2, p. 120–138, https://doi.org/10.1080/00206810109465004.

Angus, D.A., Wilson, D.C., Sandvol, E., and Ni, J.F., 2006, Lithospheric structure of the Arabian and Eurasian collision zone in eastern Turkey from S-wave receiver functions: Geophysical Journal International, v. 166, no. 3, p. 1335–1346, https://doi.org/10.1111/j.1365-246X.2006.03070.x.

Arger, J., Mitchell, J., and Westaway, R.W.C., 2000, Neogene and Quaternary volcanism of southeastern Turkey, *in* Bozkurt, E., Winchester, J.A., and Piper, J.D.A., eds., Tectonics and Magmatism in Turkey and the Surrounding Area: Geological Society [London] Special Publication 173, p. 459–487, https://doi.org/10.1144/GSL.SP.2000.173.01.22.

Arpat, A.E., and Şaroğlu, F., 1972, Doğu Anadolu Fayı ile ilgili bazı gözlem ve düşünceler: Bulletin of the Mineral Research and Exploration, v. 73, p. 1–9 [in Turkish].
Bağcı, U., Alpaslan, M., Frei, R., Kurt, M.A., and Temel, A., 2011, Different degrees of partial melting of the enriched mantle source for Plio-Quaternary basic volcanism, Toprakkale (Osmaniye) region, southern Turkey: Turkish Journal of Earth Sciences, v. 20, p. 115–135.
Becker, T.W., and Faccenna, C., 2011, Mantle conveyor beneath the Tethyan collisional belt: Earth and Planetary Science Letters, v. 310, p. 453–461, https://doi.org/10.1016/j.epsl.2011.08.021.
Bertrand, H., Chazot, G., Blichert-Toft, J., and Thoral, S., 2003, Implications of widespread high-µ volcanism on the Arabian plate for Afar mantle plume and lithosphere composition: Chemical Geology, v. 198, p. 47–61, https://doi.org/10.1016/S0009-2541(02)00418-7.
Birck, J.L., and Allégre, C.J., 1978, Chronology and chemical history of the parent body of basaltic achondrites studied by ^{87}Rb-^{87}Sr method: Earth and Planetary Science Letters, v. 39, p. 37–51, https://doi.org/10.1016/0012-821X(78)90139-5.
Biryol, C.B., Beck, S.L., Zandt, G., and Özacar, A.A., 2011, Segmented African lithosphere beneath the Anatolian region inferred from teleseismic P-wave tomography: Geophysical Journal International, v. 184, p. 1037–1057, https://doi.org/10.1111/j.1365-246X.2010.04910.x.
Blichert-Toft, J., Chauvel, C., and Albarède, F., 1997, Separation of Hf and Lu for high-precision isotope analysis of rock samples by magnetic sector–multiple collector ICP-MS: Contributions to Mineralogy and Petrology, v. 127, no. 3, p. 248–260, https://doi.org/10.1007/s004100050278.
Bosworth, W., and Stockli, D., 2016, Early magmatism in the greater Red Sea rift: Timing and significance: Canadian Journal of Earth Sciences, v. 53, p. 1158–1176, https://doi.org/10.1139/cjes-2016-0019.
Burton-Ferguson, R., Aksu, A.E., Calon, T.J., and Hall, J., 2005, Seismic stratigraphy and structural evolution of the Adana Basin, eastern Mediterranean: Marine Geology, v. 221, p. 189–222, https://doi.org/10.1016/j.margeo.2005.03.009.
Çapan, U.Z., Vidal, P.H., and Cantagrel, J.M., 1987, K-Ar, Nd, Sr and Pb isotopic study of Quaternary volcanism in Karasu valley (Hatay), N-end of Dead Sea rift zone in SE Turkey: Yerbilimleri, v. 14, p. 165–178.
Cavalié, O., and Jónsson, S., 2014, Block-like plate movements in eastern Anatolia observed by InSar: Geophysical Research Letters, v. 41, p. 26–31, https://doi.org/10.1002/2013GL058170.
Cesare, B., Rubatto, D., and Gómez-Pugnaire, M.T., 2009, Do extrusion ages reflect magma generation processes at depth? An example from the Neogene Volcanic Province of SE Spain: Contributions to Mineralogy and Petrology, v. 157, p. 267–279, https://doi.org/10.1007/s00410-008-0333-x.
Chorowicz, J., Dhont, D., Ammar, O., Rukieh, M., and Bilal, A., 2005, Tectonics of the Pliocene Homs basalts (Syria) and implications for the Dead Sea fault zone activity: Journal of the Geological Society [London], v. 162, p. 259–271, https://doi.org/10.1144/0016-764904-037.
Çoban, H., 2007, Basalt magma genesis and fractionation in collision- and extension-related provinces: A comparison between eastern, central and western Anatolia: Earth-Science Reviews, v. 80, p. 219–238, https://doi.org/10.1016/j.earscirev.2006.08.006.
Dalrymple, G.B., Alexander, E.C., Lanphere, M.A., and Kraker, G.P., 1981, Irradiation of Samples for ^{40}Ar/^{39}Ar Dating Using the Geological Survey TRIGA Reactor: U.S. Geological Survey Professional Paper 1176, 29 p., https://doi.org/10.3133/pp1176.
Davies, D.R., and Rawlinson, N., 2014, On the origin of recent intraplate volcanism in Australia: Geology, v. 42, p. 1031–1034, https://doi.org/10.1130/G36093.1.
Delph, J.R., Abgarmi, B., Ward, K.M., Beck, S.L., Özacar, A.A., Zandt, G., Sandvol, E., Türkelli, N., and Kalafat, D., 2017, The effects of subduction termination on the continental lithosphere: Linking volcanism, deformation, surface uplift, and slab tearing in central Anatolia: Geosphere, v. 13, p. 1788–1805, https://doi.org/10.1130/GES01478.1.
Dewey, J.F., and Şengör, A.M.C., 1979, Aegean and surrounding regions: Complex multiplate and continuum tectonics in a convergent zone: Geological Society of America Bulletin, v. 90, p. 84–92, https://doi.org/10.1130/0016-7606(1979)90<84:AASRCM>2.0.CO;2.
Dewey, J.F., Hempton, M.R., Kidd, W.S.F., Şaroglu, F., and Şengör, A.M.C., 1986, Shortening of continental lithosphere: The neotectonics of Eastern Anatolia—A young collision zone, *in* Coward, M.P., and Ries, A.C., eds., Collision Tectonics: Geological Society [London] Special Publication 19, p. 1–36, https://doi.org/10.1144/GSL.SP.1986.019.01.01.
Duman, T.Y., and Emre, O., 2013, The East Anatolian fault: Geometry, segmentation and jog characteristics, *in* Robertson, A.H.F., Parlak, O., and Ünlügenc, U.C., eds., Geological Development of Anatolia and the Easternmost Mediterranean Region: Geological Society [London] Special Publication 372, p. 495–529, https://doi.org/10.1144/SP372.14.
Eisele, J., Abouchami, W., Galer, S.J., and Hofmann, A.W., 2003, The 320 kyr Pb isotope evolution of Mauna Kea lavas recorded in the HSDP-2 drill core: Geochemistry Geophysics Geosystems, v. 4, no. 5, 8710, https://doi.org/10.1029/2002GC000339.
Ekici, T., and Macpherson, C., 2019, Convergence-aligned foreland magmatism in the Arabia-Anatolia collision: Geochronological evidence from the Karacadağ volcanic complex, south-east Turkey: Turkish Journal of Earth Sciences, v. 28, p. 719–733, https://doi.org/10.3906/yer-1902-25.
Ekici, T., Macpherson, C.G., Otlu, N., and Fontignie, D., 2014, Foreland magmatism during the Arabia-Eurasia collision: Pliocene–Quaternary activity of the Karacadağ volcanic complex, SW Turkey: Journal of Petrology, v. 55, no. 9, p. 1753–1777, https://doi.org/10.1093/petrology/egu040.
Ergin, M., Aktar, M., and Eyidoğan, H., 2004, Present-day seismicity and seismotectonics of the Cilician Basin: Eastern Mediterranean region of Turkey: Bulletin of the Seismological Society of America, v. 94, no. 3, p. 930–939, https://doi.org/10.1785/0120020153.
Ferrari, L., 2004, Slab detachment control on mafic volcanic pulse and mantle heterogeneity in central Mexico: Geology, v. 32, p. 77–80, https://doi.org/10.1130/G19887.1.
Fletcher, M., Wyman, D.A., and Zahirovic, S., 2020, Mantle plumes, triple junctions and transforms: A reinterpretation of Pacific Cretaceous–Tertiary LIPs and the Laramide connection: Geoscience Frontiers, v. 11, p. 1133–1144, https://doi.org/10.1016/j.gsf.2019.09.003.
Furlong, K.P., and Schwartz, S.Y., 2004, Influence of the Mendocino Triple Junction on the Tectonics of Coastal California: Annual Review of Earth and Planetary Sciences, v. 32, p. 403–433, https://doi.org/10.1146/annurev.earth.32.101802.120252.
Gürsoy, H., Tatar, O., Piper, J.D.A., Heimann, A., and Mesci, L., 2003, Neotectonic deformation linking the East Anatolian and the Karatas-Osmaniye intracontinental transform fault zones in the Gulf of İskenderun, southern Turkey, deduced from paleomagnetic study of the Ceyhan-Osmaniye volcanics: Tectonics, v. 22, 1067, https://doi.org/10.1029/2003TC001524.
Hanan, B.B., and Graham, D.W., 1996, Lead and helium isotope evidence from oceanic basalts for a common deep source of mantle plumes: Science, v. 272, no. 5264, p. 991–995, https://doi.org/10.1126/science.272.5264.991.
Hansen, S.E., Rodgers, A.J., Schwartz, S.Y., and Al-Amri, A.M.S., 2007, Imaging ruptured lithosphere beneath the Red Sea and Arabian Peninsula: Earth and Planetary Science Letters, v. 259, p. 256–265, https://doi.org/10.1016/j.epsl.2007.04.035.
Hart, S.R., 1984, A large-scale isotope anomaly in the Southern Hemisphere mantle. Nature, v. 309, p. 753–757, https://doi.org/10.1038/309753a0.
Hékinian, R., Bideau, D., Hébert, R., and Niu, Y., 1995, Magmatism in the Garrett transform fault (East Pacific Rise near 13°27′S): Journal of Geophysical Research, v. 100, no. B7, p. 10163–10185, https://doi.org/10.1029/94JB02125.
Hempton, M., 1987, Constraints on Arabian plate motion and extensional history of the Red Sea: Tectonics, v. 6, p. 687–705, https://doi.org/10.1029/TC006i006p00687.
Holzer, T.L., 2000, Implications for Earthquake Risk Reduction in the United States from the Kocaeli, Turkey, Earthquake of August 17, 1999: U.S. Geological Survey Circular 1193, 64 p.
Imprescia, P., Pondrelli, S., Vannucci, G., and Gresta, S., 2012, Regional centroid moment tensor solutions in Cyprus from 1977 to the present and seismotectonic implications: Journal of Seismology, v. 16, p. 147–167, https://doi.org/10.1007/s10950-011-9254-7.
Irvine, T.N., and Baragar, W.R.A., 1971, A guide to the chemical classification of the common volcanic rocks: Canadian Journal of Earth Sciences, v. 8, p. 523–548, https://doi.org/10.1139/e71-055.
Italiano, F., Yuce, G., Di Bella, M., Rojay, B., Sabatino, G., Tripodo, A., Martelli, M., Rizzo, A.L., and Misseri, M., 2017, Noble gases and rock geochemistry of alkaline intraplate volcanics from the Amik and Ceyhan-Osmaniye areas, SE Turkey: Chemical Geology, v. 469, p. 34–46, https://doi.org/10.1016/j.chemgeo.2017.04.003.
Kaislaniemi, L., and van Hunen, J., 2014, Dynamics of lithospheric thinning and mantle melting by edge-driven convection: Application to Moroccan Atlas mountains: Geochemistry Geophysics Geosystems, v. 15, p. 3175–3189, https://doi.org/10.1002/2014GC005414.
Karakas, O., Degruyter, W., Bachmann, O., and Dufek, J., 2017, Lifetime and size of shallow magma bodies controlled by crustal-scale magmatism: Nature Geoscience, v. 10, no. 6, p. 446–450, https://doi.org/10.1038/ngeo2959.
Karig, D.E., and Kozlu, H., 1990, Late Paleogene evolution of the triple junction region near Maraş, south-central Turkey: Journal of the Geological Society [London], v. 147, p. 1023–1034, https://doi.org/10.1144/gsjgs.147.6.1023.
Kavak, K.S., Tatar, O., Piper, J., Kocbulut, F., and Mesci, B.L., 2009, Determination of neotectonic features of the Karasu Basin (SE Turkey) and their relationship with Quaternary volcanic

activity using Landsat ETM+ imagery: International Journal of Remote Sensing, v. 30, no. 17, p. 4507–4524, https://doi.org/10.1080/01431160802578004.
Kelley, K.A., and Cottrell, E., 2009, Water and the oxidation state of subduction zone magmas: Science, v. 325, no. 5940, p. 605–607, https://doi.org/10.1126/science.1174156.
Keshav, S., and Gudfinnsson, G.H., 2004, Silica-poor, mafic alkaline lavas from ocean islands and continents: Petrogenetic constraints from major elements: Journal of Earth System Science, v. 113, p. 723–736, https://doi.org/10.1007/BF02704032.
Keskin, M., Chugaev, A.V., Lebedev, V.A., Sharkov, E.V., Oyan, V., and Kavak, O., 2012, The geochronology and origin of mantle sources for late Cenozoic intraplate volcanism in the frontal part of the Arabian plate in the Karacadağ neovolcanic area of Turkey. Part 1. The results of isotope-geochronological studies: Journal of Volcanology and Seismology, v. 6, p. 352–360, https://doi.org/10.1134/S0742046312060036.
Kinnaird, T., Robertson, A., and Morris, A., 2011, Timing of uplift of the Troodos Massif (Cyprus) constrained by sedimentary and magnetic polarity evidence: Journal of the Geological Society [London], v. 168, p. 457–470, https://doi.org/10.1144/0016-76492009-150.
Klaver, M., Djuly, T., de Graaf, S., Sakes, A., Wijbrans, J., Davies, G., and Vroon, P., 2015, Temporal and spatial variations in provenance of eastern Mediterranean Sea sediments: Implications for Aegean and Aeolian arc volcanism: Geochimica et Cosmochimica Acta, v. 153, p. 149–168, https://doi.org/10.1016/j.gca.2015.01.007.
Krienitz, M.S., Haase, K.M., Mezger, K., Eckardt, V., and Shaikh-Mashail, M.A., 2006, Magma genesis and crustal contamination of continental intraplate lavas in northwestern Syria: Contributions to Mineralogy and Petrology, v. 151, no. 6, p. 698–716, https://doi.org/10.1007/s00410-006-0088-1.
Kuiper, K.F., Deino, A., Hilgen, F.J., Krijgsman, W., Renne, P.R., and Wijbrans, J.R., 2008, Synchronizing rock clocks of Earth history: Science, v. 320, no. 5875, p. 500–504, https://doi.org/10.1126/science.1154339.
Le Maitre, R.W., Bateman, P., Dudek, A., Keller, J., Lameyre, J., Le Bas, M.J., Sabine, P.A., Schmid, R., Sorensen, H., Streckeisen, A., and Woolley, A.R., 1989, A Classification of Igneous Rocks and Glossary of Terms: Recommendations of the IUGS Subcommission on the Systematics of Igneous Rocks: London, Blackwell Scientific Publications, 193 p. and wall chart.
Lee, C.-T., Luffi, P., Plank, T., Dalton, H., and Leeman, W.P., 2009, Constraints on the depths and temperatures of basaltic magma generation on Earth and other terrestrial planets using new thermobarometers for mafic magmas: Earth and Planetary Science Letters, v. 279, no. 1–2, p. 20–33, https://doi.org/10.1016/j.epsl.2008.12.020.
Lee, J.Y., Marti, K., Severinghaus, J.P., Kawamura, K., Yoo, H.S., Lee, J.B., and Kim, J.S., 2006, A redetermination of the isotopic abundances of atmospheric Ar: Geochimica et Cosmochimica Acta, v. 70, no. 17, p. 4507–4512, https://doi.org/10.1016/j.gca.2006.06.1563.
Levander, A., Bezada, M.J., Niu, F., Humphreys, E.D., Palomeras, I., Thurner, S.M., Masy, J., Schmitz, M., Gallart, J., Carbonell, R., and Miller, M.S., 2014, Subduction-driven recycling of continental margin lithosphere: Nature, v. 515, p. 253–256, https://doi.org/10.1038/nature13878.
Ludwig, K.R., 1980, Calculation of uncertainties of U-Pb data: Earth and Planetary Science Letters, v. 46, p. 212–220, https://doi.org/10.1016/0012-821X(80)90007-2.
Ludwig, K.R., 1985, PBDAT200: A Computer Program for Processing Raw Pb-U-Th Isotope Data: U.S. Geological Survey Open-File Report 85–547, 54 p.
Lugmair, G.W., Scheinin, N.B., and Marti, K., 1975, Sm-Nd age and history of *Apollo 17* basalt 75075: Evidence for early differentiation of the lunar exterior, *in* Proceedings of the 6th Lunar and Planetary Science Conference, Volume 2: Houston, Texas, Lunar and Planetary Institute, p. 1419–1429.
Lustrino, M., Keskin, M., Mattioli, M., Lebedev, V.A., Chugaev, A., Sharkov, E., and Kavak, O., 2010, Early activity of the largest Cenozoic shield volcano in the circum-Mediterranean area: Mt. Karacadağ, SE Turkey: European Journal of Mineralogy, v. 22, no. 3, p. 343–362, https://doi.org/10.1127/0935-1221/2010/0022-2024.
Ma, G.S.K., Malpas, J., Xenophontos, C., and Chan, G.H.N., 2011, Petrogenesis of latest Miocene–Quaternary continental intraplate volcanism along the northern Dead Sea fault system (Al Ghab–Homs volcanic field), western Syria: Evidence for lithosphere-asthenosphere interaction: Journal of Petrology, v. 52, no. 2, p. 401–430, https://doi.org/10.1093/petrology/egq085.
Mahmoud, Y., Masson, F., Meghraoui, M., Cakir, Z., Alchalbi, A., Yavasoglu, H., Yönlü, O., Daoud, M., Ergintav, S., and Inan, S., 2013, Kinematic study at the junction of the East Anatolian fault and the Dead Sea fault from GPS measurements: Journal of Geodynamics, v. 67, p. 30–39, https://doi.org/10.1016/j.jog.2012.05.006.
McCallum, J.E., and Robertson, A.H.F., 1995, Sedimentology of two fan-delta systems in the Pliocene–Pleistocene of the Mesaoria Basin, Cyprus: Sedimentary Geology, v. 98, no. 1–4, p. 215–244, https://doi.org/10.1016/0037-0738(95)00034-6.
McDonough, W.F., and Sun, S.S., 1995, The composition of the Earth: Chemical Geology, v. 120, no. 3–4, p. 223–253, https://doi.org/10.1016/0009-2541(94)00140-4.
McKenzie, D.P., 1976, The East Anatolian fault; a major structure in eastern Turkey: Earth and Planetary Science Letters, v. 29, p. 189–193, https://doi.org/10.1016/0012-821X(76)90038-8.
McNab, F., Ball, P.W., Hoggard, M.J., and White, N.J., 2018, Neogene uplift and magmatism of Anatolia: Insights from drainage analysis and basaltic geochemistry: Geochemistry Geophysics Geosystems, v. 19, p. 175–213, https://doi.org/10.1002/2017GC007251.
Meijers, M.J.M., Brocard, G.Y., Cosca, M.A., Lüdecke, T., Teyssier, C., Whitney, D.L., and Mulch, A., 2018, Rapid late Miocene surface uplift of the Central Anatolian Plateau margin: Earth and Planetary Science Letters, v. 497, p. 29–41, https://doi.org/10.1016/j.epsl.2018.05.040.
Meijers, M.J.M., Brocard, G.Y., Whitney, D.L., and Mulch, A., 2020, Paleoenvironmental conditions and drainage evolution of the central Anatolian lake system (Turkey) during late Miocene to Pliocene surface uplift: Geosphere, v. 16, no. 2, p. 490–509, https://doi.org/10.1130/GES02135.1.
Min, K., Mundil, R., Renne, P.R., and Ludwig, K.R., 2000, A test for systematic errors in $^{40}Ar/^{39}Ar$ geochronology through comparison with U/Pb analysis of a 1.1-Ga rhyolite: Geochimica et Cosmochimica Acta, v. 64, no. 1, p. 73–98, https://doi.org/10.1016/S0016-7037(99)00204-5.
Muehlberger, W.R., and Gordon, M.B., 1987, Observations on the complexity of the East Anatolian fault, Turkey: Journal of Structural Geology, v. 9, p. 899–903, https://doi.org/10.1016/0191-8141(87)90091-5.
Nikogosian, I.K., Bracco Gartner, A.J.J., van Bergen, M.J., Mason, P.R.D., and van Hinsbergen, D.J.J., 2018, Mantle sources of recent Anatolian intraplate magmatism: A regional plume or local tectonic origin?: Tectonics, v. 37, no. 12, p. 4535–4566, https://doi.org/10.1029/2018TC005219.
O'Neill, H.S.C., 2016, The smoothness and shapes of chondrite-normalized rare earth element patterns in basalts: Journal of Petrology, v. 57, p. 1463–1508, https://doi.org/10.1093/petrology/egw047.
Over, S., Kavak, Ş., Bellier, O., and Özden, S., 2004, Is the Amik Basin (SE Turkey) a triple-junction area? Analyses of SPOT XX imagery and seismicity: International Journal of Remote Sensing, v. 25, p. 3857–3872, https://doi.org/10.1080/01431160310001654437.
Oyan, V., 2018, Petrogenesis of the Quaternary mafic alkaline volcanism along the African-Anatolian plates boundary in Turunçlu-Delihalil (Osmaniye) region in southern Turkey: Lithos, v. 314–315, p. 630–645, https://doi.org/10.1016/j.lithos.2018.06.008.
Parlak, O., Kozlu, H., Demirkol, C., and Delaloye, M., 1997, Intracontinental Plio-Quaternary volcanism along the African-Anatolian plate boundary, southern Turkey: Ofioliti, v. 22, p. 111–117.
Parlak, O., Kop, A., Ünlügenç, U.C., and Demirkol, C., 1998, Geochronology and geochemistry of basaltic rocks in the Karasu graben around Kirikhan (Hatay), S. Turkey: Turkish Journal of Earth Sciences, v. 7, p. 53–61.
Parlak, O., Delaloye, M., Kozlu, H., and Fontignie, D., 2000, Trace element and Sr-Nd isotope geochemistry of the alkali basalts observed along the Yumurtalık fault (Adana) in southern Turkey: Yerbilimleri, v. 22, p. 137–148.
Pearce, J.A., Bender, J.F., De Long, S.E., Kidd, W.S.F., Low, P.J., Güner, Y., Şaroglu, F., Yılmaz, Y., Moorbath, S., and Mitchell, J.G., 1990, Genesis of collision volcanism in eastern Anatolia, Turkey: Journal of Volcanology and Geothermal Research, v. 44, no. 1–2, p. 189–229, https://doi.org/10.1016/0377-0273(90)90018-B.
Perfit, M.R., Fornari, D.J., Ridley, W.I., Kirk, P.D., Casey, J., Kastens, K.A., Reynolds, J.R., Edwards, M., Desonie, D., Shuster, R., and Paradis, S., 1996, Recent volcanism in the Siqueiros transform fault: Picritic basalts and implications for MORB magma genesis: Earth and Planetary Science Letters, v. 141, p. 91–108, https://doi.org/10.1016/0012-821X(96)00052-0.
Perinçek, D., and Çemen, İ., 1990, The structural relationship between the East Anatolian and Dead Sea fault zones in southeastern Turkey: Tectonophysics, v. 172, p. 331–340, https://doi.org/10.1016/0040-1951(90)90039-B.
Pik, R., Deniel, C., Coulon, C., Yirgu, G., and Marty, B., 1999, Isotopic and trace element signatures of Ethiopian flood basalts: Evidence for plume-lithosphere interactions: Geochimica et Cosmochimica Acta, v. 63, no. 15, p. 2263–2279, https://doi.org/10.1016/S0016-7037(99)00141-6.
Pilet, S., Baker, M.B., and Stolper, E.M., 2008, Metasomatized lithosphere and the origin of alkaline lavas: Science, v. 320, p. 916–919, https://doi.org/10.1126/science.1156563.
Plank, T., and Forsyth, D.W., 2016, Thermal structure and melting conditions in the mantle beneath the Basin and Range Province from seismology and petrology: Geochemistry Geophysics Geosystems, v. 17, p. 1312–1338, https://doi.org/10.1002/2015GC006205.

Polat, A., Kerrich, R., and Casey, J.F., 1997, Geochemistry of Quaternary basalts erupted along the East Anatolian and Dead Sea fault zones of southern Turkey: Implications for mantle sources: Lithos, v. 40, p. 55–68, https://doi.org/10.1016/S0024-4937(96)00027-8.

Portner, D.E., Delph, J.R., Biryol, C.B., Beck, S.L., Zandt, G., Ozacar, A.A., Sandvol, E., and Turkelli, N., 2018, Subduction termination through progressive slab deformation across eastern Mediterranean subduction zones from updated P-wave tomography beneath Anatolia: Geosphere, v. 14, p. 907–925, https://doi.org/10.1130/GES01617.1.

Premo, W.R., and Loucks, R.R., 2000, Age and Pb-Sr-Nd isotopic systematics of plutonic rocks from the Green Mountain magmatic arc, southeastern Wyoming: Isotopic characterization of a Paleoproterozoic island arc system: Rocky Mountain Geology, v. 35, no. 1, p. 51–70, https://doi.org/10.2113/35.1.51.

Premo, W.R., and Taylor, C.D., 2010, Radiogenic isotopic characterization and petrogenesis of host rocks to the Greens Creek deposit (Chapter 12), *in* Taylor, C.D., and Johnson, C.A., eds., Geology, Geochemistry, and Genesis of the Greens Creek Massive Sulfide Deposit, Admiralty Island, Southeastern Alaska: U.S. Geological Survey Professional Paper 1763, p. 335–365.

Reid, M.R., Bouchet, R.A., Blichert-Toft, J., Levander, A., Liu, K., Miller, M.S., and Ramos, F.C., 2012, Melting under the Colorado Plateau, USA: Geology, v. 40, no. 5, p. 387–390, https://doi.org/10.1130/G32619.1.

Reid, M.R., Schleiffarth, W.K., Cosca, M.A., Delph, J.R., Blichert-Toft, J., and Cooper, K.M., 2017, Shallow melting of MORB-like mantle under hot continental lithosphere, central Anatolia: Geochemistry Geophysics Geosystems, v. 18, p. 1866–1888, https://doi.org/10.1002/2016GC006772.

Reid, M.R., Delph, J.R., Cosca, M.A., Schleiffarth, W.K., and Gençalioğlu Kuşcu, G., 2019, Melt equilibration depths as sensors of lithospheric thickness during Eurasia-Arabia collision and the uplift of the Anatolian Plateau: Geology, v. 47, no. 10, p. 943–947, https://doi.org/10.1130/G46420.1.

Reilinger, R., McClusky, S., Vernant, P., Lawrence, S., Ergintav, S., Cakmak, R., Ozener, H., Kadirov, F., Guliev, I., Stepanyan, R., and Nadariya, M., 2006, GPS constraints on continental deformation in the Africa-Arabia-Eurasia continental collision zone and implications for the dynamics of plate interactions: Journal of Geophysical Research, v. 111, B05411, https://doi.org/10.1029/2005JB004051.

Rojay, B., Heimann, A., and Toprak, V., 2001, The transition zone between the Dead Sea transform and the East Anatolian fault zone: Geodinamica Acta, v. 14, p. 197–212, https://doi.org/10.1080/09853111.2001.11432444.

Schildgen, T., Cosentino, D., Bookhagen, B., Niedermann, S., Yıldırım, C., Echtler, H., Wittmann, H., and Strecker, M., 2012, Multi-phased uplift of the southern margin of the Central Anatolian Plateau, Turkey: A record of tectonic and upper mantle processes: Earth and Planetary Sciences, v. 317–318, p. 85–95, https://doi.org/10.1016/j.epsl.2011.12.003.

Schildgen, T., Yıldırım, C., Cosentino, D., and Strecker, M.R., 2014, Linking slab break-off, Hellenic trench retreat, and uplift of the Central and Eastern Anatolian plateaus: Earth-Science Reviews, v. 128, p. 147–168, https://doi.org/10.1016/j.earscirev.2013.11.006.

Şen, P.A., Temel, A., and Gourgaud, A., 2004, Petrogenetic modelling of Quaternary post-collisional volcanism: A case study of central and eastern Anatolia: Geological Magazine, v. 141, no. 1, p. 81–98, https://doi.org/10.1017/S0016756803008550.

Şengör, A.M.C., and Yılmaz, Y., 1981, Tethyan evolution of Turkey: A plate tectonic approach: Tectonophysics, v. 75, p. 181–241, https://doi.org/10.1016/0040-1951(81)90275-4.

Şengör, A.M.C., Görür, N., and Şaroglu, F., 1985, Strike-slip faulting and related basin formation in zones of tectonic escape: Turkey as a case study, *in* Biddle, K.T., and Christie-Blick, N., eds., Strike-Slip Deformation, Basin Formation, and Sedimentation: Society of Economic Paleontologists and Mineralogists (SEPM) Special Publication 37, p. 227–264, https://doi.org/10.2110/pec.85.37.0227.

Seyrek, A., Demir, T., Pringle, M.S., Yurtmen, S., Westaway, R.W.C., Beck, A., and Rowbotham, G., 2007, Kinematics of the Amanos fault, southern Turkey, from Ar/Ar dating of offset Pleistocene basalt flows: Transpression between the African and Arabian plates, *in* Cunningham, W.D., and Mann, P., eds., Tectonics of Strike-Slip Restraining and Releasing Bends: Geological Society [London] Special Publication 290, p. 255–284, https://doi.org/10.1144/SP290.9.

Seyrek, A., Demir, T., Pringle, M., Yurtmen, S., Westaway, R., Bridgland, D., Beck, A., and Rowbotham, G., 2008, Late Cenozoic uplift of the Amanos Mountains and incision of the Middle Ceyhan river gorge, southern Turkey; Ar-Ar dating of the Düziçi basalt: Geomorphology, v. 97, p. 321–355, https://doi.org/10.1016/j.geomorph.2007.08.014.

Shaw, J.E., Baker, J.A., Menzies, M.A., Thirlwall, M.F., and Ibrahim, K.M., 2003, Petrogenesis of the largest intraplate volcanic field on the Arabian plate (Jordan): A mixed lithosphere-asthenosphere source activated by lithospheric extension: Journal of Petrology, v. 44, no. 9, p. 1657–1679, https://doi.org/10.1093/petrology/egg052.

Simão, N.M., Nalbant, S.S., Sunbul, F., and Mutlu, A.K., 2016, Central and eastern Anatolian crustal deformation rate and velocity fields derived from GPS and earthquake data: Earth and Planetary Science Letters, v. 433, p. 89–98, https://doi.org/10.1016/j.epsl.2015.10.041.

Stern, R.J., and Johnson, P., 2010, Continental lithosphere of the Arabian plate: A geologic, petrologic, and geophysical synthesis: Earth-Science Reviews, v. 101, no. 1–2, p. 29–67, https://doi.org/10.1016/j.earscirev.2010.01.002.

Stern, R.J., and Johnson, P., 2019, Constraining the opening of the Red Sea: Evidence from the Neoproterozoic margins and Cenozoic magmatism for a volcanic rifted margin, *in* Rasul, N.M.A., and Stewart, I.C.F., eds., Geological Setting, Palaeoenvironment and Archaeology of the Red Sea: Cham, Switzerland, Springer, p. 53–79, https://doi.org/10.1007/978-3-319-99408-6_4.

Tanaka, T., Togashi, S., Kamioka, H., et al., 2000, JNdi-1: A neodymium isotopic reference in consistency with LaJolla neodymium: Chemical Geology, v. 168, p. 279–281, https://doi.org/10.1016/S0009-2541(00)00198-4.

Tarı, U., Tüysüz, O., Can Genç, Ş., İmren, C., Blackwell, B., Lom, N., Tekeşin, Ö., Sibel Üsküplü, S., Erel, L., Altıok, S., and Beyhan, M., 2014, The geology and morphology of the Antakya graben between the Amik triple junction and the Cyprus arc: Geodinamica Acta, v. 26, p. 27–55, https://doi.org/10.1080/09853111.2013.858962.

Tatar, O., Piper, J.D.A., Gürsoy, H., Heimann, A., and Koçbulut, F., 2004, Neotectonic deformation in the transition zone between the Dead Sea Transform and the East Anatolian fault zone, southern Turkey: A paleomagnetic study of the Karsu rift volcanism: Tectonophysics, v. 385, p. 17–43, https://doi.org/10.1016/j.tecto.2004.04.005.

Tatsumoto, M., and Unruh, D.M., 1976, KREEP basalt age: Grain by grain U-Th-Pb systematics study of the quartz monzodiorite clast 15405,88, *in* Proceedings of the 7th Lunar and Planetary Science Conference: Houston, Texas, Lunar and Planetary Science Institute, p. 2107–2129.

Uslular, G., and Gençalioğlu-Kuşcu, G., 2019a, Geochemical characteristics of Anatolian basalts: Comment on "Neogene uplift and magmatism of Anatolia: Insights from drainage analysis and basaltic geochemistry" by McNab et al.: Geochemistry Geophysics Geosystems, v. 20, no. 1, p. 530–541, https://doi.org/10.1029/2018GC007533.

Uslular, G., and Gençalioğlu-Kuşcu, G., 2019b, Mantle source heterogeneity in monogenetic basaltic systems: A case study of Eğrikuyu monogenetic field (central Anatolia, Turkey): Geosphere, v. 15, no. 2, p. 295–323, https://doi.org/10.1130/GES01682.1.

Vervoort, J.D., Patchett, P.J., Blichert-Toft, J., and Albarède, F., 1999, Relationships between Lu-Hf and Sm-Nd isotopic systems in the global sedimentary system: Earth and Planetary Science Letters, v. 168, p. 79–99, https://doi.org/10.1016/S0012-821X(99)00047-3.

Westaway, R., 2003, Kinematics of the Middle East and Eastern Mediterranean updated: Turkish Journal of Earth Sciences, v. 12, p. 5–46.

Westaway, R., 2004, Kinematic consistency between the Dead Sea fault zone and the Neogene and Quaternary left-lateral faulting in SE Turkey: Tectonophysics, v. 391, p. 203–237, https://doi.org/10.1016/j.tecto.2004.07.014.

White, W.M., Albarède, F., and Télouk, P., 2000, High-precision analysis of Pb isotope ratios by multi-collector ICP-MS: Chemical Geology, v. 167, no. 3–4, p. 257–270, https://doi.org/10.1016/S0009-2541(99)00182-5.

Yılmaz, H., Over, S., and Ozden, S., 2006, Kinematics of the East Anatolian fault zone between Turkoglu (Kahramanmaraş) and Çelikhan (Adiyaman), eastern Turkey: Earth, Planets, and Space, v. 58, p. 1463–1473, https://doi.org/10.1186/BF03352645.

Yuce, G., Italiano, F., D'Alessandro, W., Yalcin, T.H., Yasin, D.U., Gulbay, A.H., Ozyurt, N.N., Rojay, B., Karabacak, V., Bellomo, S., Brusca, L., Yang, T., Fu, C.C., Lai, C.W., Ozacar, A., and Walia, V., 2014, Origin and interactions of fluids circulating over the Amik Basin (Hatay, Turkey) and relationships with the hydrologic, geologic, and tectonic settings: Chemical Geology, v. 388, p. 23–39, https://doi.org/10.1016/j.chemgeo.2014.09.006.

Yurtmen, S., Rowbotham, G., Isler, F., and Floyd, P.A., 2000, Petrogenesis of basalts from southern Turkey: The Plio-Quaternary volcanism to the north of İskenderun Gulf, *in* Bozkurt, E., Winchester, J.A., and Piper, J.D.A., eds., Tectonics and Magmatism in Turkey and the Surrounding Area: Geological Society [London] Special Publication 173, p. 489–512, https://doi.org/10.1144/GSL.SP.2000.173.01.23.

Yurtmen, S., Guillou, H., Westaway, R., Rowbotham, G., and Tatar, O., 2002, Rate of strike-slip motion on the Amanos fault (Karasu valley, southern Turkey) constrained by K-Ar dating and geochemical analysis of Quaternary basalts: Tectonophysics, v. 344, p. 207–246, https://doi.org/10.1016/S0040-1951(01)00265-7.